Premerger Phenomena in Neutron Star Binary Coalescences

Arthur G. Suvorov [1,2,*] [ID], **Hao-Jui Kuan** [3] [ID] **and Kostas D. Kokkotas** [2] [ID]

1   Departament de Física Aplicada, Universitat d'Alacant, Ap. Correus 99, E-03080 Alacant, Spain
2   Theoretical Astrophysics (IAAT), University of Tübingen, D-72076 Tübingen, Germany
3   Max Planck Institute for Gravitational Physics (Albert Einstein Institute), 14476 Potsdam, Germany
*   Correspondence: arthur.suvorov@ua.es

Abstract: A variety of high-energy events can take place in the seconds leading up to a binary neutron star merger. Mechanisms involving tidal resonances, electrodynamic interactions, or shocks in mass-loaded wakes have been proposed as instigators of these *precursors*. With a view of gravitational-wave and multimessenger astrophysics, more broadly, premerger observations and theory are reviewed, emphasising how gamma-ray precursors and dynamical tides can constrain the neutron-star equation of state, thermodynamic microphysics, and evolutionary pathways. Connections to post-merger phenomena, notably gamma-ray bursts, are discussed together with how magnetic fields, spin and misalignment, crustal elasticity, and stratification gradients impact observables.

Keywords: neutron stars; binary mergers; multimessenger astrophysics; gravitational waves; high-energy astrophysics

1. Introduction

Massive stars that have exhausted their fuel reservoir eventually collapse, as the outward pressures no longer resist the inward gravitational pull. The brilliant supernovae that accompany these collapses rip away most of the outer layers of material, though the inner layers become more and more compressed. Subatomic fermions, both individually through their Pauli degeneracy pressures and collectively through many-body interactions, provide a last bastion of resistance against this compression. The strongest such pressure is from neutrons, and thus *neutron stars* represent some of the most compact objects in the universe, behind only black holes and the hypothetical quark stars. Neutron star core densities likely reach supranuclear levels ($\sim 10^{15}$ g/cm^3; [1–3]) because their stellar radii are of the order of $\sim$12 km. Studying their properties thus enables, for instance, tests of the "low-energy" limit of quantum chromodynamics with baryonic degrees of freedom and general relativity (GR). The exact chemical makeup of a star defines its equation of state (EOS), determining the particulars of which constitutes one of the open problems in high-energy astrophysics.

Neutron-star mergers are some of the brightest events in the universe. A crescendo of gravitational waves (GWs) is released during the final moments of the inspiral, culminating in a "chirp" and the subsequent ringdown of the hyperactive remnant left behind at the crash site, being either a black hole or another, heavier neutron star (e.g., [4,5]). In the latter case, the object will likely be short-lived: it may maintain a state of metastability despite having a mass larger than the maximum (i.e., Tolman–Oppenheimer–Volkoff limit) applying to an "ordinary" neutron star if supported by centrifugal [6], thermal [7], or magnetic [8] pressures.

Much of the fireworks come shortly after the actual coalescence in the form of gamma-ray bursts (GRBs), primarily of the short variety with prompt durations of less than two seconds, though there is evidence that some mergers can also fuel long bursts (e.g., [9,10]). Through either a fireball-like (neutrino–anti-neutrino) or Poynting-like process, a relativistic jet is collimated by the remnant, providing the impetus for a wealth of emissions

that are both luminous (isotropic energies often reach $\sim 10^{53}$ erg) and broadband (spanning $\sim$20 magnitudes in frequency space via long-lived afterglows). The multimessenger event GW170817/GRB170817A [11,12] has not only firmly established the merger–GRB connection but has been used to place strong constraints on the nature of matter in extreme environments and hypothetical departures from GR in the ultraviolet (e.g., [13–15]).

A range of luminous and sometimes multiband events can also take place in the moments *leading up to* a binary coalescence. One of the main subjects of this review pertains to such *precursors*: a fraction ($\lesssim$5%; [16]) of merger-driven GRBs show statistically significant gamma-ray flashes before the main GRB. While other types of precursors may be released premerger (covered in Section 7), we typically write *precursor* to specifically refer to these first-round gamma flares. Indeed, many reviews are devoted to the topic of merger phenomena, involving numerical simulations and observations of inspirals, remnant dynamics, and the subsequent forming of relativistic jets (see [17–24] for instance). Comparatively little attention has been given towards a complete description of what can be (and has been!) learned *just prior to merger*, where such precursors may be expected. Our goal is to fill this gap, motivated in part by recent observational campaigns devoted to searching for precursor flares (e.g., [25–27]) and the ushering in of the LIGO–Virgo–KAGRA (LVK) collaboration's O4 science run. In the spirit of the burgeoning field of multimessenger astrophysics, we also cover the theory of tides and premerger GWs in detail in the hope that a reader not interested in gamma-ray precursors may still find value.

Precursor flashes give promise for a plethora of information about fundamental physics, naturally complementing that associated with merger and post-merger phenomena. A premerger precursor could be used, for instance, to improve sky localisation for an impending collision if nothing else (see [28]). One key difference though is that premerger objects are likely *cold*, and thus arguably give a better handle on the EOS, as the impacts of $\gg$ MeV temperatures and a littered environment (e.g., from dynamical ejecta) do not require disentangling. Precursors are observationally diverse. They have waiting times—relative to the main GRB (not merger!)—spanning $\sim$30 ms to $\sim$20 s. Their durations and luminosities span a commensurate number of magnitudes, with spectra varying from being almost a perfect blackbody to being highly non-thermal. Such an assortment of characteristics makes a strong case that there may be subpopulations of such precursors fuelled by different means (e.g., [16]). By dividing our discussion on precursors into observational (Section 5) and theoretical (Section 6) elements, we hope to build a full picture of these rich systems.

Premerger precursors are primarily thought to be caused by one of two means. The first involves direct, electromagnetic interactions between the two stars (e.g., [29–32]). For instance, if the inspiralling constituents have dipole moments which are anti-aligned with respect to each other, ample reconnection can take place as the field lines get more and more entwined as the orbit decays. To achieve large luminosities, one would expect the flares to be emitted very close to the merger as the dipole fields die off like the cube of the distance. Therefore, one may anticipate relatively short *waiting times* (see Section 5) in this case, unless magnetars are involved in the merger. Spectral and other considerations of certain precursors, however, give reason to suspect that some mergers do indeed contain a magnetar (e.g., [33–35]), despite the fact that the GW inspiral time exceeds the characteristic Ohmic decay timescale by orders of magnitude (see Section 2.3).

The second ignition mechanism involves tidal fields. Tides can not only deform the star geometrically ("equilibrium tide") but also excite internal fluid motions ("dynamical tides"). These internal motions are characterised through a set of *quasi-normal modes* (QNMs). These QNMs, which come in a few families (e.g., *g*-modes) that we properly introduce in Sections 4.1.3 and 6.4, though we also sprinkle information about them throughout the paper, can be driven to large amplitudes when coming into resonance with the dynamical tidal field. This tidal driving can manifest gravitationally, through a dephasing of the gravitational waveform, and electromagnetically, by liberating the potential energy of a star whose crustal layers succumb to the high-amplitude pulsations. Ruptures and subsequent

energy release models are akin to some of those considered for magnetar flares (see [36,37]), though in the premerger context, the cause of *crustal failure* is QNM resonances rather than the gradual build-up of mechanical stress from the secular evolution of a superstrong field.

Galactic neutron stars exhibit a variety of multiwavelength phenomena, the varying characteristics of which have invited rather detailed classification schemes over the years, with stars being grouped into categories such as recycled, radio, or X-ray pulsars (e.g., [38]). We describe how precursors, and inspiral lead-up, more generally, can inform us about each of these pathways. This review is thus roughly divided into two halves, that devoted to GWs and that to electromagnetic precursors, described in more detail below.

1.1. Structure and Purpose of This Review

Premerger phenomena can be either gravitational or electromagnetic, both of which we cover in later sections. Before doing so, however, it is important to give a sense of background regarding both the neutron star macro- (Section 2) and microstructures (Section 3), as these aspects are those which we hope to learn about from multimessenger channels. We therefore aim to make this review self-contained by exploring the theoretical and observational elements of neutron-star properties.
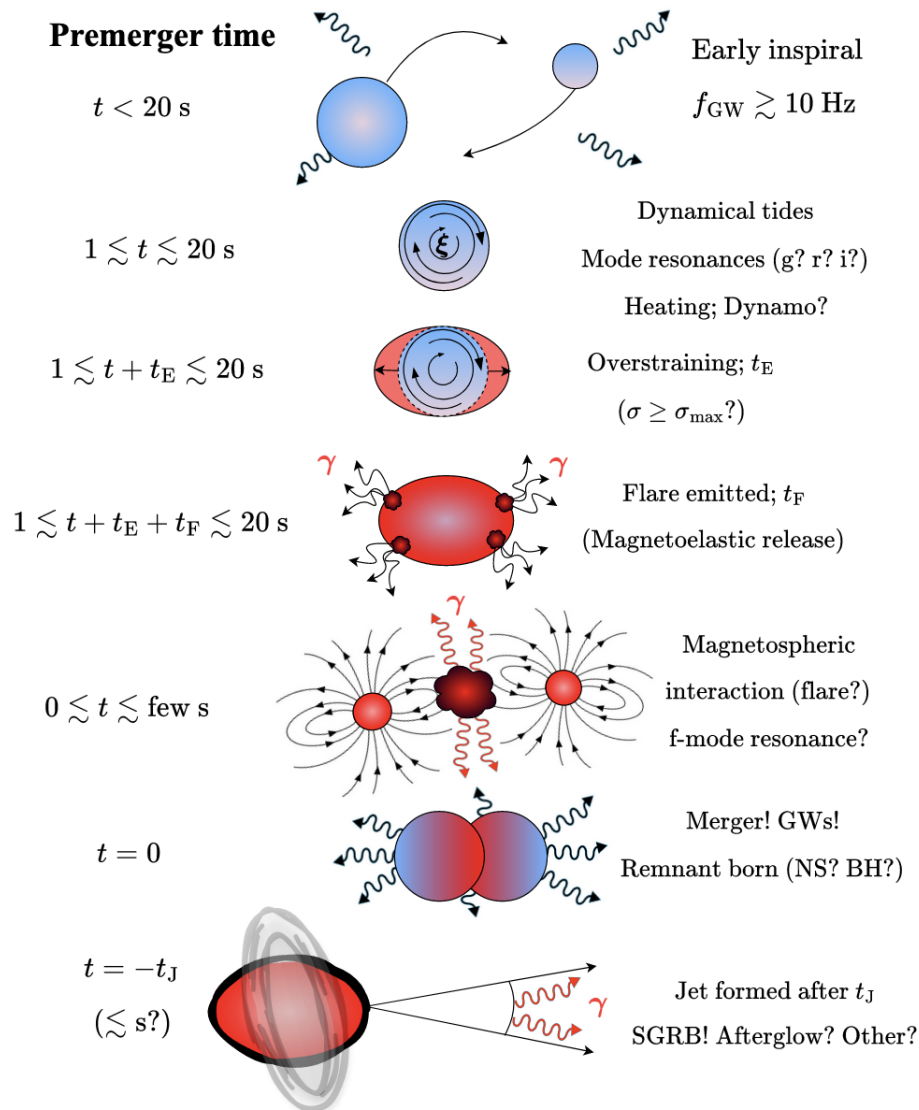
The main purpose of this work is to detail some aspects that we feel have received little attention. For example, the theory of dynamical tides is rich and varied in the literature, with several different notations being used and so on. Similarly, precursors seem to have escaped attention despite their, as we argue, at least, propensity for educating us about neutron star physics. Figure 1 depicts the various elements we describe throughout, together with a rough timeline of the anticipated events.

We begin by introducing details about the neutron star structure generally (macrophysics in Section 2 and microphysics in Section 3) to pave the way in describing how the final $\sim$20 s of an inspiral may appear. Section 4 covers the gravitational aspects of this: how an inspiral occurs, the order at which post-Newtonian (PN) effects come into play, and most importantly, how tides influence the dynamics. The resonant QNMs that are excited lead to a gravitational dephasing of the waveform that can be studied and used to infer properties about the inspiralling constituents. These tides, however, may also be important for (at least modulating) precursor emissions. The observational elements of these precursors are described and collated in Section 5 with theoretical explanation(s) and modelling in Section 6. These ideas in the context of multimessenger astrophysics more generally are reviewed in Section 7 with a summary given in Section 8.

The hasty reader who is familiar with neutron stars but cares about tidal-interaction theory and/or GWs can skip to Section 4, while a reader most interested in precursors observations or theory can head to Section 5 or Section 6, respectively.

1.2. Remarks on Notation

We use subscripts A, B to denote the primary and companion elements of a binary. Here "primary" will usually mean the heavier object, though for some theoretical discussions, it may simply refer to the object for which finite size effects are resolved when ignoring (as is typical) the multipolar structure of the companion. In cases where no ambiguity can arise, the subscripts are dropped for presentation purposes. We adopt the indicator α for arbitrary mode quantum numbers in reference to a radial and angular decomposition; see Section 4.1. If only a right-hand subscript is written (e.g., g_i), this refers to the radial node number n with $\ell = m = 2$. Most of this review is carried out in a Newtonian language, where Latin indices (aside from n, m, or ℓ) refer to spatial components of a tensorial object (typically with respect to a spherical basis). Linear frequencies are written with $f_\alpha = \omega_\alpha/(2\pi)$ for angular frequencies ω. When discussing object spin and the orbit, the symbol ν is used instead for the linear frequency (e.g., $\Omega_{\text{orb}} = 2\pi\nu_{\text{orb}}$). A superscript asterisk indicates complex conjugation. An overhead dot denotes a time derivative.

Figure 1. Cartoon depiction of premerger events culminating in a GRB with at least one precursor flare. A binary of a cold neutron star inspiral and the equilibrium tidal imprint on the gravitational waveform can be used to deduce something about the stellar structure. Once the orbital frequency matches that of some mode, dynamical tides start to induce a dephasing in the waveform through resonances; meanwhile, heating occurs. Modes exert stress on the crust such that it may overstrain after time t_E for favourable eigenfunctions. Magnetoelastic and/or thermal energy is released following a flare development timescale t_F, possibly modulated by quasi-periodic oscillations (QPOs; as in GRB 211211A). Once the separation is sufficiently small, magnetospheric interactions may also be powerful enough to produce bright gamma-ray or broadband emissions. In the final stages, the fundamental mode may also become resonant. The stars then coalesce, at the peak of the GW signal, the information of which can be further used to decipher the nature of the inspiralling stars and the remnant (as for GW 170817). The remnant, whether a neutron star of some meta-stable variety or a black hole, likely surrounded by a temporary accretion disk in any case, can then launch a GRB jet that successfully drills out after some delay timescale, t_J.
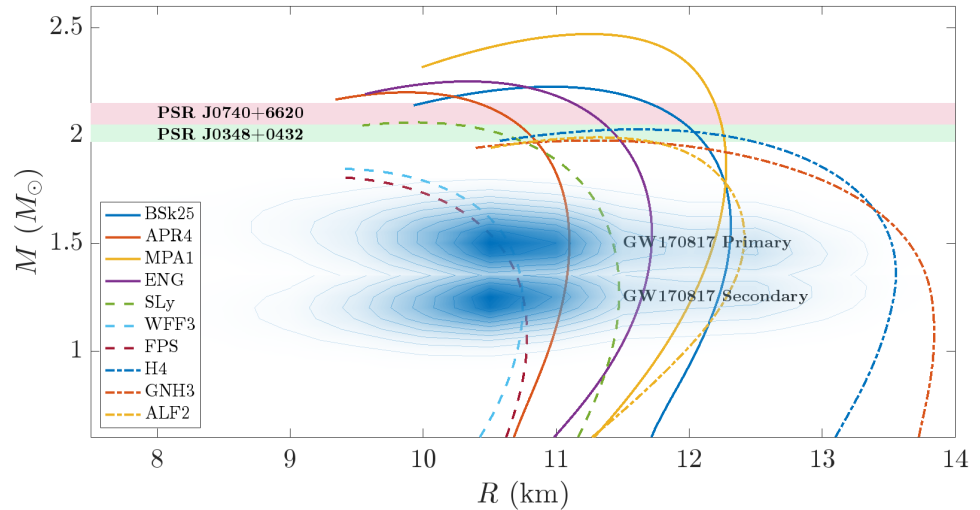
2. Neutron Star Macrostructure

The macrostructure of a neutron star, such as its mass and radius (via the EOS), greatly impacts premerger phenomena. In order to be self-contained, this section provides a brief review of that macrostructure with a view of the key aspects that will be relevant for us later in describing GWs and precursors.

2.1. Equations of State

Neutron stars exhibit an astonishing range of multiwavelength phenomena, from steady radio pulsing to rare storms of powerful soft-gamma flares (e.g., [39]). From a nuclear physics perspective, however, it is thought that neutron star matter comes into beta equilibrium shortly after birth [40]. This implies that their cores are described by a unique EOS moderated by small, thermodynamic perturbations. Proto-stars, especially those born in merger events [41], may be exempt, however, as new particle production pathways can be opened at super-MeV temperatures. For mature stars, a barotropic EOS is typically used though, where the hydrostatic pressure p is just a function of the rest-mass density ρ. This latter quantity is distinct from the *energy density* ϵ, though sometimes in the literature one can find "EOS" of the form $p = p(\epsilon)$; see Section 2 of [42] for a discussion.

Many EOS families have been considered in the literature [1,3], primarily owing to our collective ignorance regarding the behaviour of matter at supra- and hypernuclear densities at low temperatures. The EOS families we consider in an effort to make this review self-contained—mass–radius curves, which are displayed in Figure 2—cover stars with purely *nepμ* compositions to those exhibiting phase transitions to free-quark regimes (i.e., the hybrid stars, like ALF2; [43]). Although some of the considered EOS cannot support the heaviest (confirmed[1]) neutron star observed to date, namely, PSR J0740+6620 with a mass of $\sim 2.08^{+0.07}_{-0.07} M_\odot$, we consider them for completeness (especially those that pass right through the heart of GW 170817 contours). Another object worth mentioning in this landscape is HESS J1731-347, with a mass of $\gtrsim 0.8 M_\odot$ and $R \approx 10.4$ km [44]; if indeed this were representative of the lower limit to the possible neutron star mass, it would impose serious restrictions to the EOS and formation mechanisms. J1731 measurements would, funnily enough, be fully consistent with the dashed-curve EOSs in Figure 2 that do not reach $M \gtrsim 2 M_\odot$; see Figure 5 in [45].


Figure 2. Mass–radius diagram for select EOSs (see plot legends). These EOSs belong to three different groups, distinguished by curve style (solid, dashed, and dot-dashed; see main text). Inferences on the mass and radius of pulsars involved in binaries (PSR J0740+6620 and PSR J0348+0432) and in the binary merger event GW170817 are overplotted in the shaded regions.

Thermal and inviscid effects in a mature neutron star, though crucial for modelling buoyancy-restored oscillations (i.e., *g*-modes; see Section 4.1.3) especially in the crust (see Section 3.1), are often not present in many of the "standard" EOS tables because the effects are thought to be safely negligible below $\sim$0.1 MeV, where the chemical potential is tiny. Such corrections can be handled with a $\propto T^2$ thermal pressure contribution. The "general purpose EOS" (following the naming of the catalogue) available on the CompOSE catalogue[2] provide such information. Although a few general purpose EOSs do extend to a lower cutoff at 10^7 K (e.g., SLy4 and APR), many of them have their tables truncated at

minima of 10^9 K (still much higher than expected of a mature star seconds before merger; cf. Section 4.5) since lower temperatures are well modelled by cold EOSs with some perturbative corrections as described above.

The impact of realistic thermal profiles on the g-spectra in this perturbative sense has been detailed by [47] and by [48] with an independent code, finding consistent results. As found by [49], the g-spectra are linked to the "slope" of the EOS M vs. R curve, and are especially sensitive to central densities in the range of 1–3 ρ_0 for nuclear saturation value $\rho_0 \approx 2 \times 10^{14}$ g cm^{-3} [50]. The same slope impacts on the universality of some relations between the bulk properties and dominant peaks in post-merger waveforms [51]. Ref. [49] also found that g-mode scaling relations can be grouped according to EOS, with hadronic ones that can support heavy stars (solid lines in Figure 2), those that cannot (dashed), and EOSs involving phase transitions leading to either hyperon nucleation or quark deconfinement (dash-dotted); we refer the reader to [52] for a review on hyperonisation. These three families each abide by a different set of "asteroseismological relations" that can, in principle, be distinguished by observations.

Detailed analyses of the EOS population, their historical development, together with astrophysical applications and constraints, are found in [1–3,50]. Observationally, masses can be constrained from a variety of methods, ranging from the orbital timing of binaries to the phased-resolved tracking of thermal hotspots atop an isolated star to GWs. Observations of the moments of inertia can also be made from periastron advance in binaries [53]. We now turn to describing a few EOS families. Note that some of the EOSs appearing in Figure 2 are not covered below despite their consistency with data, though they could adequately be described as "relativistic models". For example, MPA and ENG are based on Dirac–Brueckner–Hartree–Fock models for purely nucleonic matter, while GNH(3) is a relativistic mean-field EOS that also contains hyperonic matter. In one of the considered EOS (ALF2) a hadron–quark hybrid core is present, described through the MIT bag model.

2.1.1. WFF Family

The WFF family (WFF1-3) was developed in the late 1980s [54] based on realistic nucleon–nucleon interactions calculated using many-body methods. This family treats nucleons as non-relativistic particles, utilising the Argonne v14 (so-named because it uses 14 operator components to model nucleon–nucleon interactions) and Urbana vII potentials which account for three-nucleon forces. The family is generally considered to be a softer EOS, especially WFF1. According to the WFF family of EOSs, the maximum mass of a neutron star typically ranges up to 2.2 $M_\odot$ (WFF1-2) in agreement with the aforementioned observations. Still, recent results from GW170817 and the Neutron Star Interior Composition Explorer (NICER) suggest a stiffer EOS; thus, WFF1 is excluded as being too soft. It is for this reason that we exclude it from Figure 2. Despite these limitations, many works still use the WFF family of EOSs as representatives of softer EOSs. The WFF family has improved over time by including additional interactions and so on, with many modern EOSs stemming from it (see [55]).

2.1.2. APR Family

The APR EOS is named for the authors Akmal, Pandharipande, and Ravenhall, who developed it in the late 1990s [56]. It is widely adopted, despite the fact that at high densities, relativistic corrections are large and using the non-relativistic Schrödinger equation at $\rho \sim$ several $\times \rho_0$ is questionable, as it meets the maximum mass observational limit in the static limit (and beyond to $\sim 2.3 M_\odot$); models the cooling evolution (implicitly via proton fraction predictions and beta-decay rates in superfluids) as observed in young and old neutron stars (see [57]); and can meet the constraints set by GW observations of neutron-star mergers. It is not necessarily unique in these respects though. The APR EOS is derived from a microscopic nuclear many-body theory using the variational chain summation method. It predicts a phase transition from pure nucleonic matter to a state including nucleons and neutral pion condensation at high densities [58] and incorporates

realistic nucleon–nucleon interactions based on the Argonne v18 potential (which, as per the discussion above, includes 18 interaction operators). In addition to two-body interactions, it includes three-body forces using the Urbana IX potential: these are essential for providing *repulsive* interactions at high densities. It is through these repulsive interactions that one may construct heavier neutron stars. For up-to-date discussions, see [58,59].

2.1.3. SLy Family

The SLy EOS is based on a semi-empirical approach that parametrises the interactions between nucleons (protons and neutrons) in terms of density-dependent coefficients of the nuclear interactions [60–63]. It is derived from the Lyon–Skyrme energy density functional (SLy) and uses a parameter set of coefficients (e.g., terms weighting the kinetic energy of nucleons) that are chosen to describe the properties of both symmetric nuclear and neutron-rich matter through fittings to six nuclear masses (spherical nuclei with an even number of neutrons and even number of protons). Neutron star models constructed using the SLy EOS can reach a maximum mass of $\sim 2.1 M_\odot$ and have a radius of $11 \lesssim R \lesssim 13$ km for typical stars with 1.4 solar masses; it is, therefore, a relatively stiff EOS. The SLy EOS is designed to be valid for a wide range of densities, ranging from the crust up to a few times the nuclear saturation density.

Although the SLy EOS can accommodate existing mass and radius constraints and is widely used in simulations of supernovae and neutron star mergers, especially updated versions with finite-temperature corrections [63–65], it does not allow for the direct Urca or other "enhanced cooling" processes to operate. This places it in strong tension with observations of thermal emissions from accreting and isolated neutron stars [66].

2.1.4. BSk Family

The BSk EOS is developed through the use of the Brussels–Skyrme (BSk) energy density functionals[3]. Like SLy, BSk is based on Skyrme-type energy density functionals that use density-dependent coefficients to parametrise nucleon–nucleon interactions. These functionals are fitted to match the experimental data on finite nuclei and nuclear matter, resulting in a sequence of incrementally named models [67–71]. The BSk functionals are, however, fitted to a much larger set of experimental nuclear data relative to that of SLy, namely all nuclear masses with $Z, N \geq 8$ with a model root-mean square deviation of ≈ 0.5 MeV. The deviation from mass data (considering the restricted set of even–even nuclei) for the SLy EOS is an order of magnitude larger (≈ 5.1 MeV [72]). In general, fitting terms using the largest available sets of nuclei—even and odd, spherical and deformed—is crucial to properly calibrate the functional(s).

In contrast to some other EOSs, members of the family need not assume strict beta equilibrium; see Fantina et al. [73] for a description of accreted crusts with X-ray burst ashes made of iron for BSk19–21. Finite-temperature corrections are included but only for the surface layers at densities below 10^6 g cm^{-3}. The predicted relationship varies depending on the model number, but typically one has a radius of 11–13 km for 1.4 $M_\odot$ neutron stars as for SLy. The BSk models also predict a relatively high maximum mass of between 2 and 2.4 $M_\odot$. In Figure 2, we show the *M-R* relation for one member of this family, BSk25, for which the maximum mass is 2.23 $M_\odot$ and the radius of the model with 1.4 $M_\odot$ is $\approx$12.3 km. BSk21-25—unlike SLy4 as well as BSk19,20,26—*do* allow for the direct Urca process in dense matter and conform better to cooling observations [66].

2.2. Rotation and Binary Alignment

Angular momentum is ubiquitous in nature. In the case of neutron stars, approximate angular momentum conservation during the supernova process implies that proto-stars can be born spinning fairly quickly, even for relatively slow progenitors. Depending on the progenitor and the impact of fallback accretion [74], some neutron stars may be born with millisecond spin periods [75]; however, see also [76,77].

Even for "slow" objects (e.g., magnetars performing a full revolution at rates less than once per few seconds), it is essential to account for rotation when considering electromagnetic observables. Depending on the rotational phase, the signal can be broadened or lost due to beaming effects, which impacts interpretation. Observationally, neutron stars seem to be anything between practically static up to spins of ~800 Hz. Why there is such an observational upper limit is a topic of active research, invoking various explanations from GW-enhanced spin-down to centrifugal propellering either from a companion or fallback (see [78] for a discussion).

One would like to know what the likelihood of having a "rapidly" rotating star taking part in a merger is. A review of spin properties in binaries, and the formation of double neutron-star systems in general, can be found in [79]. The situation is somewhat complicated, however, and it has been argued that there may be three subpopulations of double neutron-star systems with distinct spin distributions, pertaining to (i) short-period and low-eccentricity binaries, (ii) wide binaries, and lastly (iii) short-period, high-eccentricity binaries [80]. The canonical formation channel involves a symbiotic binary (i.e., without dynamical captures) where there are two supernovae. These supernovae are separated by a timescale that is sensitive to a number of evolutionary specifics related to common-envelope evolution and how susceptible the companion is to Roche lobe overflow, which in turn depends primarily on the mass ratio (e.g., [81]).

Prior to double neutron-star formation, accretion by the first born from the non-degenerate star can be either of a disk or wind-fed nature, and will tend to spin-up the neutron star, thereby leading to a "recycled" object with a spin that is (close to) aligned with the orbital angular momentum. A discussion on predictions for alignment angles can be found in Section 2.3 of [48] and the references therein: several binaries have non-negligible misalignment angles as measured through geodetic precession and optical polarimetric measurements (e.g., PSR B1534+12 in a double neutron-star system with a misalignment of ~27°; [82]). Such misalignment is relevant for the excitation of non-axisymmetric modes during inspirals (see Section 4.3). Either way, for a spin-up rate of $\dot{\nu} \gtrsim 10^{-14}$ Hz s^{-1}, not unusual from observations or torque theory [83], the first-born neutron star could attain spins of $\gtrsim 100$ Hz within significantly sub-Hubble times $\lesssim 10^2$ Myr (see Table 1 in [79]). Given that the dipolar magnetic field may be buried by large factors via epochs of mass infall [84–87] (see also Section 2.3), the spin-down that sets in, once the secondary collapses and stops gifting material, may not be sufficient to erase spin-up before merger.

It was estimated that between 15 and 30% binary neutron stars will have spins measurable via GWs at $\gtrsim$90% confidence [88]. This implies the importance of accounting for spin in tidal modelling, as all mode eigenfrequencies are skewed by even a modest degree of rotation; see Equation (24) and also Appendix A of [34].

2.3. Magnetic Fields

It has been recognised since the dawn of pulsar astronomy that rotating magnetic fields, as an induction conduit for electric fields, are not only responsible for radio activity but also instigate the star's gradual slowdown and moderate crustal activity. In order to accurately interpret neutron star activity to unveil the stellar EOS and other aspects, models of their magnetic fields, together with their evolution and dynamics, have been constructed in the literature from a variety of techniques. Magnetic fields are crucial for all of the electromagnetic, premerger phenomena considered here; we therefore feel it is appropriate to provide a brief discourse on the current understanding of magnetic structure. If strong enough, magnetic fields may even alter the GW signals associated with inspirals or EOSs (e.g., [89]) in a variety of ways; see Section 4.4.

Although a complete survey of how the magnetic field impresses on observables associated with the neutron star population at large lies well beyond the scope of this review (see Enoto et al. [38] for a thorough exposition), many observations have proven that magnetic multipoles and topologically complicated structures are a reality:
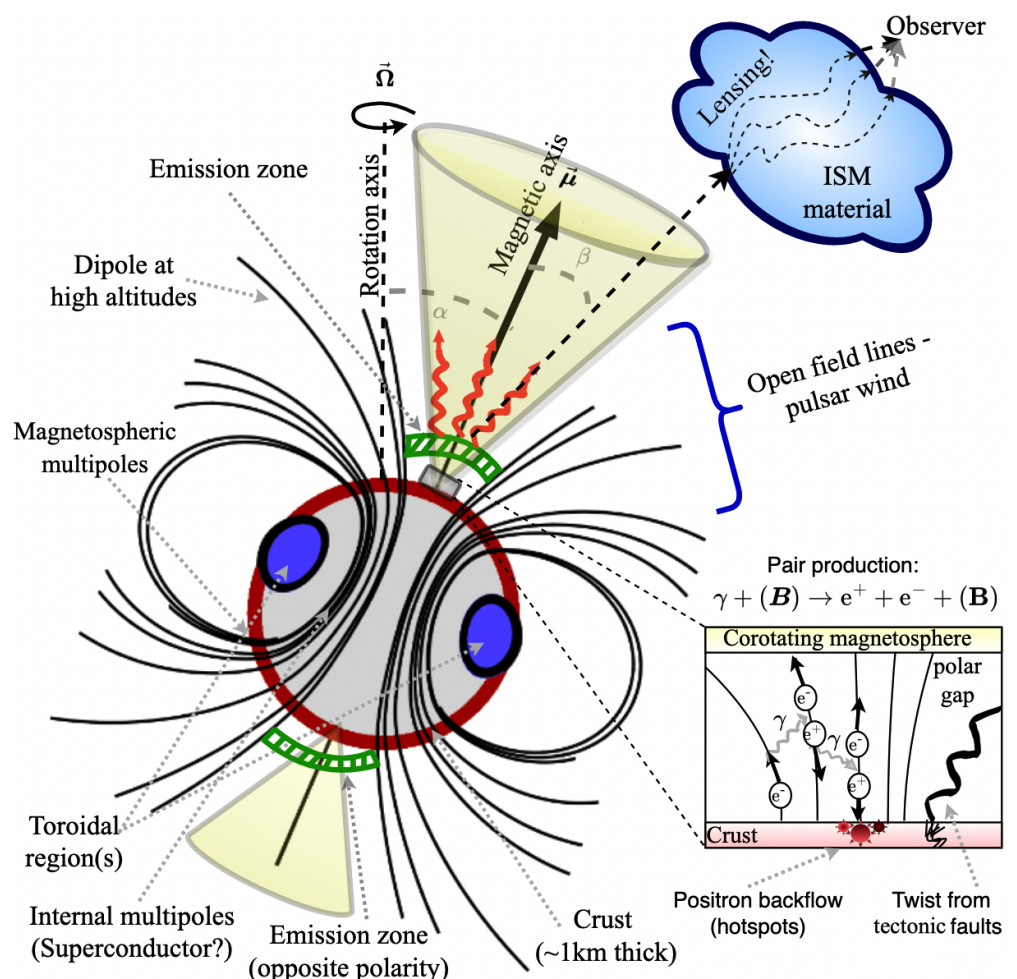
★ Data from NICER and other experiments indicate that 'hotspots' atop millisecond pulsars (e.g., PSR J0030+0451) are not antipodal [90,91]. This implies equatorially asymmetric heating, and therefore a magnetic field composed of a mix of odd- and even-order multipoles [92,93].

★ Models of pulsar radio-activation cannot explain the bulk of the population if the surface and magnetospheric field geometries are dipolar, i.e., dipole "death lines" cut right through the middle of the population on the *B-P* diagram [94,95].

★ The morphology of pulsed emissions are highly varied, with some systems displaying long-term epochs of nulling or interpulses. Interpulse phenomenology in radio pulsars can be qualitatively explained by an oblique rotator with a multipolar magnetic field, as the emissions are then composed of multiple components [96]. The X-ray light curve from the magnetar SGR1900+14 also displays interpulse-like phenomena, which may be contributed by multiple hotspots on the surface [97]. Zhang et al. [98] suggest that starspots (i.e., localised and multipolar fields) may emerge through Hall evolution near the poles of neutron stars that are hovering around the death line, sporadically allowing the hosts to pulse and possibly explaining nulling (see also [99]).

★ Multipoles are typically generated via cascade phenomena through Hall drift [99] or plastic flows [100] in neutron star crusts if the "magnetic Reynolds number" is sufficiently large ($B \gtrsim$ few $\times 10^{12}$ G [83]), and likely also through ambipolar diffusion in the core [101]. For crustal fields with a high-degree of relative helicity, *inverse cascades* can instead operate [102], where energy is transferred from small to large scales, though this presupposes an initially multipolar field. Either way, Hall–Ohm simulation outputs are supported by observations of neutron-star cooling and (more speculatively) field decay.

★ Many pulsar *braking indices* differ from the canonical dipole value of three, which points towards a complicated field geometry, anomalous braking torques, and/or mass-loaded winds initiating a different spin-down behaviour [103,104]. Glitch activity [105], Hall waves launched from superconducting phase transitions [106], or inclination angle evolution [107] may also notably affect this index, $n = \nu\ddot{\nu}/\dot{\nu}^2$.

★ Simulations of accretion show that even small accretion columns (or 'magnetic mountains') warp field lines far from the column itself [84,86,93], with field line compression within the equatorial belt persisting over long, Ohmic timescales [87]. Given that all neutron stars born from core collapse exhibit some degree of fallback accretion at birth from a temporary disc of bound material, one might expect all stars to have 'buried' and multipolar components [108]. Even ignoring this possibility, particle production and backflow in the magnetosphere will gradually advect field lines, instigating some (small) degree of multipolarity surviving over diffusion timescales. Such considerations were initially motivated by the observation that neutron stars in low-mass X-ray binaries (LMXBs; undergoing Roche lobe overflow) tend to possess unusually low magnetic field strengths [109].

★ Cyclotron resonant scattering line energies demand that a number of accreting and isolated neutron stars possess local fields (much) stronger than those implied by global, dipole-field observations [110].

★ Current bundles injected into the magnetosphere by crustal motions twist the fields there, inducing multipolarity [111]. Models of neutron star activity often invoke crustal failures as seeding events for outbursts (such as glitches or flares, e.g., [112–114]), and therefore, such injections may be common. In fact, crust failures are one of the mechanisms proposed for premerger precursors; see Section 6.

Aside from *poloidal* multipoles, the neutron star magnetic field also likely contains a multipolar and geometrically complicated *toroidal* component:

★ Precession in magnetars, such as 4U 0142+61 [115] and SGR 1900+14 [116], are most straightforwardly explained through a (sub)crustal toroidal field of strength $\gtrsim 10^{16}$ G: such a field introduces a prolate distortion along the magnetic axis, which then becomes misaligned with the rotation axis, causing free precession (see also [117,118]).

- ★ Mixed fields are necessary for the stability of the star. Magnetohydrodynamic (MHD) models and stability analyses demonstrate that purely poloidal/toroidal fields are unstable over dynamical timescales [119–121].
- ★ Dynamo models aiming to explain the intense fields of magnetars rely on poloidal–toroidal amplification cycles. More generally, differential rotation will wind up poloidal lines. Given that some differential rotation is inescapable, as the spin-down torque applied to the surface cannot instantaneously influence the core (i.e., there is a crust–core lag; [122]), toroidal components should be generated.
- ★ A universal feature of magnetothermal evolutions is that energy swaps between the toroidal and poloidal sectors, at least for sufficiently strong fields (e.g., [123,124]). Multipolarity is thus inevitably generated in the toroidal sector from each of the considerations listed above.

Figure 3 illustrates the conventional picture of pulsar operation and the presence of the magnetic substructure, generally (including the likelihood of internal multipoles and a superconductor; see Section 3.4). The interpretation of neutron-star phenomena is complicated by the fact that emissions must traverse the interstellar (or intergalactic) medium, which can lens photons or GWs (see [125]).


Figure 3. Conventional view of pulsar operation with a "twisted torus" magnetic field [126] and polar gap(s) [127]. The presence of a complicated magnetic substructure is highlighted.

Perhaps more importantly for us here, magnetic fields are subject to decay. The exact way in which this occurs within a neutron star can be subtle. For example, evolution in the crust is thought to be governed by a coupled Hall–Ohm system [128], at least for submagnetar ($\lesssim 10^{15}$ G) fields where plastic flow does not enter the picture [129]. Hall

evolution is strictly conservative though, and so even though the decay is only driven by Ohmic terms, Hall drift tends to accelerate such a decay by cascading: energy is transferred from large to small scales, whereupon it is more susceptible to decay.

If we ignore plastic flows (though see [100,129,130]), the overall crustal field strength evolution may be written, after solving a simplified volume-averaged version of the induction equation following Aguilera et al. [131], as

$$B(t) = B_0 \frac{\tau_{\rm H}}{e^{t/\tau_\Omega}(\tau_{\rm H} + \tau_\Omega) - \tau_\Omega}, \tag{1}$$

with $\tau_{\rm H} = 4\pi e n_e L^2 / c B_0$ and $\tau_\Omega = 4\pi \sigma_e L^2 / c^2$ for length-scale $L \lesssim R$ (smaller for higher-order multipoles), initial field strength $B(0) = B_0$, electron number density n_e, and electrical conductivity parallel to the magnetic field $\sigma_{\rm e}$. For typical parameter choices in the crust, we may have, therefore, that $\tau_H \sim \text{few} \times 10^4 (B_0/10^{14}\,{\rm G})^{-1}$ yr and $\tau_\Omega \sim \text{few} \times$ Myr. Given, however, that the GW inspiral time is orders of magnitude longer than either of these times unless the field strength is $\sim 10^{10}$ G, one anticipates weak fields at the time of merger. This has important implications for the precursor flares we discuss in Section 5.

It is important to note, however, that there are some ways around the decay issue, such as via Hall stalling (i.e., the system reaches a quasi-equilibrium where $\tau_{\rm H}$ tends to some much larger number; [132]), an absence of crustal impurities (which increase the conductivity and hence the Ohmic time; [133]), plastic flows (which can work to halt electron flows and thus suppress cascading and the formation of multipoles; [100,130]), or dynamical capture (thereby avoiding issues related to decay altogether). Another interesting possibility relates to superconductivity (see Section 3.4). A strong core field may be retained if the decay timescale lengthens as the star cools [134], while a strong crustal field could exist if the expulsion time of the core flux into the crust is long. Whether it is at all possible for magnetar-level fields to persist over cosmological timescales remains an active area of research (see [133,135] for discussions).

3. Neutron Star Microstructure

In some cases of relevance, the stellar microstructure can also influence premerger observables. Again in the interests of being self-contained, this section delves into some relevant aspects of microphysics, with an emphasis on the crust.

3.1. Basic Elements of Crustal Physics

Although a neutron star may be born with temperatures in excess of $\gtrsim$ MeV, especially in a merger, the system begins to cool rapidly through a sequence of beta decays (Urca reactions) as neutrinos flood outward from what is currently an envelope (e.g., [136–138]). The details of these very early stages in the star's life are a matter of active research and lie beyond the scope of this review; see, for instance, Sarin and Lasky [23]. Still, this early behaviour *is* important as concerns some early post-merger phenomena within our purview, so some details are touched on in subsequent sections.

Nevertheless, for the mature stars taking place in a merger, it is expected that the outer layers long ago formed an elastic solid that should be distinguished from the liquid core. These low-density regions, with the exception of the very outer layers comprised of a thin ocean and atmosphere, are called the crust because nuclei are cold enough to freeze and form a crystalline solid which can sustain stress. The crust is important for all electromagnetic phenomena from neutron stars, as it is ultimately the region where external field lines are anchored. During late inspiral, a great deal of heat is generated via the tidal field and resonant modes; this heating (see Section 4.5), in addition to the stresses exerted by resonant pulsations (see Section 3.2), and despite the fact that the crust constitutes only ~1% of the total stellar mass, plays a central role in the precursor phenomena covered in later sections.

The nuclear phase of the matter in the envelope can be understood through the Coulomb coupling parameter for ions

$$\Gamma = \frac{Z^2 e^2}{a_i k_B T},$$ (2)

where Z denotes the number of protons in the ion, a_i is the ion sphere radius (i.e., the Wigner–Seitz cell radius) such that $4\pi a_i^3/3$ equals the volume per ion, $1/n_i$, e is the elementary charge, k_B is the Boltzmann constant, and finally T represents the temperature. Aside from fundamental constants, each ingredient defining Γ varies with depth in a complicated way [139]. Once the temperature drops sufficiently ($\sim 10^8$ K) such that $\Gamma \gtrsim 175$ (e.g., [140]), the liquid envelope solidifies via a first-order phase transition into an elastic material—the crust.

In general, because of the density dependence in expression (2), the crust may not entirely encompass the final $\gtrsim 1$ km of the star. It is expected at least that there will be an 'ocean' separating the crust from the magnetosphere (e.g., [141]; see also Section 6.4.3), the physics of which depends strongly on temperature, meaning first of all that a zero-temperature EOS cannot apply [142] but also that no stress can be supported there. The crust–core transition takes place at a (baryon) density n, which depends on the EOS [62,143,144]; for instance, $0.07 \lesssim n \lesssim 0.09$ fm^{-3} for the BSk EOS [69], i.e., $\rho \sim 10^{14}$ g/cm^3 within a factor of a few. Crust–ocean and ocean–atmosphere transitions occur at much lower densities which are highly temperature and composition dependent (see Figure 2 in [145], for instance).

Supporting Stress

In elasticity theory, the extent to which a solid can withstand stress is mathematically encapsulated by the so-called Lamé coefficients relating stress and strain [146]. At a linear level, these are just the shear and bulk modulii, the latter of which is expected to be dynamically negligible in the crust [139]. Given that the majority of work regarding oscillations or restorative forces in the crust are discussed at a linear level, and the difficulty of microphysical calculations, little is known about the higher-order coefficients in the crust. We do not discuss non-linear elasticity further here (though see [147,148]).

Still, the shear modulus μ is the leading-order quantity relevant for elastically supported oscillations and stress support. Even though there really are multiple shear modulii which depend on the shape of nuclei [149], we neglect such complications (e.g., related to the possibility of nuclear "pasta") and assume a single contributor. For the standard (i.e., spherical nuclei) shear modulus, the often-quoted expression valid at low temperatures comes from Strohmayer et al. [150], viz.

$$\mu_{\text{S91}} \approx 0.1194 \frac{n_i(Ze)^2}{a_i},$$ (3)

which is proportional to Γ. More sophisticated variants can also be found, such as that due to Horowitz and Hughto [151], who fit the results to molecular dynamics simulations,

$$\mu_{\text{HH08}} \approx \left(0.1106 - \frac{28.3}{\Gamma^{1.3}}\right) \frac{n_i(Ze)^2}{a_i}.$$ (4)

Next-to-leading-order temperature corrections are discussed by Baiko [152] and others, as are various physical corrections to these formulae (again see [139]). At the linear (i.e., Hookean) level, μ is the proportionality factor relating (shear) stress σ to the elastic strain s^{el}, viz. (e.g., [153])

$$s_{ij}^{\text{el}} = -\frac{\sigma_{ij}}{\mu}. \tag{5}$$

In GR, arriving at a similar relationship is rather more involved, though it be can achieved through the Carter and Quintana [154] relations defining the elastic stress tensor through a Lie derivative. A modern discussion on relativistic elasticity can be found in Andersson and Comer [147]. The shear stress can be related to the Lagrangian eigenfunction associated with generic motions (see Section 4.1.1) through

$$\sigma_{ij} = \tfrac{1}{2}(\nabla_i \xi_j + \nabla_j \xi_i), \tag{6}$$

where index symmetry is manifest. The perturbed metric and Christoffel symbols also appear in the GR variant of (6). Although often the Maxwell stress is used directly to define σ in works involving magnetar events, this is, strictly speaking, invalid: one must instead model the perturbative viscoelastic response to magnetic pressures, which tends to induce significantly lower strains than the Maxwell terms alone (see [106,155] for recent emphases).

3.2. Breaking Strain

One anticipates that for $\Gamma \gtrsim 175$, the outer layers (except for the *very* outer layers, being oceans and atmosphere) of the neutron star will solidify an elastic solid that can support stress up until a point where a "failure" event occurs. Such stresses can develop through multiple channels, being a general mass quadrupole moment or "mountain" (e.g., [86,141]), deformations due to gradual spin-down [112,156], differential rotation between the crust and interior neutron superfluid (i.e., spherical Couette flow; [157]), magnetic field evolution (e.g., [158]), or resonant pulsations (see Section 6). Therefore, what this threshold is—the topic of this subsection—has important implications for a variety of phenomena (e.g., [36,37,159]).

The reason for quotations around the word *failure* above is that exactly how an over-straining event manifests in the crust is not well understood. As discussed in Section 6.3, this may have applications for precursors also. The simplest type of picture one may have of failure is that of a brittle material. The elastic maximum is breached, and suddenly the region "cracks" like glass. In this way, one can envision an immediate and large release of magnetoelastic energy: field lines that were once held fixed (cf. Alfvén's flux-freezing theorem) are now free to reconnect, as the stress holding everything together falters. Jones [160] and other authors have argued against this picture, effectively because the hydrostatic pressure in the crust exceeds the shear modulus by $\gtrsim 2$ orders of magnitude, inhibiting the formation of true voids. It is likely that a more realistic picture is that of *plastic* deformations: the crust becomes overstrained and undergoes a permanent but not immutable deformation (e.g., [161]). In this case, heat is released as the region fails, and twist is injected into the magnetosphere via plastic motions, which prime it for reconnection and magnetic eruptions, leading to energy release.

The critical strain σ_{max} has been estimated through a variety of different techniques and approximations over the last ~ 50 years as collated in Table 1. It is a very difficult problem, in general, to estimate global features of the crust via molecular dynamics or other simulations, which are inherently local. For instance, the simulations of [162] apply for $\sim 10^{11}$ *femtometers* of material. As emphasised by [156], while the former authors found a global failure mechanism once the critical strain of $\sigma_{\text{max}} \sim 0.1$ is reached, it is probable that in a real crust, the failure mechanism differs because of lattice dislocations, grain boundaries, permanent or temporary deformities due to previous failures, and other mesoscopic imperfections.

Table 1. Estimates for the breaking strain, $\sigma_{\max}$, obtained from the literature, in ascending order according to publication date. This list is not exhaustive, though it roughly illustrates the plausible range of values depending on the assumptions made on crustal microphysics. The parameter $s \approx 0.185 Z^{1/3} c/v_F$ has been introduced by Kozhberov and Yakovlev [163] for electron Fermi velocity v_F.

Physical Model/Simulation Setup	$\sigma_{\max}$ (Dimensionless)	Reference(s)
Imperfect (alkali) metals	$\gtrsim 10^{-5}$	[164]
Perfect one-component crystal	$10^{-2} \lesssim \sigma_{\max} \lesssim 10^{-1}$	[165]
Li crystals (57% Mg, $T \lesssim 100$ K)	$10^{-5} \lesssim \sigma_{\max} \lesssim 10^{-2}$	[166]
Energy and event rates of magnetar flares	$\lesssim 10^{-3}$	[37]
Perfect, defective, and poly-crystal ($\Gamma \sim 834$)	~ 0.1	[162]
Perfect body-centred cubic crystal	$\left(0.0195 - \frac{1.27}{\Gamma - 71}\right) n_i \frac{Z^2 e^2}{a_i}$	[167]
Pure and imperfect crystals (various compositions)	$\gtrsim 0.1$	[168]
Maximum strain set by spin limit ($\lesssim 1$ kHz)	$0.008 \lesssim \sigma_{\max} \lesssim 0.089$	[169]
Polycrystalline crust (anisotropic, variable)	$\sim 0.04 \ (< 0.3)$	[170]
Idealised nuclear pasta ($T = 1$ MeV)	~ 0.3	[171]
Deformed mono-crystals	$\approx 0.02 \frac{\sqrt{1+1.451 s^2}}{1+0.755 s^2}$	[163]
Multi-ion (strongly ordered) crystal ($T \ll$ MeV)	$0.02 \lesssim \sigma_{\max} \lesssim 0.08$	[172]
Near-equilibrium, stretched lattice (various composition)	~ 0.05	[173]

Aside from deducing $\sigma_{\max}$, there are multiple criteria that have been considered as to how strain leads to failure. Arguably the most popular is that of the von Mises criterion, where one stipulates that

$$\sigma = \tfrac{1}{2}\sqrt{\sigma_{ij}\sigma^{ij}} \geq \sigma_{\max} \implies \text{failure.} \tag{7}$$

Another mechanism, perhaps more physical as discussed by Chugunov and Horowitz [167] and others, is the Zhurkov model [146]. The main stipulation is that thermodynamic fluctuations should exceed some threshold energy in order for the breaking to occur. It is arguably more realistic since it accounts for the fact that stress is applied over a finite time interval, which leads to a more gradual deformation of the material in question, rather than in an abrupt sense as predicted by (7). Nevertheless, because of its simplicity, the von Mises criterion is often used in the literature (e.g., [114,158,159]) and is that which we adopt in this review.

Based on the values of maximum stress that can be sustained by the crust, the most recent and sophisticated estimates of which are in the range $\sim$0.04 to $\sim$0.1 (see Table 1; at least when discounting the possibility of pasta structures in the inner mantle), one can attempt to probe the interior from multimessenger measurements (see Sections 4 and 6).

Mountains

Another way in which the critical breaking strain impacts neutron star predictions is through the maximum mountain size (i.e., mass quadrupole moment or ellipticity). While not especially relevant for premerger phenomena per se, whether or not a star has a history of GW emission could influence evolutionary channels and especially spin (Section 4.3). For example, GW radiation reaction contributes to spin-down, and thus it may be that if the maximum mountain size is small (as is predicted by modern approaches; [141]), a larger mean spin frequency in late-stage inspirals may apply. This could impact mode frequency distributions, and the plausibility of late-stage dynamo activity (as described in Section 6.5). If a neutron star taking part in a merger already has a mountain through an old pile-up of accreted material (e.g., [84]) or some other means, the effective $\sigma_{\max}$ necessary to instigate failure would be reduced. Typically though, models assume an initially relaxed (elastic) state for the crust with $\sigma(t=0) = 0$.

3.3. Stratification Gradients

The imprint of composition or temperature can be quantified introducing the convenient parametrisation

$$\tilde{\Gamma} = \gamma(1 + \delta), \tag{8}$$
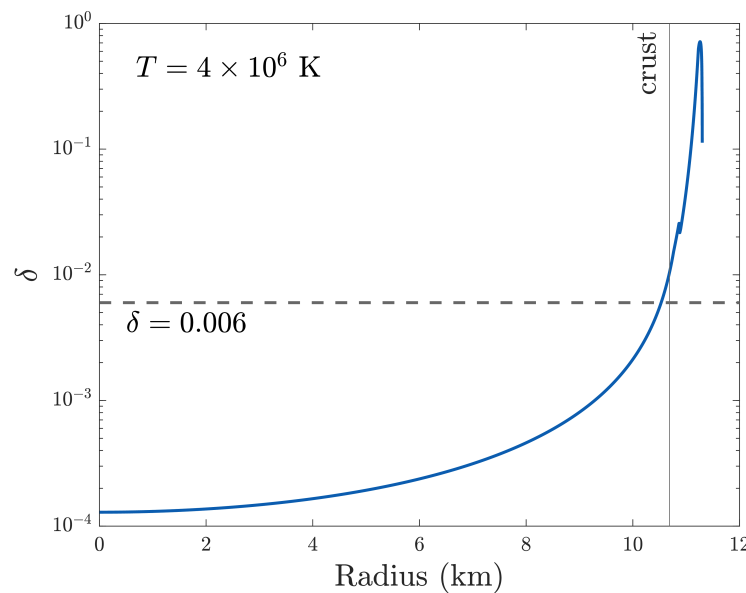
where γ is the adiabatic index associated with the beta equilibrium star $\gamma = \frac{\epsilon + p}{p}\frac{dp}{d\epsilon}$. The function (parameter) $\tilde{\Gamma}$—not to be confused with the Coulomb coupling parameter Γ— is that associated with the perturbation, generally computed in the "slow-reaction limit", where one assumes that the composition of a perturbed fluid element is frozen, and is related to the sound speed via $c_s^2 = p\tilde{\Gamma}/(\epsilon + p)$. As such, by enforcing that the Lagrangian variation of some particle (proton) fraction is zero, the neighbourhood of perturbed fluid elements is no longer in beta equilibrium, and the system supports buoyancy modes [174,175]. Generally, δ is both a function of time and space as the star heats and has position-dependent temperature and composition, with the matter such that $\delta \geq 0$ to satisfy the Schwarzschild criterion for convective stability. Compositional impacts are described above, while thermal ones can be estimated following [47] and others:
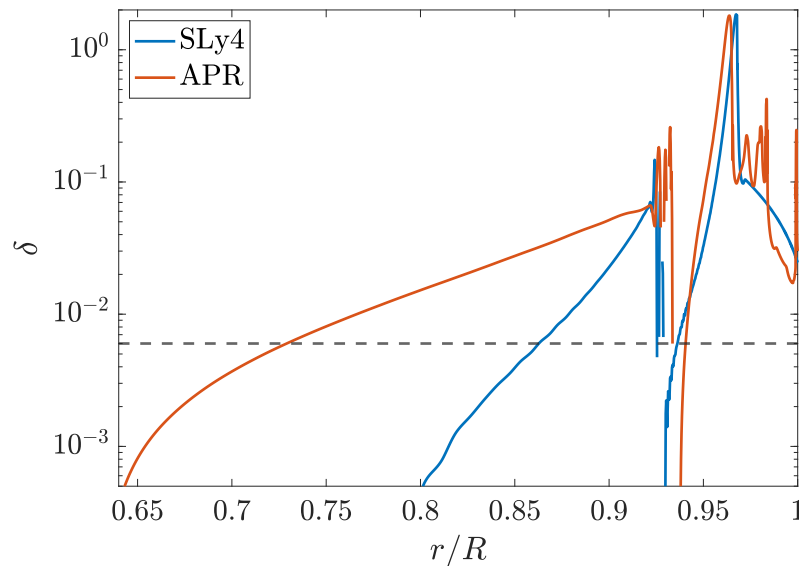
$$\delta_T(t, \boldsymbol{x}) \approx \left[\frac{k^2\pi^2}{6}\sum_x \frac{n_x(\boldsymbol{x})}{E_F^x(\boldsymbol{x})}\right]\frac{T(t, \boldsymbol{x})^2}{p(t, \boldsymbol{x})}, \tag{9}$$

for particle species x, with number density n_x and Fermi energy E_F^x, where the sum runs over the species list. Note that these latter quantities could also be treated as functions of time if chemical reactions are accounted for. The subscript T indicates a thermal contribution, clearly vanishing as $T \to 0$.

As such, a particular temperature profile and equation of state implies some value for δ that can be calculated self-consistently. Figure 4 shows one such case for an isothermal star with $T = 4 \times 10^6$ K. Taking the finite temperature SLy4 and APR EOS from the CompOSE catalog, we also show δ for a 1.41 $M_\odot$ star with constant temperature $T = 10^7$ K in Figure 5. A line corresponding to $\delta = 0.006$ is shown for reference: such a value for the stratification is considered typical for premerger neutron stars in the literature [49,176–178]. We see that a constant $\delta = 0.006$ approximately depicts the stratification in the outer regions near the crust–core interface, where the *g*-modes are mostly supported.


Figure 4. Stratification profile for an isothermal star for the (cold) SLy EOS with a mass of 1.41 $M_\odot$, where the crust–core boundary is indicated. A value of $\delta = 0.006$ is marked, considered roughly a canonical average in a number of studies (see text). The curve terminates at the stellar surface, where we do not consider ocean or atmospheric layers. Adapted from Kuan et al. [48].

Figure 5. Stratification profile for an isothermal ($T = 10^7$ K) star with a mass of 1.41 $M_\odot$ for the finite temperature SLy4 (blue) and APR (red) EOS accessible within the CompOSE catalogue. The radial coordinate is normalised by the stellar radius for the respective models.

Within Figure 5, we normalise the (coordinate) radius by the stellar radius to compare stars with two different EOSs. We truncate the domain (i.e., $r/R \geq 0.65$) to show the δ profile in the outer core and crust only, as the stratification becomes minute at lower radii (cf. Figure 4). The spiky behaviour near $0.9 \lesssim r/R \lesssim 0.95$ corresponds to densities where nuclei crush after reaching their respective saturation values [62]. Although certain types of smoothing are often performed (see [71,179]), we do not implement such filtering to the directly accessible data from CompOSE. The spiky nature of the δ profile in this case highlights the complications present when trying to calculate realistic g-mode spectra and out-of-equilibrium processes when using finite-temperature EOS. Still, the δ values are quantitatively similar to the case of (9). Strong magnetic fields could also affect the effective stratification [89].

In reality, perturbations of a neutron star will lead to a departure from the beta equilibrium, possible changes to the local viscosity, and heat propagation [180–183]. The local effect of beta gradients can kill off g-modes with a frequency lower than the reaction rate as a result of the suppressed compositionally supported buoyancy [184,185], combined with the fact that heating leads to a shift in mode frequencies (see Section 4.5). The influences of diffusive physics in the oscillation spectrum and in the tidal interaction, in the context of coalescing binary neutron stars, are still not well understood. Some recent attempts have been made with simplified models [186–188]; in particular, [189] suggested that these effects lead to a measurable phase shift in the GWs for high signal-to-noise-ratio events such that constraints on the bulk viscosity can be placed.

3.4. Superfluidity and Superconductivity

Mature neutron stars tend to be relatively cold with $k_B T \ll$ MeV. In this context, "cold" means that their thermal energies are well below the corresponding (core) Fermi energies, $10 \lesssim E_F \lesssim 100$ MeV [noting that the Fermi energy of neutrons is $E_F \approx 100 (\rho/2\rho_0)^{2/3}$ MeV; [190]. Because of the high degree of degeneracy, the neutrons and protons (and perhaps some exotica) occupying the core of the star are expected to become both superfluid and superconducting within $\lesssim 100$ yr (see [191] for a review). This was speculated on first by Migdal [192], with the first proper calculations carried out by Ginzburg & Kirzhniz [193] providing support. Since then, more elaborate calculations have been performed; see, for instance, refs. [194–196] for recent contributions based on different many-body methods.

The exact temperature at which such a transition occurs is both density- and pairing-mechanism dependent and a matter of active research, though is in the neighbourhood of $T_c \approx 10^9$ K (see Figure 1 in [197] for example). With the possible exception of some rare dynamical capture events ([198]; see also Section 4.6), stars taking part in a merger should be below this temperature. Various phases of the crust are also expected to be in such low-resistance states. As the strong interaction has an attractive component, and neutrons and protons are fermions, they are expected to form a Cooper-pair condensate at low enough temperatures, and thus neutrons in the crust are in fact likely to be superfluid [199]; by contrast, simple estimates all but confirm that that the electrons living in the neutron star crust are not superconducting (the critical temperature is practically zero).

One important aspect of superfluid+superconducting states in premerger objects concerns *g*-modes, and thus dynamical tides more generally. If the neutrons are superfluid, they do not contribute to the buoyancy that other fluid constituents experience following some perturbation, as they are free to "move out of the way" [200]. As described by Kantor and Gusakov [201] and others, the neutron component is thus essentially decoupled from the oscillations, and so the mass of some given oscillating fluid element is *smaller* by a factor that depends on the relative particle abundances. Less inertia for the same force implies a greater oscillation frequency; typically, superfluid *g*-modes have factor ≈4 larger eigenfrequencies than their normal counterparts [197,202]. This scaling of course depends sensitively on the exact EOS, the presence of temperature gradients, spin, and so on.

Treating the system with a realistic, multifluid approach and noting that leptons (electrons and muons) are the main distributors of entropy in a superfluid core [200], modes supported by leptonic buoyancy exist and may be significant also [201]. The leptonic Brunt-Väisälä frequency does not exist in the crust, however, and thus these *g*-modes are unlikely to be relevant for precursors (Section 6), though they could be for GWs, as their linear frequencies are several hundred Hz [203].

Larger frequencies imply *later* resonances as far as dynamical tides are concerned, which generally means the overlap integrals will be larger but conversely that the window in which the resonances are active will be smaller (see Section 4.1.3). Nevertheless, [202] found the net energy siphoned from the orbit into the oscillations is ∼10 times larger than the normal fluid case. This clearly may be important as concerns inferences on the nuclear EOS from GW measurements of dephasing, as even the normal-fluid *g*-modes can be significant (see later sections, and also [177]). Such an investigation was carried out by [204], with superfluid *g*-mode dephasing reaching $\mathcal{O}(1 \text{ rad})$ (see also [205]). Later resonances may, however, have a more difficult time in explaining *early* precursor flare onset times (see Section 5.5).

Superconductivity has been studied less in the premerger context. This could, in principle, distort the star significantly away from spherical symmetry [206] (which influences the tidal coupling) and shift the mode spectra through magnetic corrections, as the Lorentz force scales like $\sim H_{c1} B$, which can be large even if B is relatively small (see Section 5.4 and [207]). The lower critical field can be estimated through [see Equation (7) in [208]]

$$H_{c1} \approx 4 \times 10^{14} \left(\frac{m_p}{m_p^*} \right) \left(\frac{x_p}{0.1} \right) \left(\frac{\rho}{10^{14} \text{ g cm}^{-3}} \right) \text{G}, \tag{10}$$

for proton fraction x_p and effective (entrained) mass m_p^*. In the cores of some heavy stars under some EOSs, Equation (10) could reach $\sim 10^{16}$ G. Nevertheless, in instances where figures are shown in this work, the impacts of superfluidity and superconductivity are ignored in calculating mode properties.

4. The Mechanics of Late Inspirals: Gravitational Waves

Consider a binary, involving at least one neutron star, with component masses M_A and M_B. Ignoring complications about how the objects may reach short orbital separations *a* (this issue is reminiscent of the famous "final parsec problem", though for neutron star

mergers, the solution is likely rooted in common-envelope theory; [209]), the (quadrupole formula) GW inspiral time reads

$$\tau_{\text{GW}} \approx 5 \left[\frac{a \left(1 - e^2 \right)^{7/8}}{3 \times 10^{10} \text{ cm}} \right]^4 \left(\frac{M_\odot^3}{M_A^3 q (1 + q)} \right) \text{Myr}. \tag{11}$$

Since the pioneering works of [210,211], it has been anticipated that compact binary mergers circularise well before merger such that the eccentricity $e \ll 1$. Note the normalisation in expression (11): although it would only take light ~ 1 second to travel between two such stars, the GW radiation reaction takes $\sim$ Myr. Narrowing our attention immediately to late stages where the separation is $\lesssim 20 R_A$ for "canonical values" of the stellar radius $R_A = 12$ km and mass $M_A = 1.4 M_\odot$ (see Section 2.1), we find τ_{GW} from (11) corresponds to tens of seconds, or more precisely that

$$\tau_{\text{GW}} \approx 24.5 (a/20 R_A)^4 q^{-1} (1 + q)^{-1} \text{ s}. \tag{12}$$
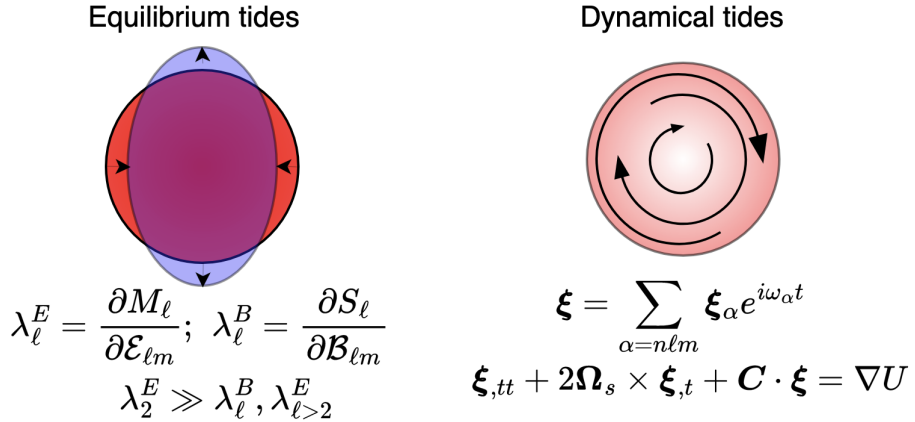
The convergence to coalescence, occurring roughly when $a \lesssim 3 (R_A + R_B)/2$ (e.g., [212,213]), accelerates rapidly in the final stages. The orbital separation can be inversely related to the orbital frequency Ω_{orb} through a Keplerian or quasi-Keplerian relationship, and thus Ω_{orb} grows in time. This sweep-up behaviour culminates in what is known as the "chirp" in the GW community.

As we explore throughout the remainder of this section, the simple result (12) is an overestimate (e.g., [214]). When considering PN or finite-size effects pertaining to *tides*, the inspiral time is reduced as additional means of energy depletion become available: the impact of tides increases as the orbital frequency sweeps up because the *tidal forcing terms* similarly increase in frequency. Obtaining a precise estimate of the tidal *dephasing* is of critical importance when trying to connect to observational data, since without accurate inference of the time relative to merger (in some appropriate frame of reference) at which some high-energy events occurs, one cannot hope to extract the maximum amount of information. More generally though, the tides encapsulate details about stellar structure, and thus, matching dephasing templates to data can be used to learn about many areas of fundamental physics.

4.1. Tides: General Theory

In the final stages of a binary inspiral, tidal effects become significant. These are usually separated into two distinct effects: (i) those associated with the "equilibrium" or "adiabatic" tides (Section 4.1.2), and (ii) those associated with "dynamical" tides (Section 4.1.3).

Within the literature, one can find a few different definitions for the qualifiers "adiabatic", equilibrium", and "dynamical" in the context of tides. For example, following [205], the word "adiabatic" emphasises that one considers deformations in the zero-frequency limit $\Omega_{\text{orb}} \to 0$. This is more typically called the equilibrium tide, though [205] made the distinction of allowing the latter to include $\Omega_{\text{orb}} > 0$ influences. Finite-frequency terms involve both non-resonant and resonant excitations, the latter of which these authors reserved for "dynamical" tide status. In other works, the inclusion of non-resonant, but time-dependent terms leads to corrections of the equilibrium quality factors which are then called "effective" (e.g., [215]). In this review, the word "dynamical" conveys $\Omega_{\text{orb}} > 0$, though we are mostly interested in resonances and their connections to high-energy phenomena. We emphasise at this stage that many of the formulae that we present are done so in a Newtonian language. When one reaches the level of wishing to actually compare results with data in a serious way, it will generally be necessary to consider fully GR expressions insofar as it is possible[4]. Given that our main purpose here is pedagogical, we avoid writing out formalisms in this way, though we point the interested reader toward the relevant literature where appropriate. A depiction of these two class of tides is given in Figure 6.

Equilibrium tides

Dynamical tides

$$\lambda_\ell^E = \frac{\partial M_\ell}{\partial \mathcal{E}_{\ell m}}; \quad \lambda_\ell^B = \frac{\partial S_\ell}{\partial \mathcal{B}_{\ell m}}$$

$$\boldsymbol{\xi} = \sum_{\alpha = n\ell m} \boldsymbol{\xi}_\alpha e^{i\omega_\alpha t}$$

$$\lambda_2^E \gg \lambda_\ell^B, \lambda_{\ell > 2}^E$$

$$\boldsymbol{\xi}_{,tt} + 2\boldsymbol{\Omega}_s \times \boldsymbol{\xi}_{,t} + \boldsymbol{C} \cdot \boldsymbol{\xi} = \nabla U$$

Figure 6. A cartoon demonstration of the difference between equilibrium and dynamical tides. The system on the left exhibits the typical (though greatly exaggerated) quadrupolar deformation, meaning that the quadrupolar, electric Love number λ_2^E is very large. In general, this implies that the mass quadrupole moment is strongly susceptible to tidal perturbations. The system on the right, by contrast, remains (approximately) spherical though has internal fluid motions excited to a large degree (i.e., strong dynamical tides). These are described by a coupled set of forced oscillation equations as detailed in Section 4.1.1.

In the Newtonian language, the essential basics of tides can be formulated as follows. Our neutron star primary, of mass M_A and radius R_A and spin angular momentum vector $\boldsymbol{\Omega}_s$, is in an orbit with a companion of mass M_B. Although it is generally expected that spin–orbit misalignment is small in late-stage binaries (cf. Section 2.2), we introduce a spin–orbit inclination angle Θ—the angle made between $\boldsymbol{\Omega}_s$ and the orbital angular momentum, denoted L. In principle, the problem can be further complicated with several additional angles if the magnetic field becomes dynamically important (magnetic inclination angles; cf. Section 2.3), the finite size of the secondary is also considered (subtended angles), or the secondary is spinning (Θ_B). These effects are almost always ignored in the literature.

Following [218] and others, we orient a spherical coordinate system around (the centre of mass of) M_A with the "z-axis" directed along L. The gravitational potential produced by M_B can then be expanded in terms of spherical harmonics $Y_{\ell m}$ (e.g., [219,220])

$$U(\boldsymbol{x}, t) = -GM_B \sum_{\ell m'} \frac{W_{\ell m'} r^\ell}{a^{\ell+1}} e^{-im'\Phi(t)} Y_{\ell m'}(\theta_L, \phi_L), \tag{13}$$

for orbital phase $\dot{\Phi}(t) = \Omega_{\text{orb}}$, and we define

$$W_{\ell m'} = (-)^{(\ell+m')/2} \left[\frac{4\pi}{2\ell+1} (\ell+m')!(\ell-m')! \right]^{1/2}$$

$$\times \left[2^\ell \left(\frac{\ell+m'}{2} \right)! \left(\frac{\ell-m'}{2} \right)! \right]^{-1}. \tag{14}$$

Here, the symbol $(-)$ is zero if raised to a non-integer power and one otherwise. Although one can work with the full harmonic expansion here, it is generally only the $\ell = 2$ and $|m| \leq 2$ terms that are observationally relevant [221,222]; for $\Theta = \pm\pi/2$, it is often only the $m' = 0$ (equilibrium tide) and $m' = 2$ (dynamical tide) terms that are relevant.

The above-described coordinate system can be related to the more natural one for describing fluid motion in the primary star. Consider now angular coordinates with respect to the corotating frame of the neutron star, with the "z-axis" now oriented along $\boldsymbol{\Omega}_s$. Fluid variables, decomposed into different sets of spherical harmonics, can thus be related through

$$Y_{\ell m'}(\theta_L, \phi_L) = \sum_m \mathcal{D}_{mm'}^{(\ell)}(\Theta) Y_{\ell m}(\theta, \phi_s), \tag{15}$$

where $\mathcal{D}^{(\ell)}_{mm'}$ is the so-called Wigner $\mathcal{D}$-function (e.g., [178,223,224]), and $\phi_s = \phi + |\mathbf{\Omega}_s|t$.

This small bit of theory is actually sufficient to specify the problem (again, at the Newtonian level): one wishes to model the response of the internal neutron star fluid to an external acceleration given by ∇U, with U given by (13). In practice, within the literature, this is achieved in a few steps using some mathematical trickery.

4.1.1. Mathematical Description and Calculation Methods

First, one wishes to solve for the "background" (magneto-)hydrostatics. For cold, mature, and not ultra-magnetised stars, this involves employing a barotropic EOS, $p = p(\rho)$, popular candidates of which are described in Section 2.1; in principle, thermal contributions can play a role at late times but these are often ignored (see Section 4.5). Once the relevant background has been constructed, a set of free perturbations is introduced for each variable X (e.g., density, pressure, gravitational potential, and velocity field) through a Eulerian scheme:

$$X \to X + \delta X + \mathcal{O}(\delta^2 X). \tag{16}$$

The linear equations of motion are conveniently expressed using displacement vector

$$\delta \mathbf{u} = \mathbf{\xi}_{,t}, \tag{17}$$

such that one obtains a "master equation"

$$\mathbf{\xi}_{,tt} + 2\mathbf{\Omega}_s \times \mathbf{\xi}_{,t} + \mathbf{C} \cdot \mathbf{\xi} + \mathcal{O}(\xi^2) = 0, \tag{18}$$

from which all[5] other variables follow [e.g., $\delta\rho = -\rho\nabla \cdot \mathbf{\xi} - (\mathbf{\xi} \cdot \nabla)\rho$]. In the above, C_{ij} is some spatially dependent tensor (defining some self-adjoint operator) that depends on the particulars of the problem under consideration (Newtonian, GR, Cowling, etc). Once some boundary conditions are imposed (e.g., regularity at the centre as $r \to 0$), the free-mode problem is fully specified.

Again, in practice, however, Equation (18) is solved through decomposition. In the irrotational case, the spatial dimensions of the problem are separated out using the spherical harmonics (15), where $\phi_s \to \phi$, depending on the *polarity* of the eigenfunction, via

$$\xi^r_\alpha(\mathbf{x}, t) = r^{\ell-1}W_{n\ell}(r, t)Y_{\ell m}(\theta, \phi) \tag{19}$$

$$\xi^\theta_\alpha(\mathbf{x}, t) = -r^{\ell-2}V_{n\ell}(r, t)\partial_\theta Y_{\ell m}(\theta, \phi) \tag{20}$$

$$\xi^\phi_\alpha(\mathbf{x}, t) = -r^\ell(r\sin\theta)^{-2}V_{n\ell}(r, t)\partial_\phi Y_{\ell m}(\theta, \phi), \tag{21}$$

for radial (W) and tangential (V) functions, where we have introduced the shorthand "α" to mean a generic set of quantum numbers n, ℓ, and m and we have

$$\mathbf{\xi} = \sum_{\alpha=n\ell m} \mathbf{\xi}_\alpha(\mathbf{x}, t). \tag{22}$$

Modes with $n > 1$ are referred to as "overtones", as n is defined by counting the number of radial nodes in the eigenfunction (see [175]). Rotation, however, generally makes a separation of variables as above impossible, and a further sum over a dummy azimuthal index becomes necessary unless one further sets up a hierarchy in powers of $|\mathbf{\Omega}_s|$ (e.g., [226]).

Finally, it is usually numerically more straightforward to evolve (18) in the Fourier domain, where one further introduces a temporal decomposition through

$$\mathbf{\xi}_\alpha(\mathbf{x}, t) = \mathbf{\xi}_\alpha(\mathbf{x})e^{i\omega_\alpha t}, \tag{23}$$

where the abuse of notation is apparent (and the carry-over to V and W in the static case is straightforward). Here we remark that ω_α is the (angular!) mode frequency in the co-

rotating frame (that is, "according to the star"); the inertial-frame ("laboratory") frequency instead reads

$$\omega_{\alpha,i} = \omega_\alpha - m|\mathbf{\Omega}_s|. \tag{24}$$

In solving mode problems, one must also take care to note that complex conjugates generally also solve the master equation, though we ignore this complication here for pedagogical purposes (see [215] for a recent discussion).

At this stage, the amplitude of the modes have not yet entered, as these fall out of the homogeneous Equation (18). Enter the tides. Formally, their accounting amounts to instead solving the inhomogenous version of the master equation,

$$\boldsymbol{\xi}_{,tt} + 2\mathbf{\Omega}_s \times \boldsymbol{\xi}_{,t} + \mathbf{C} \cdot \boldsymbol{\xi} = \nabla U. \tag{25}$$

Solving this equation is conceptually straightforward: project U into a set of spherical harmonics, as we have already done in expression (13), and repeat the above procedure, making use of orthogonality relations (taking care to ensure that one does not confuse the mode quantum numbers with the tidal field quantum numbers). This does not quite work as easily as one might hope in practice, however, because the symmetries of U are not shared by $\boldsymbol{\xi}$, meaning that the tidal field distorts the spectrum (ω_α and $\boldsymbol{\xi}$), as well as driving the system. In fact, the expansion (23) may not produce anything useful because a non-harmonic forcing term equation typically forbids harmonic time dependencies and orthogonality, and thus the ansatz involving harmonics (in both time and space) is not even necessarily well defined.

Fortunately, except possibly at very late stages in the inspiral, the tidal distortion of the spectrum is weak [227] as can be formally estimated with the formula in [175]; see Section 4.2. One thus considers a "volume-averaged" problem, where the amplitude evolution $q_\alpha(t)$ of each mode is considered in isolation. The problem is thus reduced from 1+3 to 1+0 dimensions, and we end up with some ODEs for the amplitude evolution. The key step involves introducing an inner product,

$$\langle \mathbf{A}, \mathbf{B} \rangle = \int d^3x\, \rho \left(\mathbf{A}^* \cdot \mathbf{B} \right), \tag{26}$$

between the modes ($\mathbf{A}$) and some angular harmonic of the tidal potential ($\mathbf{B}$). Crucially, this inner product defines some kind of weighted integral over *space* only. Applying this bracket to both the left- and right-hand sides of (25), one finds [218]

$$\dot{q}_\alpha + i\omega_\alpha q_\alpha = \frac{i}{2\varepsilon_\alpha} \langle \boldsymbol{\xi}_\alpha, -\nabla U \rangle$$
$$= \sum_{m'} f_{\alpha,m'}\, e^{im|\mathbf{\Omega}_s|t - im'\Phi}, \tag{27}$$

with

$$f_{\alpha,m'} = \frac{iGM_B}{2\varepsilon_\alpha} \sum_\ell \frac{W_{\ell m'}}{a^{\ell+1}} \mathcal{D}_{mm'}^{(\ell)} Q_{\alpha,\ell m}, \tag{28}$$

where the *overlap integrals*[6] read

$$Q_{\alpha,\ell m} = \left\langle \boldsymbol{\xi}_\alpha, \nabla(r^\ell Y_{\ell m}) \right\rangle, \tag{29}$$

and a spin offset is introduced through

$$\varepsilon_\alpha = \omega_\alpha + \langle \boldsymbol{\xi}_\alpha, i\mathbf{\Omega}_s \times \boldsymbol{\xi}_\alpha \rangle, \tag{30}$$

and we use the normalisation $\langle \boldsymbol{\xi}_\alpha, \boldsymbol{\xi}_\alpha \rangle = 1$.

Thus, provided the free mode spectrum can be constructed, one need "only" solve Equation (27). This, however, is still not quite the end of the story, as the orbital phase Φ

must be evolved simultaneously. By modelling the fluid motion in the neutron star as a set of harmonic oscillators [230–232] and incorporating mode kinetics into the Hamiltonian of the binary, Refs. [224,233,234] shoewd how this can be achieved with a high-order PN method, though with the modes themselves calculated in full GR without Cowling (i.e., including the metric perturbations). While not all are taken into account (such as those occurring in gravities with non-metric fields where dominant mono- or dipolar radiation exists; [235]), we list PN orders at which various effects occur in Table 2. We remark in this respect that although, strictly speaking, the radiation reaction is a 2.5 PN effect, often this is said to appear at the *Newtonian* order when using a Newtonian definition for the system's quadrupole moment(s) (see below). To avoid confusion between different conventions for PN order counting, we focus on the effects on binary motion and do not refer to the hierarchical imprints on GWs.

Table 2. A non-exhaustive list of post-Newtonian effects that influence the inspiral for compact objects. The order counting presented in the first column is quoted with reference to the power of *c* of the associated coefficient(s) in the equations of motion for binaries (i.e., N PN corresponds to a c^{-2N} scaling). Constraints on each of these orders can be found in the violin plots produced by the LVK consortium; see [13]. In principle, stellar structure and multipole moments corrections together with additional couplings enter at ever-higher orders [236]. Some additional modified gravity terms may also enter at lower PN orders; see Table 3 in Yunes, Yagi, & Pretorius [237].

Post-Newtonian Order	Effect(s)	Reference(s)
0	Energy deposited into modes	[230,231]
1	Stellar structure; pericentre advance	[238,239]
1.5	Scalar-field contributions to dynamics (non-GR)	[235,240]
1.5	Spin–orbit coupling; tail backscatter	[241]
2	Self–spin, spin–spin, quadrupole–monopole couplings, mag. dipoles	[242,243]
2.5	Quadrupole formula for GWs	[211]
3	Gravitational tails of tails	[244]
4	Dissipative tidal number	[187,188]
5	Gravitoelectric quadrupole Love number	[245,246]
6	Gravitomagnetic quadrupole Love number	[247,248]
6.5	Spin-tidal coupling	[247,249]

PN effects in shaping stellar structure have been examined in several references (e.g., [238,239,250]) and starts already at the first order, though no systematic analysis of how these directly influence the inspiral has been carried out. Tides and spins contribute hierarchically at several PN orders, accounting, for instance, for the breakdown of the point particle approximation. Tides absorb orbital energy in the Newtonian theory already (i.e., at the 0th order), while spin couples to the orbital angular momentum at the 1.5th order and to self-spin and companion spin at the 2nd order. At the 2.5th order enters the leading-order dissipation due to GW emission [cf. Equation (11)]. The electric-(magnetic-)type stationary deformations factor into the dynamics at the 5th (6th) order, as introduced in Section 4.1.2, and the coupling between this deformation to the spin follows at the next half order. GW170817 placed constraints on each of these PN orders as detailed in [13].

With the above in mind, the notion of *dephasing* can be made precise. In the stationary phase approximation, the frequency-space GW phase Ψ can be written as (e.g., [251,252])

$$\Psi(f_{\text{gw}}) = 2\pi f_{\text{gw}} t_{\text{ref}} - \phi(t_{\text{ref}}) - \frac{\pi}{4}, \tag{31}$$

where t_{ref} is a given reference time, and $\phi(t)$ is the *time domain* phase associated with $f_{\text{gw}} = \Omega_{\text{orb}}/\pi$ and the shift $\pi/4$ is conventional. The quantity Ψ can be shown to satisfy [245]

$$\frac{d^2\Psi}{d\Omega_{\text{orb}}^2} = \frac{2Q_\omega}{\Omega_{\text{orb}}^2}, \tag{32}$$

for some dimensionless Q_ω (a quality factor akin to the overlap integrals), measuring the phase acceleration, viz.

$$Q_\omega = \Omega_{\text{orb}}^2 \left(\frac{d\Omega_{\text{orb}}}{dt} \right)^{-1}. \tag{33}$$

The dephasing, called $\Delta\Phi$ here, is thus just the difference between the calculated Ψ from (31) when relevant terms are kept (i.e., the PN ones described above) as compared to when they are de facto "switched off".

4.1.2. Tides: Equilibrium

The equilibrium tide simply corresponds to the "$\Phi(t) = 0$" portion of the dynamics. In this case, the quasi-harmonic time dependence of (13) drops out, and our interest shifts to bulk, geometric deformations of the stellar surface ("zero-frequency oscillations"). The extent to which the stellar interior is susceptible to a time-independent tidal potential can be encapsulated by the (shape) *Love numbers*; effectively, much like the Q_α defined previously, these measure the extent of orthogonality between the stellar fluid (or solid) and some angular portion of the tidal field (i.e., ℓ, m'). In general, therefore, there is an infinite set of Love numbers, though often in the literature, one will find the term "Love number" just to mean the quadrupolar, $m' = 0$ Love number. In the context of compact binaries in GR, Ref. [253] first quantified how tidal Love numbers influence inspirals. Note also that if the star is static and axisymmetric at the background order, the index m' falls out of the equations and thus the static, or even effective, Love numbers are characterised by a single harmonic number ℓ. These reduced Love numbers are typically denoted as k_ℓ.

Again working in the static limit for simplicity, the Love numbers define proportionality factors weighting the multipole moments $I_{\ell m}$ of the previously spherical star when affected by the tidal field. One has [254,255]

$$G I_{\ell m} = \frac{2\ell + 1}{2\pi \ell!} k_\ell R^{2\ell+1} \mathcal{E}_{\ell m}, \tag{34}$$

where the tidal moments are defined implicitly by the relations

$$\mathcal{E}_{a_1 a_2 \ldots a_n} x^{a_1} x^{a_2} \cdots x^{a_n} = \sum_m \mathcal{E}_{\ell m} r^\ell Y_{\ell m}(\theta, \phi) \tag{35}$$

and

$$U = -\sum_{\ell=2}^{\infty} \frac{1}{\ell!} \mathcal{E}_{a_1 a_2 \ldots a_\ell} x^{a_1} x^{a_2} \cdots x^{a_\ell}, \tag{36}$$

which is the same U from (13). Note that the multipole moments $I_{\ell m}$ are also implicitly defined at some PN order; see Section V in [236]. At Newtonian order, $I_{\ell m}$ is defined through an integral over the mass-density weighted by a spherical harmonic and radius to power ℓ:

$$I_{\ell m} = \frac{16\pi}{(2\ell+1)!!} \left[\frac{\ell^2 + 3\ell + 2}{2(\ell^2 - \ell)} \right]^{1/2} \int d^3 x \rho Y^{\ell m*} r^\ell. \tag{37}$$

In a GR setting, the theory becomes somewhat more involved. The Love numbers now acquire a magnetic counterpart. This is essentially because all forms of energy gravitate and thus angular momentum deposits made by the tidal field influence the spacetime through *current multipoles*: the "gravitomagnetic" portion of the field can excite some current-like components provided the star is not static and axisymmetric [256]. Essentially one can find the correspondence [246,257]

$$\lambda_\ell^E = \frac{\partial M_\ell}{\partial \mathcal{E}_{\ell m}} \quad ; \quad \lambda_\ell^B = \frac{\partial S_\ell}{\partial \mathcal{B}_{\ell m}}, \tag{38}$$
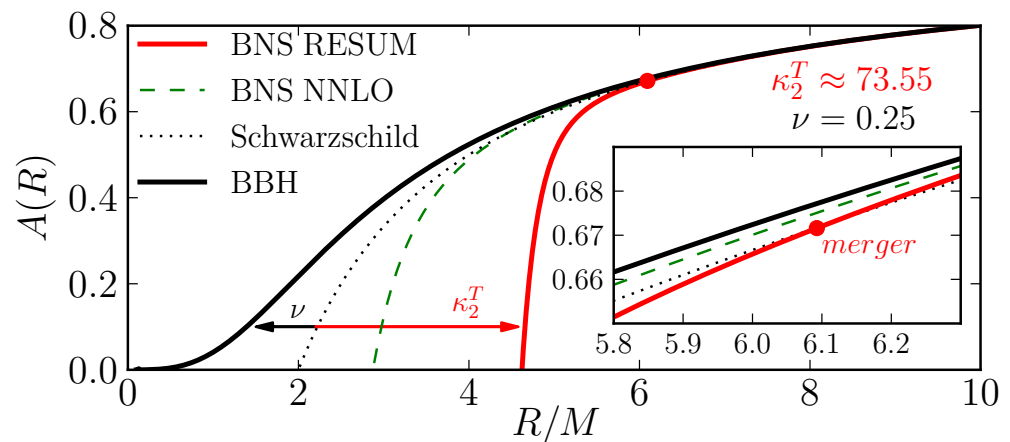
where the (axisymmetric) mass (M_ℓ) and current (S_ℓ) multipole moments can be defined either via the [236] or Geroch–Hansen [258] formulae. These formulations are compeltely

equivalent by a theorem due to [259]. In the above, we have the odd and even parity sectors of contractions of the trace-free Weyl tensor (e.g., [257,260]). Using the schemes introduced by [85,261] to generalise the Geroch–Hansen definitions to theories beyond GR, one could try to extend the correspondence (38) to some other theory of gravity. This has not yet been attempted.

Tides effectively enhance the "attraction" between the components of the binary, leading to earlier merger relative to binary black holes or point particles. The tidal dynamics are elegantly described by a radial interaction potential in the effective-one-body (EOB) formalism [262–264]. PN models of tides in the EOB formalism were initially verified against numerical simulations by [265,266], who demonstrated that the models can be improved with such calibrations but that it is not possible to accurately describe tides close to merger with a PN model. Such a restriction was lifted by [262] through *resumming* techniques. A schematic depiction of this attractive feature is shown in Figure 7, where the red curve describes the radial potential for a neutron-star binary with tidal resumming. A significant drop in the potential occurs at a larger radius, indicating the stronger attraction felt by the binary than the equivalent binary black hole. The dominant term of the tidal imprints on waveform is delivered by the quadrupole quantity [245]

$$\kappa_2^T = \frac{3}{13}\left[\frac{(M_A + 12M_B)M_A^4\Lambda_A + (M_B + 12M_A)M_B^4\Lambda_B}{(M_A + M_B)^5}\right],\tag{39}$$

for $\Lambda_A = \frac{2}{3}k_2^A(R_A/M_A)^5$ with the same definition for object B (see also [267–270]). Note that k_2 is defined in expression (34), effectively being the constant of proportionality between the quadrupole moment and the quadrupolar tidal potential (appropriately generalised to GR via the Weyl tensor; cf. Note 4).


Figure 7. The main radial gravitational potential $A(R)$—the lapse function of the effective-one-body spacetime over which the dynamics of a test particle describes the dynamics of the real binary system [271,272]—as a function of the radial coordinate $R = a$ with $M = M_A + M_B$ (for this figure only) in a tidal EOB model. The binary black hole sector of this model (solid black) shows a deviation from the lapse of the Schwarzschild spacetime (dotted), indicating the dynamics of a test particle on the effective spacetime is different from that of a (plunging) orbit around a Schwarzschild black hole due to the finite symmetric mass ratio $\nu = M_A M_B/M^2$ of the binary (which should not be confused with the our use of ν as stellar spin used elsewhere). For the neutron star case, the gravitational potential including up to the next-to-next-to-leading-order tidal effects (i.e., up to 7 PN; green dashed) is shown together with the result, resumming the gravitational-self-force information up to 7.5 PN [273] (red). The specific equal-mass neutron-star binary considered here has a tidal deformability [Equation (39)] of $\kappa_2^T \approx 73.55$. From Bernuzzi et al. [262] with permission.

4.1.3. Tides: Dynamical

Pulsation modes inside compact stars, tidally forced or otherwise, are generally characterised according to the nature of the restoring force that ultimately damps the oscillations. The theory of mode oscillations is an active and rich area of research, for which we cannot do justice in this review. We therefore refer the reader to, for example, [274–277], though a few QNM groups are particularly important in the context of GWs and tides, so we introduce them briefly.

Modes that are restored by pressure are known as p-modes, with the lowest radial quantum number ($n = 0$) mode referred to as the "fundamental", or f-mode. These modes remain non-degenerate in the spectrum in the limit that all physical ingredients (rotation, magnetic fields, stratification, ...) are discarded except for the hydrostatic pressure. Including more physics in the model will augment the p-spectrum, but the classification remains the same. Some other modes obtain a hybrid-like character when additional physics is included, in the sense that the spectrum is strongly codependent on more than one variable, such as the torsional (magneto-elastic) modes [278–280] and the inertial gravity modes [218,281,282]. The excitation of these modes during inspiral comes at the expense of the orbital energy, as described mathematically in Section 4.1.1, which can be computed using numerical techniques [202,205,225,233,283–287].

Modes that are instead restored by buoyancy are referred to as g-modes (i.e., "gravity" modes, not to be confused with GWs). The g-modes, in contrast to f-modes, do depend sensitively on the internal composition of the star (see Section 3.3) and thus may be able to reveal a different kind of information. Depending on the chemical composition of the star, the g-modes tend to follow different relations as described by [49]. That is to say, whether the EOS is purely hadronic or hybrid (for instance) has a strong impact on the scaling of the modes with the mean density, temperature, and other microphysical parameters. Generally speaking, the g-mode spectrum will be influenced by both composition and temperature (entropy) gradients. The former can be calculated from a EOS that provides the speed of sound and $d\epsilon/dp$ in a tabulated form so that the Brunt–Väisälä frequency can be determined [174,175]. A related class of modes are those associated with interfaces: realistic stars with crust–core [288], crust-envelope [289], and possibly pasta transitions, where the state of matter changes, also host a class of interface (i-) modes with eigenfunctions that peak strongly around the boundary layer (see Section 6.4.1).

The p-modes, and f-mode in particular, are especially important for astrophysical processes involving neutron stars owing to their compactness, including the tides: it can be shown that the f-mode couples most strongly to the tidal potential ∇U out of all other modes (at least for astrophysical stars, e.g., without near break-up rotation rates or virial-strength magnetic fields). The f-modes tend to have a (linear) frequency in the range of $2 \lesssim \omega_f/2\pi \lesssim 3$kHz depending on the EOS (see [290] for a review), and thus are primarily relevant in the late stages of an inspiral. The dephasing induced by the f-mode oscillation is a problem that has attracted considerable attention, where the effects are usually incorporated via the Love number as an effective dressing [264,291–295]. Considering rapidly rotating stars leads to a more complicated picture since the retrograde mode may actually come into resonance much earlier, as the inertial-frame frequency of the mode is $\omega_i = \omega_0 - m\Omega_s$ [Equation (24); see [283,284]].

In [224], the method presented in [233] to simultaneously evolve the inspiral and mode amplitudes was extended to the 3.5 PN order. In particular, the conservative dynamics, leading-order gravitational radiation, and mode excitations (see Table 2) are incorporated into a total system Hamiltonian. Solving the associated equations of motion allows one to quantify the above effects, including that of spin-modulations in mode excitation (deferred to Section 4.3). The aforementioned physics can also be incorporated into the effective Hamiltonian of the EOB formalism [264,294], where spin can also be included [295]. We note that only modes whose pattern speed is along the orbital motion can be considerably excited while there is another set of modes rotating in the opposite direction. Hereafter, we always discuss modes belonging to the former class unless stated otherwise. An important

caveat with respect to these results notes the absence of elasticity terms within the equations of motion, which could skew the results for g- and other modes to some degree as discussed in Section 6.4.2; see also [225,296]).

Figure 8 shows how the mode amplitudes evolve due to the tidal coupling that was solved for simultaneously with orbital motion (top), and the associated dephasings compared to the point particle approximation of the inspiral. The g-mode amplitudes increase rapidly when the GW frequency (f_{gw}, twice as the orbital frequency; green) sweeps through their characteristic frequencies (vertical dash-dotted), and remain roughly unchanged afterward. In this specific case, the f-mode's frequency is higher than f_{gw} at the end of evolution, and thus the mode (purple) is never resonantly excited. Although there are only four modes involved in the evolution shown in Figure 8, an arbitrary number can be considered, in principle. Still, the dephasing yielded by the f-mode excitation [$\mathcal{O}(10^{-1})$ radian] is more than one order of magnitude greater than that collectively caused by g_1- to g_3-resonances ($< 10^{-5}$ radian with 60% attributed to g_1, $\lesssim 40\%$ from g_2, with only a feeble contribution from g_3). We note that we terminate the numerical computation when f_{gw} reaches 10^3 Hz since the PN scheme is obviously invalid in that strong-gravity regime. However, the excitation of f-modes can be even more important than shown above. Given that the merger frequency can be approximated as [267]

$$f_{gw,mrg} \simeq \frac{4000\,\text{Hz}}{(M_A + M_B)/M_\odot},\tag{40}$$

f-resonances could be reached shortly prior to merger.

On the other hand, if the neutron star has a spin, the frequencies of retrograde modes will be reduced [297–300], pushing the onsets of resonance earlier in the inspiral. Of the most relevant effects in terms of waveform is the f-mode excitation in a neutron star possessing an anti-aligned spin with the orbit [223,293,295] as also demonstrated in numerical simulations (e.g., [292,301]); the effects of spin are described in more detail in Section 4.3.
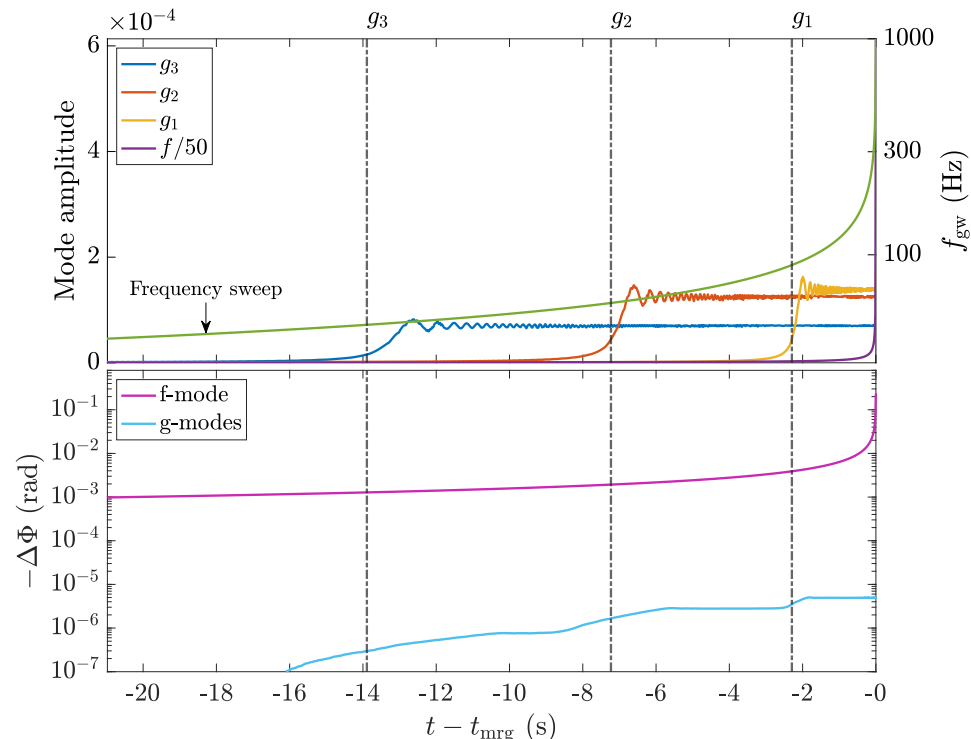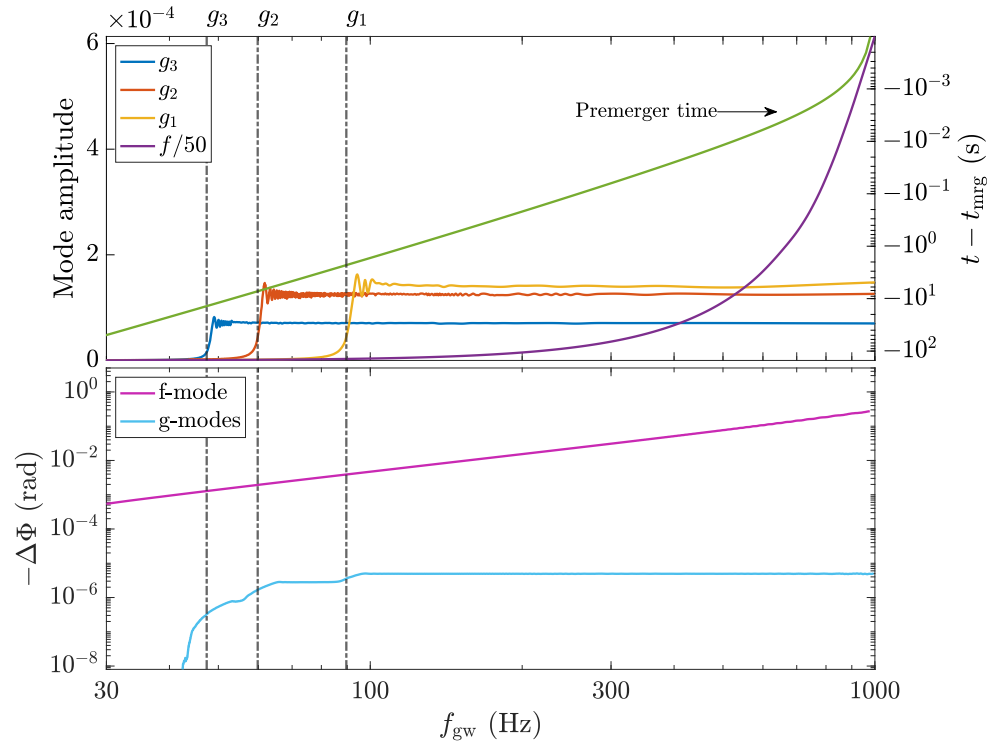

Figure 8. *Cont.*

Figure 8. (**Top panel**): self-consistent mode amplitude evolutions of f- and $g_{1,2,3}$-modes due to tidal forcing, together with the dephasing [lower; see Equation (31)] associated with the f- (magenta) and g-modes (other colors; see plot legends) as functions of time relative to the merger, $t - t_{\mathrm{mrg}}$. The GW frequency (f_{gw}) is overplotted as the green line, corresponding to the vertical axis on the right-hand axis. (**Bottom**) The same information as per the left panel though instead as functions of f_{gw}, with $t - t_{\mathrm{mrg}}$ overlaid as the green line, corresponding to the vertical, right-hand axis. The evolution is carried for a $1.35 + 1.35\,M_\odot$ binary neutron-star (i.e., $q = 1$) with the generalised piecewise-polytropic approximation of the APR EOS from O'Boyle et al. [42] (the original version of the piecewise-polytropic approximation in [302] has discontinuous $\tilde{\Gamma}$, preventing an accurate determination of g-modes' tidal properties when δ is small) with a constant stratification $\delta = 0.005$. The vertical lines mark the frequency of $g_{1,2,3}$-modes, which are 90, 60 and 48 Hz, respectively.

Current analytic waveform models include either implicitly or explicitly dynamical tides to introduce some effective dressing. In particular, Ref. [176] showed that the Love number can be expressed as a sum of the contributions of various QNMs with the f-mode dominating. As the orbital frequency increases, the tidal interaction enters a dynamical regime, where the Love number varies with tidal frequency and is often referred to as an effective Love number [264,294]. Another stream to model the dynamical tidal effects is to introduce amplification factors to the leading-order tidal effects to blend in higher-order PN contributions [263,267,303,304]. Phenomenological fittings to numerical simulations have also been developed [305–308] (see also [309]).

4.2. Spectral Modulations: General Considerations

In reality, the free-spectrum consisting of all the modes described above and more will also be perturbed due to the tidal hammering, as the interior structure of the star is now also perturbed; the relative shifts for the *angular* frequencies, $\delta\omega_\alpha$, can be deduced from the leading-order [175] formulae. Given some perturbing force $\boldsymbol{F}$, the eigenfrequency correction reads, in the Newtonian context (see Refs. [224,228] for GR generalisations),

$$\delta(\omega_\alpha^2) = 2\omega_\alpha \delta\omega = \frac{\int dV \boldsymbol{F} \cdot \boldsymbol{\xi}_\alpha^*}{\int dV \rho |\boldsymbol{\xi}_\alpha|^2}. \tag{41}$$

The above can be evaluated for any given perturbing force, which is subdominant with respect to that of the hydrostatics. Given that spin, magnetic fields, and thermodynamics play a significant role in premerger phenomena beyond just mode modulations, these are covered in their own subsections in Section 4.3, Section 4.4 and Section 4.5, respectively.

4.2.1. Tidal Corrections

The perturbing tidal force is given by

$$\boldsymbol{F}^{T} = \rho \nabla U. \tag{42}$$

It is straightforward to evaluate expression (41) for (42) for any particular QNMs as was performed, for example, by [310] for f- and r-modes and [224] for g-modes. The former found for Maclaurin spheroids the simple result

$$
\begin{aligned}
\frac{\delta \omega_f^{\text{Tidal}}}{42.3 \text{ Hz}} = & -q \left(\frac{\alpha_f}{0.1} \right)^{-1} \left(\frac{M_A}{1.4 M_\odot} \right)^{3/2} \left(\frac{R_A}{13 \text{ km}} \right)^{3/2} \\
& \times \left(\frac{a}{100 \text{ km}} \right)^{-3} \left[1 - 0.21 \left(\frac{\nu}{300 \text{ Hz}} \right)^{-1} \right. \\
& \left. + 0.055 \left(\frac{\nu}{300 \text{ Hz}} \right)^2 \right],
\end{aligned}
\tag{43}
$$

for mode amplitude α_f directly proportional to the overlap integral (29) [see Equation (10) in [310]]. The result matches that of more realistic EOS to within a factor ~ 2, and is typically small; see also [227]. For g-modes, the shift is expected to be of order $\sim 0.01\%$ and can be safely ignored [224].

4.2.2. Curvature (Frame-Dragging)

Accounting for the fact that frequencies differ between the neutron-star and laboratory frames because the star is embedded in a region of strong curvature can be important [294,311,312]. The gravitational redshift factor can be deduced from the metric lapse function, if available from a numerical simulation. To the PN order, though, and ignoring spin corrections (i.e., Lense–Thirring and quadrupolar corrections to the timelike component of the metric), one finds [see Equation (3.6) in [294]]

$$z_B \approx 1 - \frac{5 G M_B}{4 a c^2} = 1 - 0.03 \left(\frac{M_B}{1.6 M_\odot} \right) \left(\frac{100 \text{ km}}{a} \right), \tag{44}$$

where one anticipates $\omega_{\alpha,i} \mapsto (1 + z_B) \omega_{\alpha,i}$ for an inertial-frame frequency $\omega_{\alpha,i}$. For resonances applying some seconds prior to merger, we expect separations within the resonance window to be of order $a \gtrsim 100$ km. As expression (44) shows, a frequency shift of at most a few percentage points would therefore apply. By contrast, the redshift at moments closer to merger may seriously impact the high-frequency (e.g., f- or superfluid g-) mode resonances [294]. On the other hand, frame-dragging effects counterbalance this static effect: Ref. [295] found that at late stages of an inspiral, there are near cancellations and the effective z_B may be small.

4.3. Spin Effects

As far as premerger phenomena are concerned, rotation is no less important than in other instances of neutron-star astrophysics. Primary effects are due to the fact that intrinsic angular momentum (i) alters the equilibrium shape of the neutron star; (ii) introduces a Zeeman-like splitting of the modes, which introduces prograde and retrograde bifurcations, the latter of which can potentially be unstable to the [313–315] (CFS) instability; (iii) impacts the efficacy of tidal couplings depending on spin–orbit (mis)alignment; and also (iv) influences the inspiral directly through spin–orbit, spin–spin, and self–spin couplings.

This list is not exhaustive, as rotation also influences the evolutionary track of stars in complicated ways, though the above effects are what we concentrate on in this work, as they are directly applicable to the premerger phase. We give a brief description of the above points (i)–(iv) here, commenting more throughout as appropriate.
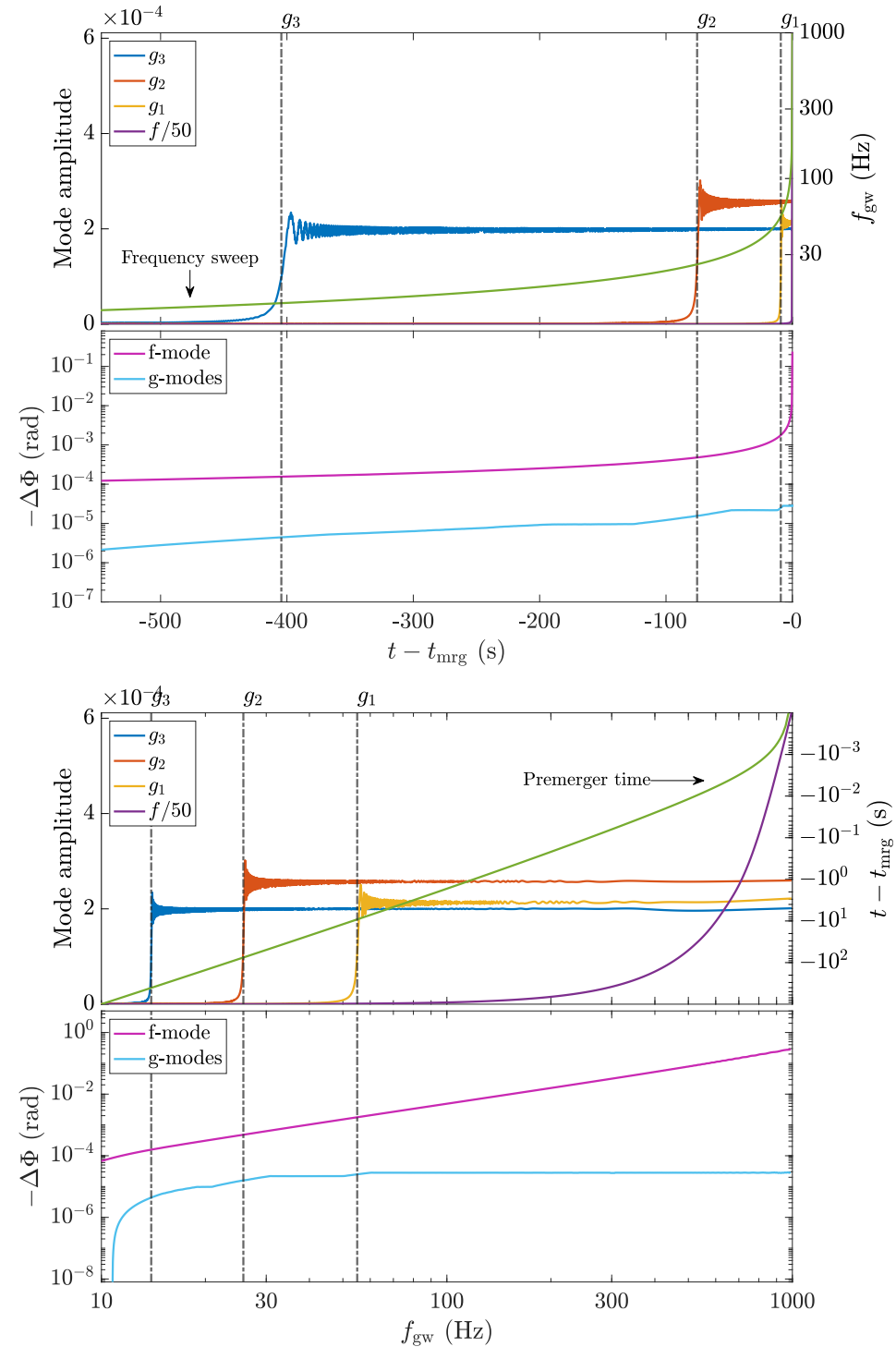
(i)   Centrifugal forces deform the star starting at order $\mathcal{O}(\Omega^2)$. For a uniform density object, the rotational oblateness is estimated by $\epsilon_{\rm rot} = 5\Omega^2/4\Omega_k^2$, where Ω_k is the Keplerian break up value (e.g., [316]). In much the same way that equilibrium tides impact the evolution through a quadrupolar deformation, so too does the rotation (e.g., [317]).

(ii)   Modes are generally split into prograde and retrograde families through the azimuthal number m. That is to say, when $\Omega_s \neq 0$, the mode frequencies and eigenfunctions depend on m, which can be either positive or negative. This splitting leads to a more complicated set of couplings and dynamical tides (as described in Section 4.1.3). Moreover, if the star is spinning sufficiently fast such that $\omega_{\alpha,i} < 0$ while $\omega_\alpha > 0$, an allegedly retrograde mode instead appears as prograde in the inertial frame (24)—from which radiation reaching infinity is measured—and thus is subject to the Chandrasekhar–Friedman–Schutz (CFS) instability [313–315,318].

(iii)   Spin–orbit misalignment changes the Wigner coefficient and hence the tidal coupling, which couples in with point ii above.

(iv)   Spin–orbit coupling, independent of tides, is important and modifies the dephasing of GW from 1.5 PN order in a way that a spin anti-aligned with the orbital motion tends to accelerate the merger, while an aligned spin works to delay the inspiral [241,319–321].

As soon as one accounts for spinning stars, the geometrical description becomes considerably more complicated. A few additional angles are introduced relating to the directionality of the orbital angular momentum versus that which is intrinsic to the stars. If we consider just a single star to have spin, we need only introduce a single angle, introduced as Θ in expression (15) (e.g., [218]), representing the single surviving misalignment angle. If we have alignment but a significant spin, the effect is that of earlier resonances. In the anti-aligned case, it is the lower inertial-frame frequency branch of modes that is most strongly excited by the tides [223]. This generally implies a stronger tidal influence, as earlier resonances imply a longer period of time to drain the orbit. On the other hand, a later resonance for some modes could imply a greater dephasing since, again typically, larger overlaps are achieved for higher eigenfrequencies. Larger amplitudes are especially relevant for precursor observations since the crust is likely to be more susceptible to a greater strain exerted over a short period of time rather a moderate strain over a marginally longer window. This is the case for the von Mises criterion at least, which only considers the maximum strain (see Section 3.2).

Simultaneous mode and orbital evolutions for arbitrary misalignment angles ($\Theta \neq 0, \pi$) were calculated by [48] for g-modes and [284] for f-modes. Physically, non-zero misalignments allow for the excitation of odd azimuthal mode-numbers ($m = 1, 3, \ldots$) depending on the Wigner coefficient, and can reach relatively large amplitudes. For a system spinning at even a modest rate $\nu \gtrsim 2$ Hz but with a significant misalignment angle $\Theta \sim 80°$, it was shown that the resonant pulsations from both $m = 1$ and $m = 2$ modes could theoretically break the crust, leading to the emission of two time-separated precursors (as observed in GRB 090510, for instance; discussed in more detail in Section 5). Whether multiresonances allowed by significant misalignment are relevant for GW dephasing has not yet been calculated in detail in the literature.
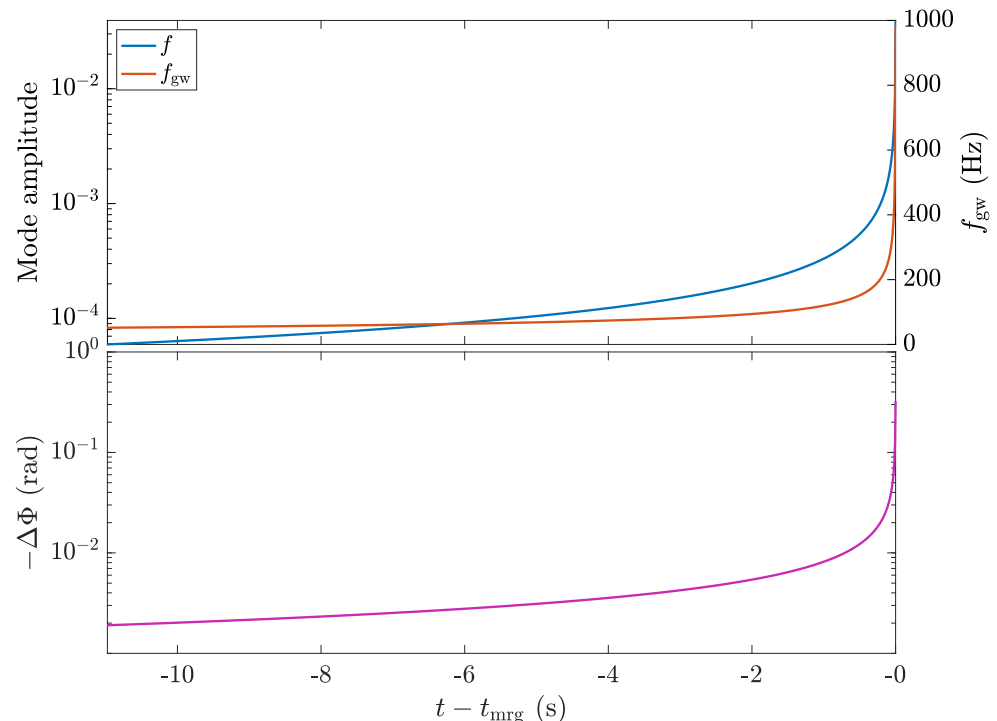
Figure 9 demonstrates the impact that moderate rotation ($\nu = 20$ Hz) can have with respect to resonance timings and associated dephasing. Noting the difference in scale between both time and the vertical axes on the plots relative to Figure 8, several effects are visible. The g-mode are particularly affected by earlier excitations of modes: for the static case, it is clear that the g_1-mode amplitude is largest, while that title instead goes to g_2 in terms of raw amplitude when $\nu = 20$ Hz. At the same time, retrograde g-modes may be smeared out if their frequencies are reduced by spin to be slower than the chemical reaction

rate of neutron star matter (Section 3.3), which is about $\lesssim 10^2$ Hz ($\sim$ mHz) assuming that the direct (modified) Urca reaction is the dominant beta-decay channel [184,185]. That is, locally, the Brunt–Väisälä frequency should be higher than the chemical balancing rate. In principle, one could also use the above ideas to test whether the direct Urca channel can operate in neutron stars, a topic that has received much attention lately (e.g., [57]). That is, if *g*-mode dephasings at low frequencies were conclusively ruled out, that would provide strong evidence for direct beta-decay channels. Such ideas have yet to be thoroughly investigated in the literature.

Figure 9. Similar to Figure 8, though assuming the primary neutron star spins at 20 Hz in the opposite direction to the orbital angular momentum (i.e., anti-aligned with $\Theta = -\pi$).

For the spinning case depicted in Figure 8, the g_3-mode is probably not realistic in light of the above (though see also [322]). That said, if being conservative to assume that the chemical reaction rate is at the mHz level, then the g_1- to g_3-modes will be eliminated when the neutron star spins at 51, 35, and 28 Hz, respectively. Therefore, the only relevant mode in a rapidly spinning neutron star ($>10^2$ Hz misaligned with the orbit) is the f-mode, and possibly the interface and/or r-modes (see Section 6.4), though these latter modes are not incorporated here. This is demonstrated in Figure 10 for a star with spin $\nu = 200$ Hz: the g-modes are washed out of the spectrum based on the above predictions (even if not mathematically at the level at which we set up the problem), and only the f-mode remains, whose frequency is reduced from the static value 1955 Hz to 1727 Hz. Even in this case, however, the mode does not become resonant [see Equation (40)]. The dephasing is, therefore, in this case, the weakest of all considered thus far, though it could increase with higher spins [205,284]. This demonstrates the complicated, non-linear dependence that stellar spin has on GW observables. Including spin within merger simulations is especially difficult, though it was first successfully implemented by [323].


Figure 10. Similar to Figure 8, though for a star spinning with $\nu = 200$ Hz in the opposite direction of the orbit. In this case, the (retrograde) g-modes are completely washed out of the spectrum due to reaction rate considerations (see text).

Tidal Spin-up

In addition to the direct energy deposits from the orbit, tidal interactions torque each of the neutron stars. From a resonant interaction alone, Ref. [324] showed that a net angular momentum transfer of

$$\Delta J_{\alpha,\text{res}} = \int dt \int d^3x \, \delta \rho_\alpha \left(-\frac{\partial U^*}{\partial \phi} \right) \tag{45}$$

can be expected. An upper bound to the bulk spin-up of a given star can then be obtained by assuming that $\Delta J_{\alpha,\text{res}}$ contributes only to the uniform rotation of the star, so that $\Delta \Omega_{\alpha,s} \sim \Delta J_{\alpha,\text{res}} / I_0$. For f-modes, where the tidal overlap reads $Q \gtrsim 0.1$, the above estimate indicates that a non-negligible spin-up of order unity may occur, albeit only in the very final moments

of merger [see also Equation (6.2.6) in [285]]. For a $1.4 M_\odot$ pair of stars, the general result is (e.g., [310])

$$\frac{\Delta\Omega_{\alpha,s}}{\Omega_s} \lesssim 0.2 \left(\frac{30\,\text{Hz}}{\nu}\right) \left(\frac{\omega_{\alpha,i}}{1\,\text{kHz}}\right)^{-5/3} \left(\frac{Q_\alpha}{0.01}\right)^2. \tag{46}$$

For g- and other non-f-modes, the effect is likely subleading, though it could achieve $\Delta\Omega_{\alpha,s}/\Omega_s \gtrsim 0.01$ for favourable overlaps. The long-lived tidal-grinding provided by the non-resonant f-mode could also be significant. Either way, such effects complicate the dynamics of the system considerably, as one must, in general, account for a time-dependent spin factor in modelling the tidal dynamics. Such modelling has not been attempted aside from the work of [324] for neutron stars, and in the different contexts of binaries involving a white dwarf by [325,326].

It is actually expected that the tidal torques will primarily induce differential rotations instead of bulk motions, essentially due to relation (17). This differential rotation can excite convective motions and invites the possibility of premerger dynamos; see Section 6.5.

4.4. Magnetic Effects

Magnetic fields control all of the electromagnetic phenomena associated with neutron stars, including those occurring premerger (see Sections 2.3 and 3.2). Dynamical magnetic fields can also generate electric fields via induction, which work towards accelerating the binary inspiral [242].

As described by [327] and others prior (beginning with [328]), suppose that the magnetic field of the primary greatly exceeds that of the companion so that the latter may be treated effectively as a perfect conductor with a vanishing dipole moment. The orbital motion of this companion through the rotating magnetosphere of the primary generates an electromotive force, driving a "direct current" between the constituents, with the closed magnetic field lines playing the role of wires in the circuit. This is the so-called "unipolar inductor" model, which will be covered in some more detail in Section 6.2. The exact way in which EM energy is siphoned out of the orbit depends on the total resistance of the circuit, $\mathcal{R}$, which includes contributions from the primary, companion, and the (intertwined) magnetosphere. Ref. [327] argues that the maximum energy dissipation rate reads

$$\dot{E}_{\text{EM}} = -T_{\text{mag}}(\Omega_{\text{orb}} - \Omega_s) = \zeta_\phi (\Omega_{\text{orb}} - \Omega_s)\frac{\mu_d^2 R_B^2}{2a^5}, \tag{47}$$

for electromotive torque T_{mag}, primary (equatorial) dipole moment μ_d, and twist parameter ζ_ϕ. This latter parameter relates to the induced toroidal field due to kinetics as is familiar from studies of low-mass X-ray binaries (e.g., [83]), though its value is highly uncertain: it depends on poorly understood boundary-layer physics.

In fact, Ref. [329] suggested implicitly (i.e., in a different notation) that the twist could reach values much larger than unity, $\zeta_\phi \gg 1$, which could significantly accelerate the inspiral. Furthermore, the torque T_{mag} will generally spin up the primary when $\Omega_{\text{orb}} > \Omega_s$; Ref. [329] argued this could lead to near synchronisation and thus to rapidly rotating stars prior to merger if the dipole moment is sufficiently large (cf. Section 2.2). On the other hand, if the magnetic pressure exerted by the toroidal field is too large, the flux tubes defining the circuit will be broken by unstable kink modes. This is the essence of the argument put forward by [327] regarding the limiting value of the twist ($\zeta_\phi \sim 1$), and hence a relatively weak electromagnetic contribution (47). Still, quasi-periodic circuits may be established if after such a flux tube breaks, reconnection between the (inflated) field lines re-links the two stars so that the cycle may repeat. Understanding the dynamics of such a system requires 3D simulations, which have not yet been conducted; see [330], who found that ζ_ϕ could greatly exceed unity in cases where the stellar spins are anti-aligned with respect to each other.

To gain a rough sense of the impact, we can integrate the torque–balance equation

$$\frac{d}{dt}\left(\frac{1}{2}I_0\Omega_s^2\right) = \dot{E}_{\text{EM}},\tag{48}$$
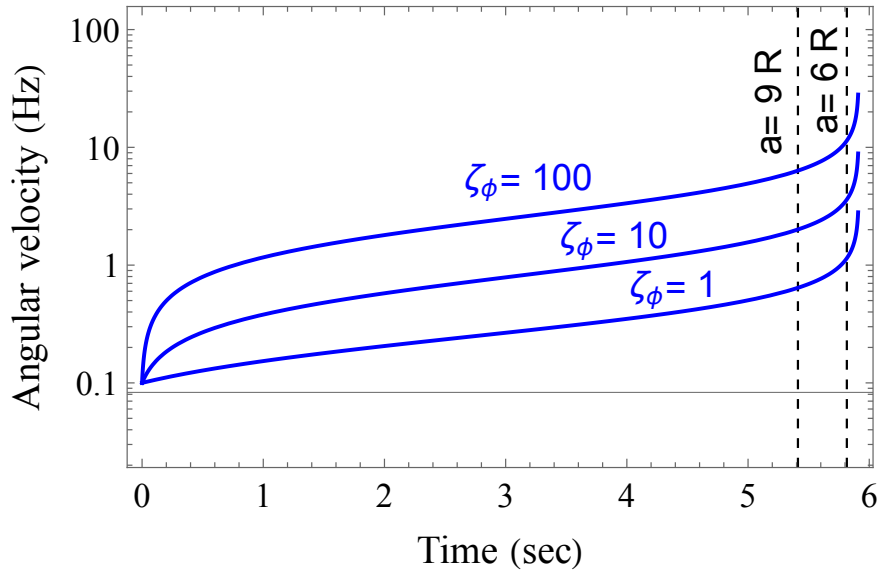
which, provided we take $\Omega_{\text{orb}} \gg \Omega_s$, has the solution

$$\Omega_s(t) \approx \left(\Omega_{s,0}^2 + \mu_d^2\frac{R_B^2}{2I_0}\int dt\,\frac{\zeta_\phi\Omega_{\text{orb}}}{a^5}\right)^{1/2},\tag{49}$$

where we ignore the dipole spin-down and field decay taking place in the final seconds or minutes. If we take a constant value for ζ_ϕ and further use the leading-order GW orbital decay rate (cf. Section 4),

$$\dot{a} = -\frac{64G^3}{5c^5}\frac{M^3q(1+q)}{a^3},\tag{50}$$

together with $\Omega_{\text{orb}}^2 \approx GM(1+q)/a^3$, we can evaluate expression (49) easily. One set of results for various values of ζ_ϕ is shown in Figure 11, where we postulate a magnetar-level field at the equator of $\sim 10^{14}$ G, radius 12 km, moment of inertia $I_0 = 10^{45}$ g cm^2, and two $1.4M_\odot$ stars ($q = 1$). The evolution is tracked starting from a separation of 200 km ($\Omega_{\text{orb}} \approx 216$ Hz). The magnetic star is practically static initially with $\Omega_{s,0} = 0.1$ Hz, though half a second before merger ($a \approx 9R$), it can reach non-negligible spins if the twist parameter is large ($\zeta_\phi \gtrsim 1$). For the case $\zeta_\phi = 10^2$—still significantly less than that estimated by [329] for some systems—the spin frequency can reach $\nu \gtrsim 1$ Hz when $a(t) \sim 9R$. Larger field strengths amplify the effect further like $\sim B^2$. If some magnetars with larger fields take part in mergers, as hinted at by some precursor observations (see Section 6), spin-up could be dynamically impactful. These spin-ups will combine with those of the tidal torques discussed in Section Tidal Spinup.


Figure 11. Estimates for electromotive spin-up in the final seconds of inspiral, following expression (49), for a magnetar with equatorial field strength $B \approx 10^{14}$ G and an unmagnetised companion. For large twists ($\zeta_\phi \gg 1$), spin-up could be significant and contribute to dephasing through the effects described in Section 4.3.

Internal Fields?

Magnetic effects can also be associated with those of the interior, rather than the exterior. A strong tension can either reduce or increase the tidal deformability of a star depending on the nature of the magnetic geometry: poloidal (toroidal) fields tend to induce

an oblate (prolate) distortion. This was studied by [331] and more recently by [332] using complementary techniques, though the results are rather pessimistic: relative shifts in the deformabilities Λ [see below Equation (39)] amount to $\lesssim 0.1\%$ for $B \lesssim 10^{15}$ G for neutron-star EOS. For quark-star EOSs, the effects are greater. In a superconducting core, the result may also be somewhat larger if $H_1 \sim 10^{16}$ G (e.g., [206] and Equation (10)), which leads to a factor $\gtrsim 10$ increase in the effective magnetic tension and hence a percent-level shift for magnetars. Tidal deformabilities for stars with superconducting components have not been calculated in the literature. Some additional effects could arise if the internal magnetic fields are large enough to distort the stellar EOS, though these must be typically larger than even H_{c1} (see [8,89]). A recent discussion on mathematical elements of GRMHD equilibria can be found in [333].

4.5. Thermal and Viscous Effects

As quantified by Equation (25), tidal energy is siphoned into QNMs during an inspiral. This energy is essentially in the form of the potential and kinetic energy associated with the master eigenfunction ξ. As detailed by [128] and [327], three ways in which these modes can be damped is through GW radiation reaction, chemical relaxation through neutrino emission, and viscous dissipation. The first of these is largely irrelevant (though note that the damping time of f-modes can be of the order ~ 100 ms, which could theoretically be fast enough if a very early resonance occurs because of rapid rotation; see Section 4.3).

Viscous heating is likely to play a significant role. As described in [48] and elsewhere, the stellar stratification is generally a function of time because of this heating, implying that the g-mode *spectrum* itself is time dependent (this gets even more complicated if accounting for nuclear reactions; [186]). In particular, Ref. [285] has shown that the *non-resonant* $\ell = 2 = m$ f-mode in an aligned (or non-rotating) binary will increase the star's temperature by [see Equation (8.30) therein]

$$T_{\text{vis}} \approx 3.6 \times 10^7 \left(\frac{3R_A}{a} \right)^{5/4} \text{K}, \tag{51}$$

where it is assumed that the heat content is determined solely by the thermal energy of a non-relativistic, degenerate, free-neutron gas. For a superfluid star, the relativistic electrons dominate this latter quantity of interest, and expression (51) is increased further by a factor of $\gtrsim 2$.

It has been suggested that T could reach values considerably larger than (51). Arras and Weinberg [334]—who also provided an overview of the tidal heating literature in their introduction—found that chemical heating, driven by the induced fluid motions during inspiral, could raise the temperature to $\sim 2 \times 10^8$ K if the system has access to the direct Urca mechanism. This is because density perturbations excited via tides force the system out of beta equilibrium, instigating chemical heating. If the core contains "strange" matter such that non-leptonic weak interactions raise the bulk viscosity by a couple orders of magnitude (e.g., hyperonic matter), tidal heating could even raise the temperature to $\lesssim 10^{10}$ K [335]. Such enormous temperatures would have a significant impact on the g-spectrum of the system, leading to dephasing, aside from that which is associated with the heating directly. The latter effect would likely exceed ~ 0.1 rad and thus be detectable with the LVK network [335]; see also Section Crust Melting. In the limit of totally efficient tidal dissipation, the core temperature would easily reach $\sim 10^{10}$ K before merger as calculated by Meszaros and Rees [336].

If the system were to reach even a fraction of such values, the effective Love number should decrease because extra thermal pressures cause the outer boundary ($p = 0$) to extend. Using various EOS, Kanakis-Pegios et al. [337] calculated the quadrupolar Love numbers at fixed temperatures finding that for $T \sim 1$ MeV ($\sim 10^{10}$ K), there is a decrease in k_2 of order $\approx 20\%$ with a $\approx 70\%$ drop for $T \sim 5$ MeV; the tidal deformability, however, is largely insensitive to the temperature since the radius increases to compensate for the

reduced k_2 for the EOS considered therein. High temperatures would also impact the elastic maximum of the crust (Section 3.2).

A super-to-normal fluid transition due to intense heating ($T > T_c$) could also lead to a rapid shift in the already-excited g-mode spectrum. Such a rapid transition could lead to "glitch-like" phenomena in the waveform as the system undergoes a premerger phase transition. Practically speaking, crude estimates for how bulk heating will influence the g-modes can be made, noting that variations in the stratification δ obey the relation $\Delta\delta/\delta = 2\Delta T/T$ since $\delta \propto T^2$ from expression (9). One can then recompute spectra with $\delta \to \delta + \Delta\delta$ at each timestep. This could combine with a discontinuous jump in the frequencies of order ~ 4 from the above super-to-normal transition (see Section 3.4). Efforts to self-consistently account for such changes are in progress.

Overall, thermal elements in mergers are rather subtle and not fully understood beyond the above. For example, it is pointed out in [186] that out-of-equilibrium elements in a merger lead to a softening of the EOS in some density regions and to composition changes that affect processes that rely on deviation from equilibrium, such as bulk viscosity, both in terms of the magnitude and the equilibration timescales inherent to the relevant set of reaction rates. Whether the estimates described above may apply in a realistic merger environment, including the possibility of constraining them, is not obvious. Significant tidal heating of the stars can also induce mass loss via winds before merger [336], which could lead to electromagnetic, premerger emissions if strong shocks develop in the winds. Such debris will also contribute to the dynamical and post-merger ejecta polluting the eventual crash site, which could inhibit jet formation and affect the breakout timescale (see Section 6.1). If the stars reach high-enough premerger temperatures, the bulk viscous timescales calculated in [338] could be utilised.

Crust Melting?

Heat imparted due to tides reduces the effective Coulomb parameter Γ in a space- and time-dependent way (see Section 3.1). It has been suggested that, actually, the entire crust may melt prior to coalescence because $\Gamma < 175$ is achieved [339] (see also [186]). This is plausible in some of the scenarios described above. If indeed the crust undergoes a kind of global elastic-to-plastic transition at late times, Ref. [339] argued that the heating rate due to tides and (resonant) modes would increase significantly, as a liquid is more susceptible, which can manifest at the level of the waveform through a $\mathcal{O}(0.1\ \text{rad})$ dephasing. However, according to estimate (51), the crust may not reach its melting point even by coalescence, unless the viscosity assumptions made by [285] underestimate the degree of heating. A melted crust obviously cannot yield either, meaning that the melting time t_{melt}, relative to coalescence, sets an upper limit to a resonant failure time to explain a precursor (see Section 6.3). This would rule out f-mode-induced failures altogether for large bulk viscosity. Increasing the width of the liquid layers near the surface of the star would also strongly impact the spectrum of ocean modes; see Section 6.4.3 and [340]. A discussion on the theoretical elements of mode-induced crust melting can be found in [341].

4.6. Residual Eccentricity

Aside from canonical formation channels involving a symbiotic binary (see Section 2.2), mergers might occur in globular clusters where captures are not irregular. Although the recent Monte Carlo simulations of [198] estimate a globular cluster merger rate of only $\sim 0.02\ \text{Gpc}^{-3}\ \text{yr}^{-1}$, such systems may retain a significant eccentricity, as the usual circularisation arguments made in Section 4 following the [210] formulae do not apply. Tidal phenomena in eccentric inspirals acquire additional complexity because resonances can be triggered at different orbital phases (likely near periastron), and thus generally will happen earlier; multiple resonances can also be triggered each passage.

It has been shown that for eccentric binaries, there can be chaotic growth in the modes, with the kinetic energy stored in a mode rivalling that of the orbital binding energy $U \sim GMm/a$ after many cycles [342,343]. Given that this energy greatly exceeds that

which is typically expected to be stored in resonant modes, $E_{\rm kin,max} \sim 10^{45}$erg, it would be worthwhile to revisit such studies but for neutron stars specifically [344–346]. One such study was carried out by [347], finding appreciable effects depending on a complicated relationship between the eccentricity and how much energy is siphoned into the f-mode; see also [348].

4.7. Remarks on Merger Simulations and Future Challenges

Here, we provide a brief discussion on merger simulation results *with respect to mode excitations*; we direct the reader interested in GRMHD details more generally to [17,21]. Although the mode evolution is not as transparent as in Figures 8–10, some fully relativistic simulations may resolve the excitation of the f-mode in the last < 100 ms of an inspiral, given that the dephasing between the numerical waveform and the analytic model including realistic f-mode effects is small [292,295,301]. Aside from the f-mode, numerically capturing the excitations of other (polar) modes that could experience a resonance (viz. g-, i-, shear-, and ocean modes) are currently out of reach due to a number of technical and theoretical challenges. This is important since g-mode dephasings in particular may not be totally negligible (discussed recently by [177] for instance) and represents a future challenge for the numerical relativity community. Failing to account for such dephasings, if large, could lead to spurious inferences about the neutron star structure.

Spatial resolution is not the only technical requirement to see the excitation of lower-frequency modes. In such cases, one would need to start the simulation at a time when the orbital frequency is less than ~50 Hz to include their resonance windows. This corresponds to many seconds prior to merger (cf. Figure 8). This is borderline impossible, owing to both the computational demand and numerical stability considerations when coupled with the above resolution demand, at least in a full numerical relativity sense, where the spacetime is evolved self-consistently with (magneto-)hydrodynamics using the full Einstein equations. For higher quantum numbers ($g_{n \geq 2}$, ...), even greater resolution is required, and the problem becomes more severe still. On top of this, the g- and other modes' tidal response tends to be rather shallow compared to that of the f-mode (see [225,233,285,349] and others), and thus numerical dissipation can easily bias the results, i.e., convergence is expected to be much harder to obtain than the f-mode case. This is in addition to the usual separation problem of the real and imaginary components of g-modes (e.g., [224]).

From a theoretical perspective, most (though not all) of the long-term inspiral simulations adopt a cold EOS through a piecewise-polytropic approximation, which does not include the crust structure and cannot support the thermal and compositional stratification gradients that exist in a real star. Therefore, all of the microphysically dependent modes may not even exist in the first place within the computational setups employed. It is thus even difficult to estimate how many CPU hours and further code innovations would be needed to accurately simulate the evolution of these modes and claim it was either resolved or not resolved (cf. [186]). The highly dynamical nature of the spacetime and fluid makes it also not obvious whether "modes" even exist in the usual sense of the word, as these are inherently linear, while the Einstein equations are inherently non-linear (see [148,350] for discussions).

5. Precursor Flares: Observations

It has been well accepted since the dual discovery of GW 170817 [11] and GRB 170817A [12] that neutron star binary mergers are at least in part responsible for *short* GRBs. Some mergers may, however, also produce *long* bursts as described in Section 5.2. We thus use the phrase *merger-driven* to encompass this wider class of GRBs.
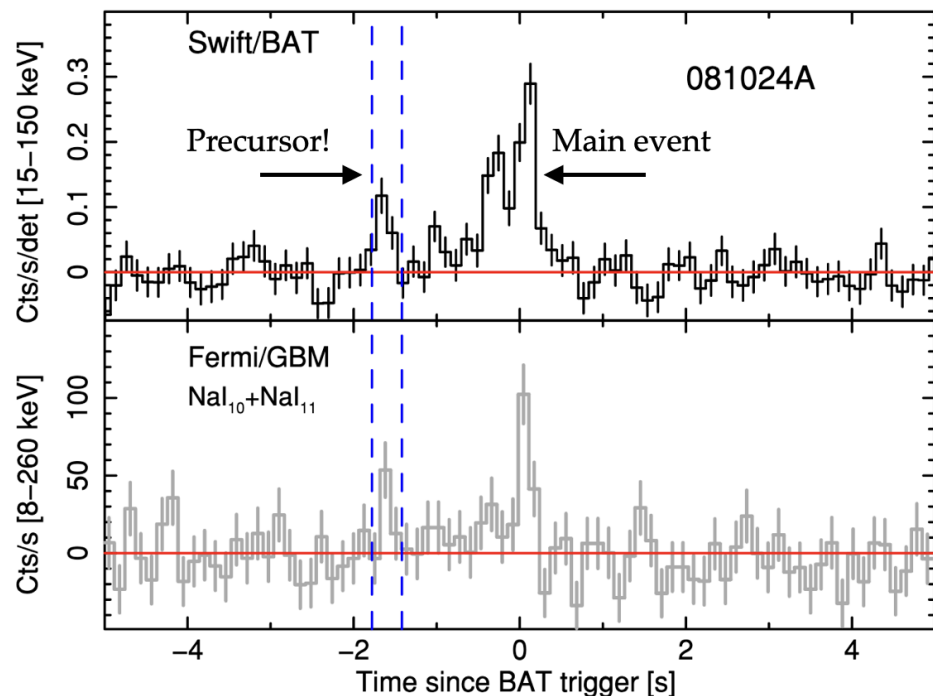
A small percentage (Section 5.3) of merger-driven GRBs display precursor phenomena, where energetic flashes are observed even many seconds prior to the main event in some cases (e.g., [25,351–353]). Based on jet delay physics (Section 6.1), there is good reason to suspect that least some of these events, such as the GRB191221A precursor measured $\sim$ twenty seconds prior to the respective GRB [27], ignite during the premerger stage. Some

precursors may be attributed to post-merger phenomena, however: the precursor from GRB150922A had only a ~30 ms waiting time, which is considerably less than the ~1.7 s delay observed in GW/GRB170817 [12]. Such post-merger phenomena could be related to the nature of the jet, possibly interacting with the dynamical ejecta, launched by the post-merger remnant (e.g., in cocoon or choking jet models; see Section 6.6). It is thus unclear what fraction of precursors occurs before *merger*, even though they occur before[7] the *GRB* by definition.
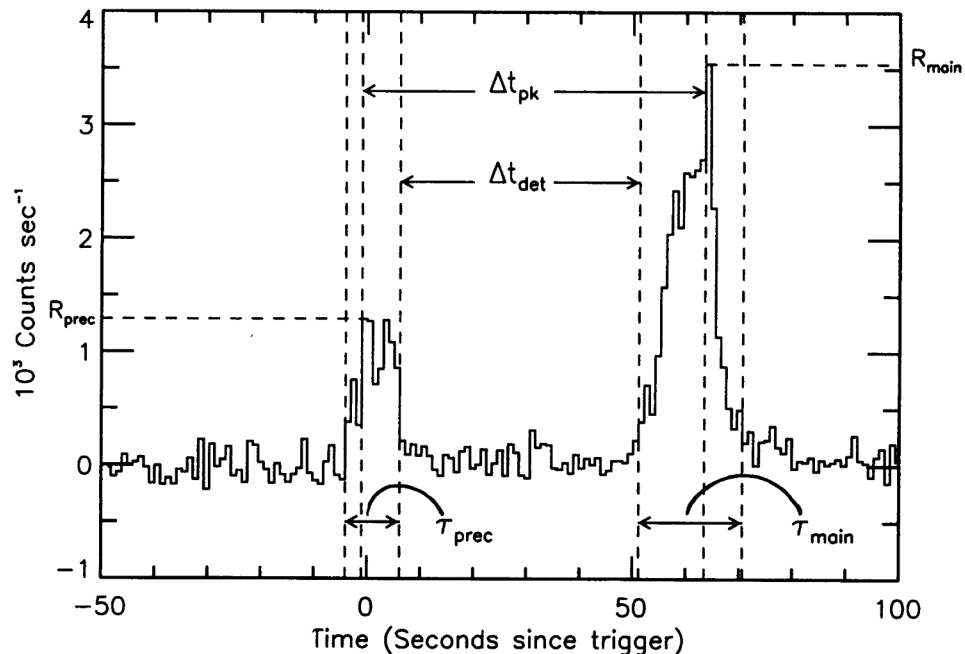
Before proceeding to precursor observations, we remark that following LVK's O3b run, searches for GWs were carried out for a variety of GRBs that took place during the observational window, regrettably without any success [354]. Some of these GRBs were associated with precursors, placing some (very mild owing to source distance) constraints on event nature.

5.1. Statistical Preliminaries

Light curves for a prototypical precursor—that associated with GRB 081024A—are shown in Figure 12, adapted from Troja et al. [352]. The event and precursor were observed by Swift and Fermi with a clear coincidence and separation time of ~ 1.5 s. What one ought to call the *waiting time* (as is the terminology we use) is, however, not obvious and occasionally inconsistent in the literature. For instance, [353] reported a *quiescent* time for 081024A as ≈ 0.91 s, meaning the time from the precursor end to the main burst beginning, which is clearly shorter than that between the peak precursor flux and main event beginning. These definitional differences are important to account for if one wishes to compare in earnest with real, astrophysical data. Although applying for long bursts, a visual depiction of the different timescales is shown in Figure 13 from the pioneering precursor observations described by [351]. Though their nomenclature of peak (Δt_{pk}) and detectable (Δt_{det}) waiting times did not persist in the literature, it is clear that even factor $\gtrsim 2$ differences in waiting time can occur if different definitions are applied.


Figure 12. Light curves for GRB 081024A from Swift/BAT (**top panel**) and Fermi/GBM (**bottom**). The significant precursor event is delineated by the vertical blue lines as marked by the arrow. Adapted from Troja et al. [352] with permission.

Figure 13. Diagrammatic representation of different types of timescales for precursors and GRBs. For short GRBs in particular, these distinctions can lead to significant factors separating reported waiting times. Reproduced from Koshut et al. [351] with permission.

Aside from this issue, statistical algorithms used to hunt for precursors can offer rather different values for event lengths or waiting times. For the case shown in Figure 12 for 081024A, Ref. [353] found that the precursor took place between -1.65 and -1.59 s prior, while [352] reported -1.70 prior to -1.45. The event duration is different by a factor ~ 4 between these. While this review cannot cover all the statistical nuance, readers should be aware that results shown by us and others in the literature are sensitive to a variety of systematics, including that associated with different instrument observations. For example, in Figure 12, it is clear that the waiting time may be different if one were to use only Fermi or Swift data: this could, in principle, be attributed to either instrument systematics or the bandwidth of emitted photons.

5.2. GRBs: Short, Long, or Ultra-Long?

Historically, GRBs have been classified according to their T_{90} durations: long bursts have $T_{90} > 2$ s while short bursts have $T_{90} \leq 2$ s. It has long been postulated that these two classes of burst are associated with different progenitors; the long ones with "collapsars" or some kind of active core collapse (e.g., [17]), and the short ones with merger events involving at least one neutron star (e.g., [18]).

As it often does, nature proves more complexity: in 2010, an "ultra-long" burst was detected, GRB 101225A (so-called "Christmas Burst"), observed by Swift and boasting a staggering 28 min duration. This led some authors to introduce a third classification for such ultra-long bursts. Additionally, it has been suggested that the Christmas burst originated from a merger, though not necessarily involving two neutron stars (e.g., [355]). Moreover, although predicted already by [356], *kilonovae* are now routinely observed (including after GW170817; [357]). These transients involve bright, broadband electromagnetic emissions due to the radioactive decay of heavy *r*-process nuclei that are produced and subsequently ejected quasi-isotropically during the merger process. They are thought to be a signature of a binary neutron-star coalescence and can be searched for with a variety of instruments owing to their broadband nature; a detailed discussion on kilonova detectability, with current and future detectors, is provided by [358].

Some notably long bursts have been accompanied by kilonovae, thereby making it even less clear whether the usual T_{90} classification can be used to distinguish between collapse or merger scenarios. For instance, Yang et al. [359] examined the late-time afterglow data from GRB 060614—a burst with $T_{90} \gtrsim 100$ s— finding a (candidate) *r*-process-powered merger nova. Such complications are the reason we use the words *merger-driven GRBs* when talking about precursors. Indeed, all GRB classes show precursors with varying statistics, with about $\sim 9\%$ of the global GRB population showing precursor activity (see [25]). Long bursts seem to display precursors more often than short ones, though (cf. Section 5.3).

Some particularly relevant examples are GRBs 211211A [10] and 230307A [9], with durations of 50 and 35 s, respectively. Both of these events are likely associated with binary mergers due to kilonovae and heavy-element production. They also both display precursor phenomena (see Section 5.5 and Table 3 below). It is probable, therefore, that some merger-driven precursors have historically evaded analysis because there is an inherent assumption that the GRBs are fuelled by an isolated object. The above discoveries highlight the need for a new classification scheme for GRBs, which influence the precursor inferences covered in this Section; see [360] for ideas in this direction. With the recent advent of the James Webb Space Telescope (JWST), classification schemes are likely to improve in the coming years.

Table 3. Precursors (likely) associated with merger events, organised in descending order of waiting timing relative to main event, with remarks on special features (if any). Key: XAM = X-ray afterglow with internal plateau, suggestive of a magnetar remnant as identified by [361] and others (e.g., [362]). Most data were compiled by [16], though others not listed there come from Minaev and Pozanenko [363] (071030), [353] (100717, 130310A, 170726794), [33] (230307A), and [26] (180703B). The long-form Fermi GBM catalogue name is used for some GRBs. Some precursors may be post-merger.

Source	Precursor Duration (s)	Relative Delay (s)	GRB Duration (s)	Remarkable Features
150922A	$0.05^{+0.01}_{-0.01}$	$0.03^{+0.01}_{-0.01}$	$0.08^{+0.01}_{-0.01}$	Peak flux larger than that of the main pulse
100223110	$0.02^{+0.03}_{-0.01}$	$0.08^{+0.02}_{-0.03}$	$0.12^{+0.01}_{-0.01}$	-
080702A	≈ 0.31	≈ 0.13	≈ 0.64	XAM; Stable magnetar?
160804180	$0.16^{+0.02}_{-0.02}$	$0.17^{+0.02}_{-0.02}$	$0.26^{+0.02}_{-0.02}$	-
170709334	$0.46^{+0.01}_{-0.27}$	$0.17^{+0.30}_{-0.07}$	$0.15^{+0.07}_{-0.04}$	Thermal precursor and main GRB
111117A	$0.18^{+0.05}_{-0.03}$	$0.22^{+0.05}_{-0.06}$	≈ 0.46	XAM; Stable magnetar? Debated T_{90}; $z = 2.211$
100702A	≈ 0.04	≈ 0.23	$0.16^{+0.03}_{-0.03}$	XAM; $t_c \approx 178$ s
180703B	~ 1.5	~ 0.3	~ 1.54	Thermal spectra; long-duration precursor
060502B	≈ 0.09	≈ 0.32	≈ 0.24	Debated T_{90}
100827455	$0.11^{+0.05}_{-0.04}$	$0.34^{+0.06}_{-0.06}$	$0.09^{+0.02}_{-0.01}$	Debated waiting time [353]
230307A	≈ 0.4	≈ 0.4	≈ 33 s	LGRB but Kilonova? $L_{\text{prec}} \approx 3.6 \times 10^{50}$ erg/s(!)
090510 (I)	$0.05^{+0.07}_{-0.03}$	$0.52^{+0.04}_{-0.08}$	$0.30^{+0.01}_{-0.01}$	Double! XAM; $z = 0.9$; peaks in 15–50 keV band
081216	$0.15^{+0.05}_{-0.03}$	$0.53^{+0.04}_{-0.05}$	$0.24^{+0.02}_{-0.02}$	Debated spectra [26]
071112B	≈ 0.01	≈ 0.59	≈ 0.27	-
150604434	$0.17^{+0.25}_{-0.01}$	$0.64^{+0.02}_{-0.29}$	$0.21^{+0.03}_{-0.02}$	-
100213A	≈ 0.44	≈ 0.68	≈ 0.94	-
181126A	$\approx 0.72^{+0.18}_{-0.27}$	$0.85^{+0.40}_{-0.29}$	$0.46^{+0.11}_{-0.13}$	-
081024A	≈ 0.06	≈ 0.91	≈ 0.94	Debated T_{90}; XAM; Collapse time ≈ 125 s?
211211A	≈ 0.2	$1.08^{+0.20}_{-0.20}$	≈ 35	LGRB; Kilonova; QPOs main and prec(!); XAM
140209A	$0.61^{+0.08}_{-0.08}$	$1.10^{+0.08}_{-0.08}$	$1.03^{+0.04}_{-0.06}$	Debated T_{90} (≈ 2.4 s?); LGRB?; Strongly thermal
101208498	$0.17^{+0.12}_{-0.08}$	$1.17^{+0.1}_{-0.14}$	$1.03^{+0.03}_{-0.04}$	-
141102A	$0.06^{+0.10}_{-0.06}$	$1.26^{+0.11}_{-0.15}$	$0.48^{+0.04}_{-0.04}$	Thermal spectra
170726794	~ 0.08	~ 1.53	~ 0.25	-
170802638	$0.015^{+0.17}_{-0.11}$	$1.85^{+0.14}_{-0.21}$	$0.33^{+0.04}_{-0.04}$	-
071030	0.9 ± 0.2	~ 2.5	2.7 ± 0.5	Data appear lost (see [353])? Debated T_{90}
100717	~ 0.15	~ 3.32	~ 1.23	Strongly non-thermal. Debated T_{90}
130310A	0.9 ± 0.32	4.45 ± 0.8	~ 2.15	Debated spectra [364]; Magnetar flare? QPOs
180511437	$2.80^{+1.38}_{-1.69}$	$12.72^{+1.80}_{-1.57}$	$3.33^{+0.18}_{-0.24}$	LGRB? Debated T_{90}; Longest precursor
090510 (II)	≈ 0.4	≈ 12.9	$0.3^{+0.01}_{-0.01}$	Double! Peaks around ~ 300 keV
191221A	$0.03^{+0.59}_{-0.03}$	$19.36^{+1.24}_{-3.19}$	$0.37^{+0.26}_{-0.13}$	-

Excluded Events

In sections that follow regarding merger-driven precursor properties, a few candidate events, discussed in the literature, are excluded here. These are the (possible) precursors associated with GRBs 050724, 080702A, 091117, and BATSE trigger 2614 (3B 931101).

The first two of these are described by [352], and are remarkable, in that the waiting times exceed ~ 100 s. The authors remark several times, however, that they "are unable to confidently determine whether they are real features", as they were not seen by instruments other than Swift and are of relatively low significance. Although the possibility of such a long waiting time could offer exciting insight into the neutron star structure (cf. Figure 9), we do not comment on these events further here. The final BATSE event is described by [351], also with a very long waiting time of ~ 75 s. The significance is, however, similarly unclear (as is perhaps visually evident from the fourth-to-last panel seen in their figure 3). Note that a precursor from 080702A but much closer to the main event was found in [27]; it could be, therefore, that this is the second example of a known double precursor event after 090510 (see Section 5.6.5). In the case of GRB 0911117, Troja Troja et al. [352] found a significance of only $\sim 1.8\sigma$ and Zhong et al. [353] remarked that the data can no longer be downloaded from the Swift archives (although this event may have also been recorded by Suzaku). We exclude this otherwise unremarkable event also (waiting time $\sim$2.7 s).
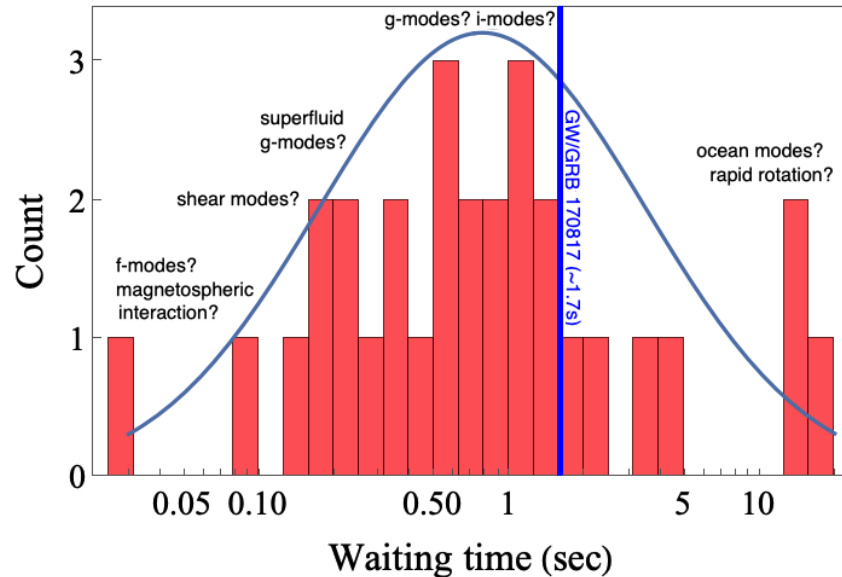
5.3. Rarity

Uncertainties notwithstanding with respect to the long-short classification issues detailed above, classifications for *merger-driven* precursors also depend on a variety of systematics. For instance, some authors require that a genuine precursor must precede the main burst by more than the burst T_{90} (e.g., [352,363]). This would mean there is a clear separation of timescales (as in Figure 13), and not a possible blur period, where it is unclear whether the precursor is related to burst ramp-up (cf. GRB 150922A). Some other studies allow for arbitrarily short waiting times relative to the main burst for early flashes to qualify for precursor status (see [25,27,353] for discussions).

Another more obvious issue relates to sample size and instruments, with some events only being seen by Fermi, and/or Swift, and/or INTEGRAL (some events even by Agile, KONUS, Suzaku, Messenger, and HEND-Odyssey [363]; cf. Table 3). As such, one has to make a statistical decision about the significance required to define a precursor *with respect to one or more instruments*. Taking a high cutoff for some information criterion (e.g., Akaike or Bayesian) will naturally reduce the event rate and hence predict that precursors are rarer. As noted by [310] and others, even these deceptively small systematics can change event rate predictions from $\sim$0.4% [363] to $\sim$10% [352], with the most recent studies falling somewhere around a few percentage points. If we included some long bursts as part of the sample, as argued to be reasonable in Section 5.2, the event rate would adjust further. Without a clear criterion for separating merger-driven and formed-in-isolation GRBs, it is very difficult to formally estimate precursor rarity, and thus this remains an open problem in our view. The problem also goes the other way: is it strictly necessary to have a merger to form a short GRB (see [365])? This issue has also been discussed by [27] in light of the fact that even deducing T_{90} is prone to systematics.

The next standout problem is deducing the rarity of the subset of precursors that are launched *premerger*. It is likely that not all precursors are in fact launched premerger; if we took the GW/GRB 170817A waiting time of $\sim$1.7 s as canonical, about $\sim$25% of precursors would be associated with the inspiralling stars themselves (see Figure 14 below). The delay time is, however, rather sensitive to the post-merger environment. High-resolution, numerical studies show that black holes typically launch jets within $\lesssim 10^2$ ms, while metastable neutron stars (if able at all; see Section 5.7) tend to take longer (see [23] and the references therein). Black hole environments are typically cleaner, as baryon pollutants from dynamical or post-merger ejecta that could drag the jet and reduce its Lorentz factor are swept under the event horizon, leading to shorter breakout timescales (see [366] for a

discussion). These issues are discussed in more detail in Section 6.1. Even so, combining the above, we may estimate that binary mergers of the order $\gtrsim 1\%$ involving at least one neutron star display a *premerger precursor*.


Figure 14. Histogram of precursor waiting times (cf. Section Excluded Events), overlaid with the best-fit lognormal distribution and several indicators for potential (premerger) precursor ignition mechanisms. Note taht these waiting times are *relative to GRB, not the merger*: the solid blue line marks the delay observed in GW/GRB 170817. Data are from Table 3 and references therein.

5.4. Spectral Inferences

Spectral information about a precursor may be useful in reducing the uncertainties detailed above, as well as landing on a likely candidate for the ignition mechanism. As described in detail by [288,367], one may anticipate less thermality in cases where magnetic fields are dynamically dominant, at least with respect to premerger models. Essentially, the matter boils down to how important backreactions are. If the local magnetic fields in the region where the flare originates are strong, energy may be more freely transported along open field lines (via Alfvén waves; see also Section 6.5) without scattering that would otherwise tend to thermalise the spectrum. If instead the field is relatively weak there, cross-field transport is hardly prohibited, and scattering can take place en masse. A typical decider in this matter will be how strong the magnetic energy density is compared to the precursor luminosity, with [288]

$$B \gg 10^{12} \times \left(\frac{L_{\text{prec}}}{10^{46} \text{ erg s}^{-1}} \right)^{1/2} \text{G} \tag{52}$$

leading to a strongly non-thermal spectrum.

In the above, we introduce the precursor luminosity, L_{prec}. Deducing this quantity from observations is non-trivial, and few events in the literature have had luminosities reported. The difficulty stems from the fact that one needs to translate (i) photon counts into fluxes, and then (ii) fluxes into luminoisites. For the former, this depends on the energy band of the instrument(s) and often requires delicate extrapolation between instruments (see [368] for a discussion on common pitfalls). The latter requires knowledge of source redshift, often not recorded at the times of publishing because it requires hunting through astronomical databases for coincident events (there may not be any). One must also be careful in deducing a kind of averaged luminosity as opposed to a peak one since the gamma-ray flux will, of course, be time-dependent. Thus far, no clear understanding of the precursor luminosity distribution is available in the literature (though see [26] for a recent

study). It should also be understood that L_{prec} refers to an *isotropic* luminosity, and thus could actually be lower if there is a non-negligible amount of beaming (see Section 6.3.1).

Many bright precursor flares tend to exhibit a non-thermal spectrum (see Table 2 in [353] for instance). This would be expected if Alfvén waves propagating along open field lines are the primary means of the associated energy transport as detailed above, though this requires high field strengths and brings its own set of issues (cf. Section 2.3). Regardless, brightness combined with non-thermality has led directly to the suggestion that some mergers contain magnetars (e.g., [33,35,310,352,369]). Precursor rarity may therefore be directly related to the prevalence of magnetars in mergers. Explaining how a strong field can persist into merger, even in $\lesssim 1\%$ of the population, remains an open issue under this interpretation. One possibility is that the field is not preserved at all but rather *generated* just before merger from convective instabilities triggered by mode-driven differential rotation; see Section 6.5.

As some specific examples, Wang et al. [27] noted that the (bright) precursors in GRBs 111117A and 160804180 strongly favour non-thermal fits. These both had short waiting times relative to the main event, and could thus favour a magnetospheric interaction or high-frequency mode resonance (see Section 6 for a review of theoretical elements). Zhong et al. [353] noted a strong favouring for a non-thermal, cutoff power-law in the (dim) precursor from GRB 130310A, which occurred $\sim$4 s prior to the main event. The precursors of GRBs 081216 and 141102A, both with delay times of $\sim$1 s, can be convincingly fit with a blackbody [16]. They may therefore be associated with weak fields, or some kind of shock-breakout model. The absence of thermal components in the extremely bright precursor from GRB 211211A ($L_{\text{prec}} \approx 7 \times 10^{49}$ erg s^{-1}; [35]), which occurred $\sim$1 s prior to the main event, could theoretically be expected from either a Poynting-dominated outflow from a remnant or possibly premerger magnetar interaction. Systematising such an analysis would constitute a useful addition to the literature, though spectral fittings can be notoriously complicated, and this, therefore, extends yet another observational problem. Some recent efforts towards systematic, spectral classification were carried out by [26].

5.5. Waiting Times

Merger-driven precursors exhibit a range of GRB-relative waiting times, from $\sim$30 ms (150922A) to $\sim$20 s (191221A). Table 3 presents relevant data from the literature, including the main GRB name, the duration of the precursor, the time delay between the precursor and GRB, the GRB duration, and some comments on remarkable features (if any). The waiting time distribution is illustrated graphically in Figure 14, showing that a reasonable fit is obtained with a lognormal distribution. Overlaid are a number of possibilities relating to premerger explanations as described in Section 6.

It is evident that there is a significant spread of precursor phenomena, with a couple orders of magnitude separating the shortest and longest waiting times and also durations. It is probable therefore that there are multiple ignition mechanisms, involving either pre- or post-merger phenomena; the physics pertaining to delays is discussed in Sections 6.1 and 6.3.3. We remark on the nature of some entries in Table 3, as some have error bars, while others do not. In [27], from which many of our tabulated precursor results are quoted, the authors did not give a confidence interval attached to the $\pm$ values they provided. As per standard convention, these error bars may correspond to 84.13% confidence upper and lower limits containing the 68.27% confidence interval [370]. In some other studies, such as [353,363], waiting times were given as a kind of mean value from T_{90} data (see Section 5.1), which we quote here using the $\sim$ symbol. Owing to these differences in notation and convention, on top of other systematics described thus far, caution should be applied when weighting precursor significance across different studies.

5.6. Some Exceptional Precursors

Here, we go into some more detail about some precursors with remarkable properties. These events may be particularly useful in deducing information about the neutron-star EOS and other fundamental physics.

5.6.1. GRB 211211A

GRB 211211A was accompanied by a kilonova [371]. This by itself is exciting: the GRB was long ($T_{90} \gtrsim 30$ s), and yet the association with a kilonova identifies the origin as a merger event (see Section 5.2). Aside from this, the event showed a precursor flare ~1 s prior to the main event [35]. In Suvorov et al. [372], the precursor timing was matched with a *g*-mode resonance with a sufficiently large overlap such that the crust may break, within the resonant failure model (see Section 6.3). Since magnetic fields skew the mode eigenfrequency, the magnetic field strength that was obtained ($\gtrsim 10^{14}$ G) was required to be consistent with that set by the extraordinarily high isotropic luminosity ($\sim 7 \times 10^{49}$ erg s^{-1}) and the absence of thermal emissions in the precursor (see Section 5.4).

In addition to that described thus far, the duration of the *main event* may also point towards magnetar participation in the merger. Kiuchi et al. [373] found in GRMHD simulations with merging magnetars that the accretion disc that comes to surround the remnant is itself highly magnetised. Although not seen in their simulation, it has been proposed that this, combined with the magnetic field sourced by the remnant if a neutron star, can set up a barrier that episodically chokes the accretion flow, thereby prolonging the event duration (see [35] and references therein).

The 211211A precursor was also modulated by quasi-periodic oscillations (QPOs) at ~22 Hz [35] (see also [374]). Seismic excitations in the crust is a natural prediction of failure: a deep quake relieves energy from the crust, which then causes the surroundings to vibrate through aftershocks. These aftershocks are most conducive to torsional modes, as initially pointed out by [375], which happen to have frequencies in the ~20 Hz range. The combination of having mass estimates for the binary members from the kilonova [371], estimates for the internal properties and magnetic field strength from a *g*-mode (or other) resonance, *and* estimates for the shear modulus in the crust from the torsional mode frequency proves intriguing. Although a thorough parameter space scan was not performed by Suvorov et al. [372], it was shown that conventional assumptions on the EOS (Figure 2) and shear modulus from the recent literature can accommodate all of the observed properties. More precisely, the frequency of the precursor QPO (interpreted as a torsional mode) and relative timing of the precursor itself (interpreted as a *g*-mode resonance) can be well fit with a star that has kilonova-inferred mass $M = 1.25\,M_{\odot}$ [371] with the APR EOS (Section 2.1.2) and shear modulus computed from nuclear physics (Section 3.1). Other interpretations are valid, though. For example, the QPO could be associated with a magnetoelastic mode (e.g., [279,280]) and the precursor could be attributed to an interface-mode (e.g., [288,367]; see also Section 6.4.1).

5.6.2. GRB 180703B

The 180703B precursor is unusual because of the event duration. As found by [26], the precursor emissions began ~1.8 s prior to the main burst, lasting all the way until a lull at ~0.3 s, followed by the GRB of a similar duration. The delay could therefore be longer depending on what one calls the waiting time (again see Section 5.1). The authors, however, denoted this precursor as a "gold sample" burst of very high significance with a thermally dominated spectrum. The main GRB was also well fit with strongly thermal components and overall high-degree of spectral similarity. These facts together may point towards a common origin, i.e., a post-merger model with a choking jet or similar (see Section 6.6).

5.6.3. GRB 180511437

The precursor in 180703B described above is not, however, the longest duration precursor; that title goes to that seen prior to GRB 180511437 with a duration of ~2.8 s [27].

Given that the T_{90} duration of this event has been debated in the literature, with some stipulating a long burst (see Section 5.2), it is difficult to place constraints on the progenitor. However, given the long delay ($\sim$12 s) and the lack of any obvious spectral similarity, a long period of magnetospheric interaction with especially tangled fields seems difficult to accommodate [376]. Resonances with a particularly long window are theoretical possible for some EOS; see Section 6.3.2.

5.6.4. GRB 191221A
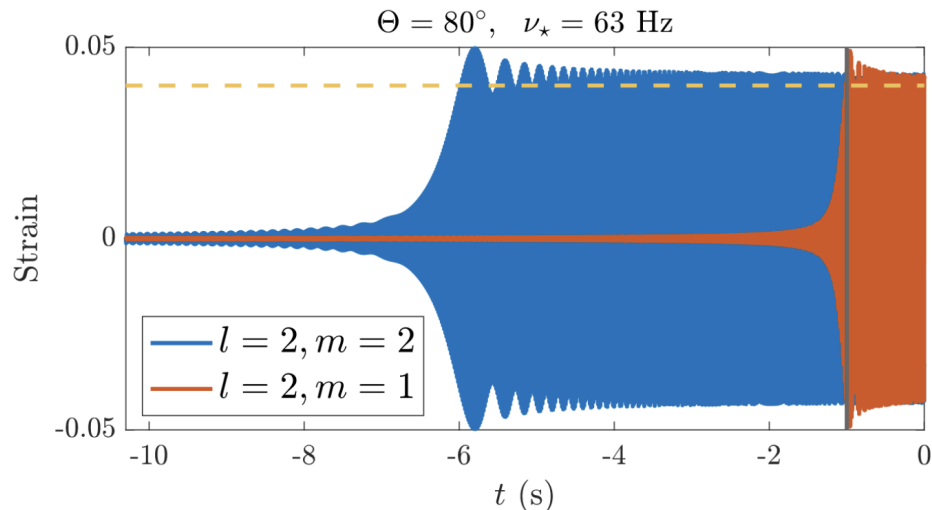
The precursor from 191221A is currently the record holder for earliest precursor relative to main event, with a staggering $\sim$20 s waiting time (though cf. Section Excluded Events). No constraints on the spectrum were placed [27]. This event was coincident with LVK's O3b run, though no GWs were detected [354], pointing to a non-negligible source redshift. The distinct lack of any X-ray afterglow is also problematic with respect to a stable neutron star remnant scenario, which would probably be favoured in order to ascribe the long delay to a jet formation timescale [18,377]. Premerger models in this direction, assuming a $<$10 s combined jet production and breakout timescale (see Section 6.1), are practically limited to low eigenfrequency resonances such as g-modes or ocean modes (Section 6.4) unless strong magnetic fields, thermal gradients, or rotation skew the eigenfrequency towards lower values (see Section 4.3). A systematic analysis of this event would be worthwhile to carry out because of the above considerations.

5.6.5. GRB 090510

GRB 090510 is special for two reasons: one being that, aside from the unclear case of 081024A, it is the only known merger-driven GRB that showed a *double precursor*.

The two precursors from this event were separated by $\sim$12 s [352], with the second precursor taking place $\sim$0.5 s prior to the main event. Several possibilities present themselves, involving (i) two premerger precursors, (ii) two post-merger precursors, or (iii) one of each. The parameter space is large. The first precursor was notably softer ($\sim$ 30 keV peak) than the second ($\sim$300 keV peak), which disfavours the operation of strong *external* magnetic fields at early stages. A possibility put forward by [48] involves rotation and stellar misalignment. As shown in Figure 15, a significant misalignment angle and rapid rotation (though the latter is not strictly necessary, as even spins of $\lesssim$ 10 Hz are sufficient) can instigate two episodes of crustal failure with $m = 2$ and $m = 1$ modes (see Section 4.3). Although the delay seen in this figure does not exactly correspond to that seen in 090510, it demonstrates the possibility. Regarding the 090510 double event specifically, parameter-space constraints are given in [48].

The second remarkable feature of GRB 090510 is that of a rather prominent X-ray afterglow as discussed by Suvorov and Kokkotas [118], Rowlinson et al. [361], and others. This afterglow exhibited the 'internal plateau' feature thought to be characteristic of a neutron star pumping spin-down energy into the forward shock. Importantly, the system showed a steady decline in flux rather than a sharp cutoff, which is often interpreted as the collapse time of the metastable star (see [8,378]). If indeed a stable neutron star was formed, it is more plausible that the jet formation timescale was comparatively long, and hence that only one precursor was premerger, with the second being attributable to a choking jet, possibly because neutron stars have a harder time forming jets with high Lorentz factors [379]. Still, several scenarios are viable.

Figure 15. A double resonance of $m = 2$ and $m = 1$ kink modes in a highly misaligned and rapidly rotating neutron star. The strain (σ) can exceed ~ 0.04—a realistic elastic maximum [170,172,173]—and thus, theoretically, trigger two episodes of failure separated by a number of seconds. The stratification rises to $\delta \approx 0.021$ for the later episode, due to intervening tidal heating (cf. Section 4.5), having started from an initial (cold) value of $\delta \approx 0.006$. The binary is symmetric with stars of mass $1.23 M_\odot$ and the APR4 EOS. From Kuan et al. [48].

5.6.6. GRB 230307A

GRB 230307A is an extremely bright, *long* GRB. The recorded gamma-ray fluence is $\gtrsim 3 \times 10^{-3}$ erg cm^{-2} in the 10–1000 keV band [33], second only to GRB 221009A. Despite its long duration, it is likely associated with a kilonova and heavy element production [9], thus resembling the case of GRB 211211A [33] of a merger-driven long GRB. Taking the best-fit distance of ≈ 291 Mpc implies an enormous luminosity $L_{\mathrm{prec}} \sim 3.6 \times 10^{50}$ erg s^{-1}. As discussed by Dichiara et al. [33], this event is a strong candidate for a magnetar with an external field of $\gtrsim 10^{15}$ G taking place in a merger. This is not only because of the spectrum and high luminosity but because of its long-short nature supporting a magnetar-in-a-merger origin if magnetic barriers are easier to set up (as for GRB 211211A). If the field were of this magnitude, accounting for magnetic shifting in mode eigenfrequencies would be essential as would electromotive torques towards the end of the binary evolution (see Section 4.4). Given the waiting time of only ≈ 0.4 s, however, many ignition scenarios are viable (especially post-merger ones).

5.7. Connections with Post-Merger Phenomena

Insofar as strong magnetic fields are necessary to explain premerger, precursor spectra (Section 5.4), the remnant environment and structure could be affected. It is fair to say that one of the open problems in GRB physics concerns whether or not magnetar remnants are capable of launching a relativistic jet that can drill through the polar baryon pollution (e.g., [23]). Most numerical simulations of mergers that leave a magnetar find that (i) a magnetic field of strength approaching equipartition ($\sim 10^{17}$ G) is needed to a launch a jet (if a jet can be launched at all), and (ii) the magnetic field that is generated is larger if the premerger 'seed' fields are larger (e.g., [380]). Point (ii) has been challenged by recent, high-resolution simulations [381], though it is naturally easier to accept strong remnant fields via flux conservation arguments if there is a magnetar in the merger.

The magnetic field strength of a remnant star would also influence its spin-down energy and GW luminosity. In principle, one could therefore anticipate a subpopulation of remnants with stronger fields if bright precursors are observed [34]. Even if irrelevant for precursors, the dynamo activity triggered by f- or other mode resonances just before merger could also amplify seed fields (see Section 6.5).

6. Precursor Flares: Theory

This section of the review is dedicated to theoretical models for precursor flares. The bulk relates to premerger mechanisms (though see Section 6.6), with special focus placed on the resonant failure picture, owing to the authors' familiarity. If some stellar oscillation mode comes into resonance with the orbital motion while the stars are inspiralling, significant amounts of tidal energy may be deposited into the mode(s) as described in Section 4.1.3. The resonant amplitude may thus reach the point that the crust yields due to the exerted stresses exceeding the elastic maximum (Section 3.2). Two of the more promising candidates in this direction are the *g*- and *i*-modes, which appear to lie in a sweet spot, in the sense that the expected mode frequencies match the orbital frequency at times corresponding to many precursor flashes and the overlap integrals are sufficiently large (see Section 6.4). The other main mechanism involves electrodynamic interactions between the binary components (Section 6.2) or shocks in a mass-loaded wake [336]; there could be subpopulations of precursors associated with different mechanisms.

6.1. Delay Timescales: Post-Merger Jets

If one is to reliably assign a mechanism to precursor flare ignition, it is important that the physics relating to jet formation and breakout are understood in the context of the waiting time observations described in Section 5.5.

For better or worse, there is considerable theoretical uncertainty surrounding the orbital/GW frequency at which precursors are launched. This is because the times that are recorded are relative to the main GRB event (see Table 3). However, this will not coincide exactly with the moment of coalescence, which is the relevant quantity as concerns GWs, because there will generically be a delay timescale, t_J, required in order for the jet to not only form but also break out (i.e., penetrate through the surrounding baryon pollution) and produce the observed EM radiation (see Figure 1). For example, assuming that GWs do indeed propagate at the speed of light, the landmark event GW170817 indicates that the SGRB took $\approx$1.7 s to launch post-merger. If this estimate were canonical, many of the events listed in Table 3 would occur *post-merger*. This is obviously problematic if one wishes to ascribe resonant modes to their excitation mechanism.

Fortunately—at least from a premerger perspective—there is reason to suspect that t_J may be considerably shorter than that seen in GRB 170817A in some instances, perhaps even down to a $\sim$ few ms. In this section, we closely follow and summarise the compilations of [377] and [18] in describing various jet formation mechanisms and t_J estimates. Where appropriate, some recent numerical simulations or theoretical results concerning remnants are instead quoted to update and/or adjust values presented in Table 1 of [377].

We decompose the delay time, t_J, of a GRB observation relative to merger into three independent terms:

$$t_J = \Delta t_{jet} + \Delta t_{bo} + \Delta t_{GRB}, \tag{53}$$

where Δt_{jet} represents how long it takes for the engine to collimate the jet; Δt_{bo} is then the extra time for the jet to *break out* from the ambient material ejected before and at merger (and also of the environment generally); with finally Δt_{GRB} being an extra propagation timescale associated with the jet to reach some appropriate *energy dissipation radius*, where the actual γ-rays are emitted. In general, there will also be a combined cosmological and local (i.e., due to remnant gravity) redshift factor $1 + z$ to account for (see also Section 4.2.2), but since this applies to GWs and merger also, it is unimportant for the relative timing issue.

Zhang [377] introduced a second decomposition for Δt_{jet}, depending on the mechanism responsible for launching. The mechanism is naturally dependent on the progenitors. We write

$$\Delta t_{jet} = \Delta t_{rem} + \Delta t_{acc,B} + \Delta t_{clean}, \tag{54}$$

where Δt_{rem} is a waiting time for the responsible remnant to form (typically zero, unless invoking the collapse of some metastable neutron star), $\Delta t_{acc,B}$ is a further add-on related to the time for either accretion or dynamo activity to actually prime the object for jet launching

[i.e., dynamical fall-back timescale (acc) or dynamo timescale for magnetic growth (B)], and lastly we have the time taken for the jet to clean the surroundings (which is connected to the degree of mass loading), $\Delta t_{\rm clean}$. This final quantity is probably the most uncertain, and depends on the Lorentz factor that is achieved, which can be dragged by pollutants surrounding the crash site. For a thermal (neutrino-anti-neutrino annihilation) fireball, one anticipates a short timescale possibly of the order of only $\sim$ ms. For a magnetically (Poynting-flux) dominated jet, on the other hand, not only will the Lorentz factor generally be smaller [19] but the jet might have to reach a turbulence/reconnection radius, which is thought to exceed that of the relevant photosphere by a factor ~ 100. The main expectations are summarised in Table 4.

Table 4. Expected delays associated with merger-driven GRBs and relative precursor timings, adapted and expanded from Zhang [377]. Abbreviations: NS = Neutron star; SM = Supramassive; HM = hypermassive. Remarks: (*) HMNS collapse time could theoretically be prolonged through thermal [382] or magnetic [8] support, extending the upper limit significantly. (**) Result quoted from analysis performed in [379] regarding breakout requirements [see also [383] and [19] for detailed discussions]. (†) Results anticipated from high-resolution dynamo simulations of [381], who found amplification on sub-ms timescales. (‡) From simulations of [384], who found that sufficiently low-mass BHNSs result in a HMNS that tends to launch a magnetically dominated jet. It was argued by [385] that for canonical neutron-star parameters, SGRB is limited to "low" energies of order $\sim 10^{48}$ erg/s because of the tidal disruption impact on the torus mass. (#) We assume a fireball-like mechanism for accretion scenarios involving a neutron star, or a Blandford–Znajek mechanism if involving a BH, and a Poynting-flux-dominated jet for dynamo (magnetic) scenarios when estimating $\Delta t_{\rm GRB}$. However, in principle, any of these mechanisms could have an upper limit of many $\sim$ s owing to theoretical uncertainties; see [377] and [18]. Black hole topology and modified-gravity terms could also skew these estimates, though such effects are ignored (see [386,387]).

System	Engine	Mechanism	$\Delta t_{\rm jet}$			$\Delta t_{\rm bo}$ (s)	$\Delta t_{\rm GRB}$ (s; #)	$t_{\rm J,min}$ (s)	$t_{\rm J,max}$ (s)
			$\Delta t_{\rm rem}$ (s)	$\Delta t_{\rm acc,B}$ (ms)	$\Delta t_{\rm clean}$ (s)				
BH-NS	BH	accretion	~ 0	~ 10	~ 0	$\gtrsim 10^{-2}; \lesssim 10^{-1}$	$<$ few	$\sim 10^{-2}$	~ 3
BH-NS	HMNS/BH	accretion	$\gtrsim 0.1; \lesssim 1$ (*)	~ 10	~ 0	$\gtrsim 0.1; \lesssim 1$	$\lesssim$ few (‡)	$\lesssim 1$	>5 (*)
BH-NS	HMNS/BH	magnetic	~ 0	< 1 (†)	<1	$\gtrsim 10^{-2}; \lesssim 1$	$\lesssim$ few (‡)	$\lesssim 1$	~ 5
NS-NS	BH	accretion	~ 0	~ 10	~ 0	$\gtrsim 10^{-2}; \lesssim 10^{-1}$	$<$ few	$\sim 10^{-2}$	~ 3
NS-NS	HMNS/BH	accretion	$\gtrsim 0.1; \lesssim 1$ (*)	~ 10	~ 0	$\gtrsim 0.1; \lesssim 1$	$\lesssim$ few	$\gtrsim 10^{-1}$	>5 (*)
NS-NS	HMNS/BH	magnetic	~ 0	< 1 (†)	$\lesssim 1$	$\gtrsim 10^{-2}; \lesssim 1$	$\sim$ few	$\gtrsim 10^{-2}$	> 3
NS-NS	SMNS/NS	accretion	~ 0	~ 10	$\lesssim 0.1$	$\gtrsim 10^{-2}; \lesssim 10^{-1}$	$\lesssim$ few	$\gtrsim 10^{-2}$	$\gtrsim 3$
NS-NS	SMNS/NS	magnetic	~ 0	< 1 (†)	$\lesssim 0.2$ (**)	$\lesssim 0.2$ (**)	$\sim$ few	$\lesssim 1$	> 3

We close this section by noting that multimessenger events may accompany a collapse event for some of the remnant types listed in Table 4. Most notably, fast radio bursts (FRBs) have been predicted to be produced following the collapse of a neutron star (see [6,8]). Once an event horizon forms and cloaks the star, the external field lines are no longer anchored and so snap, inciting relativistic, magnetic shocks that accelerate electrons to high Lorentz factors, ultimately producing radiation in the $\gtrsim$ GHz band. A coincident detection of a sharp drop in X-ray flux and an FRB would be a "smoking gun" for a post-merger, neutron-star collapse; in such a case, at least $\Delta t_{\rm rem}$ could be tightly constrained. See [388] for recent (unsuccessful) search efforts for coincident FRBs and GRBs, and see [389] who found that FRB 20190425A is coincident with GW190425 at $\sim 2.8\sigma$. Sadly, no GRB was observed for this event.

6.2. Magnetospheric Interaction and Unipolar Inductor

Depending on the persistence (or late-time generation) of strong (crustal) magnetic fields over cosmological timescales, electrodynamic interactions occurring in the final seconds of inspiral could produce fireworks. The mechanisms responsible have been described in detail by [29] and others since. The production of gamma rays can proceed through essentially three different channels, depending on the relative magnetisation and

alignment angles of the two stars [32,327,329]. In cases with a black hole, comparable estimates can be found in [390].

The simplest, and arguably most probable if a luminous precursor is observed, scenario in the electrodynamic interaction context is that of the unipolar inductor introduced in Section 4.4. The reason for this is that it is already difficult to explain one magnetar in a merger let alone two, and without strong fields to mediate the interaction, the precursor is likely to fizzle out long before it reaches Earth. The other two cases instead apply when the object's have comparable magnetic dipole moments, either aligned or anti-aligned (though in reality of course there will be some angle Θ_μ). In the aligned case, the field lines will compress at the interaction radius given by $r_i \approx a/(1 + q_\mu^{1/3})$ with the dipole ratio $q_\mu = \mu_{B,d}/\mu_{A,d}$ [32]. In the opposite case, we have instead direct reconnection occurring in the interaction zone, which leads to explosive event(s) followed by the establishment of a quasi-stable circuit similar to a unipolar inductor (e.g., [30,330]).

It was argued in [327] that the maximum energy that can be relieved relates to $\dot{E}_{\text{EM}}$ from Equation (47). This is controlled by the effective resistance between the two stars through the effective twist parameter ζ_ϕ, viz.

$$
\begin{aligned}
\dot{E}_{\text{EM}} &\approx 6.0 \times 10^{43} \zeta_\phi \sqrt{\frac{M(1+q)}{1.4 M_\odot}} \left(\frac{B}{10^{12}\,\text{G}}\right)^2 \\
&\times \left(\frac{a}{30\,\text{km}}\right)^{-13/2} \left(\frac{R}{13\,\text{km}}\right)^8 \text{erg s}^{-1},
\end{aligned}
\tag{55}
$$

where B here is to be understood as the largest equatorial strength of either star, and we assume equal stellar radii. The above is difficult to reconcile with precursor luminosities unless $a \sim 3R$ and $\zeta_\phi \gg 1$, though $\dot{E}_{\text{EM}}$ can be slightly larger than estimates provided by [32] if ζ_ϕ is kept free.

The estimate (55) is in rough agreement with that found from ab initio numerical simulations for large twists. Most and Philippov [391] found, via special-relativistic simulations, a maximum dissipation of (Equation (6) therein)

$$
\dot{E}_{\text{MP20}} \approx 4.6 \times 10^{44} \left(\frac{B_{\text{int}}}{10^{12}\,\text{G}}\right)^2 \left(\frac{R}{13\,\text{km}}\right)^3,
\tag{56}
$$

applying just $\sim$ ms before merger for equal mass objects (see also [330]). Note in particular that the relevant B value here is the local value at the interaction radius not that at the stellar surface (though these are approximately equal at merger by definition). Interestingly, the luminosity scaling was found by [391] to be $\propto a^{-7/2}$, which is shallower than that of (55). Either way, we can match (56) with (55) at merger if $\zeta_\phi \lesssim 10$, consistent with the anti-aligned simulations by [30,330]. Some works in the literature [392,393] studied neutron star plus black hole binaries, finding roughly similar dissipation rates, though with the interesting result that the flares present in their simulations were up to $\sim 10^2$ times *brighter* than the (relativistic) orbital emission.

An important aspect of the interaction model is that emissions should be generated almost instantaneously. That is, particle production occurs immediately after reconnection, and thus the precursor timing should correspond directly to the ignition moment without an additional lag beyond those detailed in Section 6.1. On the other hand, the *duration* of a precursor born from magnetospheric interaction is likely limited to $\sim$10 ms based on the relationship between the Poynting flux and chirp length, where the separations are low [376]. This is somewhat shorter than *all* event durations listed in Table 3, though allowing for the factor of an extension of a few $\sim$ would bring many low-waiting-time precursors into view (e.g., 150922A, 100223110 , 100702A, ...). Still, Metzger and Zivancev [394] argued the detection horizon is limited to $\sim$10 Mpc for $B \approx 10^{14}$ G unless the twist is large, $\zeta_\phi \gg 1$.

Finally, aside from reconnection being generally able to spark a plethora of progenitors (see also Section 7), strong magnetic fields in the emission environment could effect

photon propagation directly. For example, quantum–mechanical photon splitting could acquire a non-negligible cross-section [395,396], thereby impacting the polarisation states and/or Faraday rotation of electromagnetic waves. Such effects, manifesting as vacuum birefringence, have been observed in emissions from the isolated neutron stars RX J1856.5-3754 [397] and 4U 0142+61 [398] with characteristic field strengths of a few by 10^{13} G [399] and $\sim 10^{14}$ G [39], respectively. As noted by [16], the next-generation gamma-ray polarimeter POLAR-2 may be able to measure such effects directly and constrain the plasma environment [400].

6.3. Resonant Failure: Luminosity and Timescales

The resonant failure picture that has been alluded to throughout this review is covered here and in Section 6.4. The model was initially put forward by [288], though it has since been covered by many authors in different contexts. In a nutshell: a large amount of tidal energy can be rapidly siphoned into modes from the orbit when a resonance is hit depending on the respective overlap integral; see Section 4.1.3. For some modes, the resonant amplitude grows large enough to overstrain the crust (see Section 3.1), releasing magnetoelastic energy that can theoretically fuel a gamma-ray flash. The way in this energy propagates is likely complicated depending on the local field strength, though the recent GR force-free electrodynamic simulations carried out by [401] tracked Alfvén waves propagating out to the orbital light cylinder with crossing time $t_{\text{cross}}^2 \approx a^3/G(M_A + M_B)$, where flares were formed self-consistently. For $a \approx 100$ km the light-crossing time is of the order of ms (see also Section 6.3.3). Although the mechanism responsible for the overstraining involves resonant pulsations rather than the gradual evolution of the magnetic field itself, the electromagnetic extraction of energy is totally analogous to that put forward for magnetar flares [37].

Based on relationship (6) for some mode, one can investigate whether any given mode candidate can be responsible for crustal failure. The mode eigenfrequency relates to the ignition time and GW frequency, which when correcting for jet formation and other factors (Section 6.1) can be matched to the precursor waiting time. Details of specific mode families are covered in Section 6.4, while below we go into more general aspects relating to luminosity and timescales.

6.3.1. Energetics

The maximum magnetically extractable luminosity from the crust of a neutron star is given by a Poynting integral, which for a dipole can be estimated through [288,367]

$$L_{\text{max}} \sim 10^{47} \left(\frac{v}{c}\right) \left(\frac{B_{\text{crust}}}{10^{13}\,\text{G}}\right)^2 \left(\frac{R}{10\,\text{km}}\right)^2 \text{erg s}^{-1}, \tag{57}$$

where v is the speed of the mode perturbation. While this value is considerably larger than (47), essentially because we have integrated over the whole *surface* rather than just in some small volume within a possibly distant interaction zone, it still requires relatively large fields to explain bright precursors. Such tensions can be alleviated somewhat by beaming (expected if some zone on the surface fails rather than the entire crust) and by noting that there is additional energy available beyond just that of the magnetic field.

More generally though, the maximum amount of energy during some window that can be liberated within a failed zone reads (e.g., [159]),

$$\int dt\, E_{\text{quake}} \leq \int_{t_{\text{offset}}}^{t_{\text{onset}}} dt \int_{V_{\text{crack}}(t)} d^3x\, u_{\text{tot}}, \tag{58}$$

where the total energy density u_{tot} accounts for all types of energy stored in the region. The above is obtained by integrating the energy stored in the failed zone over a resonance

duration $t_{\text{onset}} \leq t \leq t_{\text{offset}}$ (see Section 6.3.2). From a von Mises perspective, the volume V can be defined through

$$V_{\text{crack}}(t) = \{p \mid \sigma(p) \geq \sigma_{\max}, \ p \text{ within the crust}\}, \tag{59}$$

which is the collection of points such that the elastic maximum is exceeded at any given t.

The total density u_{tot} includes a (i) magnetic contribution [which is effectively just a rescaled version of (57)], the (ii) kinetic energy density of QNMs u_{kin}, (iii) rotational energy density u_{rot}, and finally the (iv) tidal energy density u_{tid}. The three latter contributions are respectively given by

$$u_{\text{kin}} = \frac{1}{2}(\dot{\xi} \cdot \dot{\xi})\rho \tag{60}$$
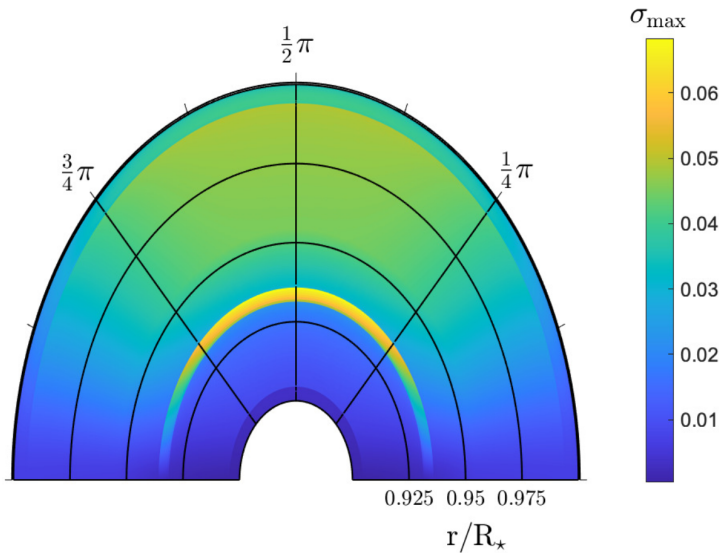
$$u_{\text{rot}} = \frac{1}{2}\Omega^2 r^2 \sin^2\theta\rho, \tag{61}$$

and

$$u_{\text{tid}} = U\delta\rho, \tag{62}$$

for tidal field U from Equation (13). An elastic term may be added also.

Under the approximations that (i) the energy released during a resonance timescale is just the integral of the energy density at the onset of resonance over the cracking area at the offset of resonance, and (ii) u_{rot} is only associated with uniform rotation and frame-dragging is negligible (cf. Section 4.2.2), these energies were calculated by [369] for some g-mode resonances (see Section 6.4.2). The main results are listed in Table 2 therein: for magnetar-level fields strengths, energy outputs can exceed $\sim 10^{46}$ erg each second. (How long such an event may last is covered in Section 6.3.2.) This would be sufficient to power most precursors, noting in particular that only some small fraction of the crust actually fails (rather than global events) in those simulations; see Figure 16 for one such g_2-strain pattern. If indeed the precursor were attributable to a g_2-mode, the isotropic luminosities quoted in Section 5.4 would not be appropriate, and in fact the energetics could easily be accommodated through expression (58).

Figure 16. Crustal strain pattern, σ (Equation (6)), in the northern hemisphere as induced by a g_2-mode for an *unmagnetised star* with the SLy EOS in an equal mass binary with $M = 1.27\,M_\odot$ and a constant stratification index $\delta = 0.005$. For $\sigma_{\max} \lesssim 0.05$ (see Table 1), a complicated failure geometry will emerge. From Kuan et al. [369].

Aside from beaming considerations, for slow stars, the main contributions are from the magnetic field so that (57) remains the leading-order piece. However, a $\sim$20% or

more leeway could be afforded if the resonances are triggered particularly close to merger, relaxing (some) difficulties associated with magnetic field strengths (see Section 2.3).

6.3.2. Resonance Window Duration

For a given mode with (inertial-frame) eigenfrequency $\omega_{\alpha,i}$, resonance will be triggered when Ω_{orb} falls in the interval $[\frac{1-\varepsilon}{2}\omega_{\alpha,i}, \frac{1+\varepsilon}{2}\omega_{\alpha,i}]$ [285], where the real part of the eigenfrequency is implied. This frequency interval yields a total duration of

$$t_{\mathrm{prec}} = \frac{\varepsilon \omega_{\alpha,i}}{\dot{\Omega}_{\mathrm{orb}}} \approx \frac{2\varepsilon \Omega_{\mathrm{orb}}}{\dot{\Omega}_{\mathrm{orb}}}, \tag{63}$$

which can be compared directly to observational durations from Table 3 assuming low redshift [cf. Equation (1) in [377] and Section 4.2.2]. The (dimensionless) detuning parameter ε can be calculated self-consistently with numerical simulations or the analytic approximation provided by Equation (3.10) in [285]. It is generally expressible as

$$\varepsilon = \chi \sqrt{\frac{2\pi}{\Omega_{\mathrm{orb}}} \frac{|\dot{a}|}{a}}, \tag{64}$$

for some parameter $1 \lesssim \chi \lesssim$ few. Although a value up to $\chi \approx 10$ was found for some *g*-modes by [224], more realistic values in most cases are $\chi \sim \mathcal{O}(1)$. Either way, the numerical detuning parameter (64) can be somewhat larger than the analytic estimate made by Lai [285]. More generally, χ depends on the EOS, mode family in question, spin, and microphysical (e.g., stratification) assumptions essentially because modes in stars with a specific mass can have the same frequency but different tidal overlap by tuning the aforementioned physics.

To the leading order, combining (50) with the frequency sweeping rate estimated from the Keplerian formula,

$$\frac{\dot{\Omega}_{\mathrm{orb}}}{\Omega_{\mathrm{orb}}} = -\frac{3\dot{a}}{2a}, \tag{65}$$

we can estimate that at a separation of $a = 170$ km, corresponding roughly to a normal-fluid *g*-mode with $f_{\alpha,i} \approx 88$ Hz and ≈ 3 seconds before merger, we have $t_{\mathrm{prec}} \approx 0.3$ s for stellar parameters such that $\chi = 2$. Such durations are more in line with the observational data (Table 3) than the ~ 10 ms values anticipated from the magnetospheric interaction picture discussed in Section 6.2 [376].

6.3.3. Launching Timescale

One important aspect of the resonant failure picture is that the flare will not be immediately launched once resonance, which is the quantity deducible from GWs for instance, is met. This couples with the issues described in Section 6.1 for deducing precursor merger waiting times. In particular, as detailed by [33,48], there are three timescales to consider. The first of these is the time it takes for overstraining to occur once resonance has been triggered. For the von Mises criterion (7), this failure happens instantaneously once expression (6) reaches a significantly large value. In a more realistic stress–strain model (e.g., Zhurkov; see Section 3.2), there may be a short delay associated with this step; see [146].

The next timescale pertains to the delay for *failure* once an overstraining has been triggered from resonance. This was estimated by Tsang et al. [288] to be on the order of ~ 1 ms based on elastic-to-tidal energy ratios, though it is sensitive to both the overlap integral and mode frequency (see below Equation (10) therein). These authors used a breaking-strain value of $\sigma_{\mathrm{max}} \sim 0.1$; all else being equal but using the [170] value $\sigma_{\mathrm{max}} \sim 0.04$ would increase this timescale by a factor $\sim (0.1/0.04)^2 \approx 6$ (see Table 1). Higher eigenfrequencies or energies would reduce it.

The final timescale of relevance, t_{emit}, relates to how long it takes for emissions to be generated following the failure (see [36,37] regarding the magnetar flare context). Neill et al. [402] argued t_{emit} can be as long as ~ 0.1 s for $B \sim 10^{13}$ G—see Equation (12) therein—again assuming $\sigma_{\text{max}} \sim 0.1$ from Horowitz and Kadau [162]. The result scales like [48]

$$t_{\text{emit}} \sim \frac{E_{\text{elastic}}}{L_{\text{max}}} \approx 0.03 \left(\frac{\sigma_{\text{max}}}{0.04} \right)^2 \left(\frac{10^{47} \text{ erg/s}}{L_{\text{prec}}} \right) \text{ s.} \qquad (66)$$

For most precursors, t_{emit} will be of the order of tens of ms. In support of this, t_{emit} is suggested to be related to a light crossing time that is relatively short unless $a \gg 100$ km [401].

Altogether, there are thus *eight* timescales to keep track of when trying to directly compare a tidal resonance to a precursor timing observation, at least in the resonance picture for bright *nonthermal precursors*. These are the five detailed in Section 6.1 relating to jet generation and breakout, and the three described above (or only one in the case of magnetospheric interactions). This highlights the non-trivial nature of the problem, where future numerical simulations of jet break-out and radiation transport are likely to prove particularly powerful. In fact, for thermal or comparatively low luminosity precursors, an additional set of physical timescales become relevant relating to collisions of fireball shells. As described by Neill et al. [402], regions surrounding the emission site may be optically thick to pair production, and multiple-pair photon fireballs could be launched, which, upon collision, create shocks and synchrotron emissions together with inherent blackbody emissions with luminosities reaching $\sim 10^{48}$ erg/s. The collision times of these shells depend on the Lorentz factors set through the degree of mass loading, with theoretical ranges spanning a few orders of magnitude, suggesting a wide range of viable timescales.
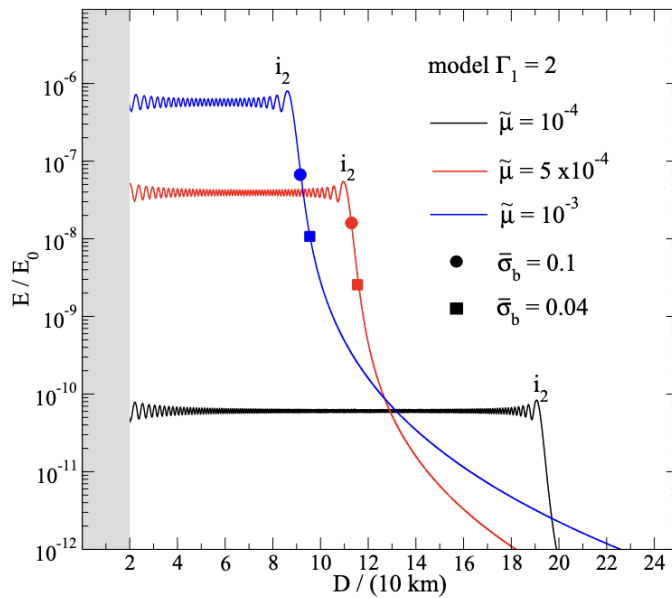
6.4. Resonant Failure: Some Important Families

This section details various QNM families which have been invoked to explain precursors in the literature: their physical origin, variation with EOS and microphysical parameters, eigenfrequencies, and overlap integrals.

6.4.1. i-Modes

As a neutron star cools, it is expected to undergo a number of localised phase transitions. These can relate to superfluidity and conductivity (Section 3.4), and the formation of a crust and ocean layers (Section 3.1). The presence of these solid–liquid discontinuities allows for a family of *interface* (*i*-) modes to exist. These were the first family that were considered viable for breaking and arguably remain the strongest candidate [33,288,367], at least for the crust–core (i_2) rather than crust–ocean (i_1) variety, though the latter can also induce non-trivial strain and crustal failure (see Section 6.4.3). This is because the overlap integrals tend to be large and *i*-mode eigenfrequencies are extremely sensitive to the transition density and stellar macrophysics, allowing for many events to be explained by this one mode in different stars [402]. Figure 17 shows predictions for the (appropriately normalised) energies deposited into *i*-modes as found by [225], who self-consistently included elastic terms into their (Newtonian) equations of motion.

Passamonti et al. [225] found *i*-mode overlaps to be two orders of magnitude weaker than those found by Tsang et al. [288]. Although still plausibly large enough to break the crust (at least for sufficiently large shear modulii; see Figure 17), this demonstrates that *i*-modes may not be generically optimal for any given neutron star configuration when incorporating elastic aspects. Another possible origin for this large discrepancy is rooted in the mixed use of Newtonian overlaps/perturbations but with a GR star. Although the use of such a hybrid scheme to solve for the stellar spectrum is common in the literature (and was used by [288] for instance), it leads to some non-orthogonality between modes and there can then be "leakage" of one mode to others when computing overlap integrals[8] [see Appendix A of [228] for a qualitative discussion].

Figure 17. Resonant amplitudes (expressed via energies in units of $E_0 = GM_A^2/R_A$) obtained for the crust–core interface modes i_2 for a polytropic star in Newtonian gravity (Γ_1 is our γ), where elastic terms in the crust are self-consistently included for a variety of shear modulii [$\tilde{\mu}$; normalised according to Equation (73) in [225]]. Circles (squares) denote distances associated with the moment of crustal failure, if applicable, for a stronger (weaker) breaking strain of 0.1 (0.04) under a von Mises criterion. From Passamonti et al. [225] with permission.

Overall, however, owing to the sensitivity of *i*-modes to crustal microphysics, these modes represent a powerful probe of stellar structure (e.g., for the possible existence of pasta phases; [148,402]). Neill et al. [403] demonstrated that constraints for the nuclear symmetry parameters—namely, the (isovector) symmetry energy parameters J, L, and K_{sym}—of a (nucleonic) EOS can be made when combining precursor measurements, assuming *i*-mode triggers, with GWs. The main results are described in Figure 3 therein, illustrating the complementary nature of such constraints with those obtained from terrestrial (e.g., PREX-II [404], where the neutron skin thickness of the heaviest lead isotopes were measured) and astrophysical experiments. For example, for a given *i*-mode frequency and ignoring the impacts of rotation or magnetic fields, shifts of $\sim$20 MeV in uncertainty ranges for L could be anticipated.
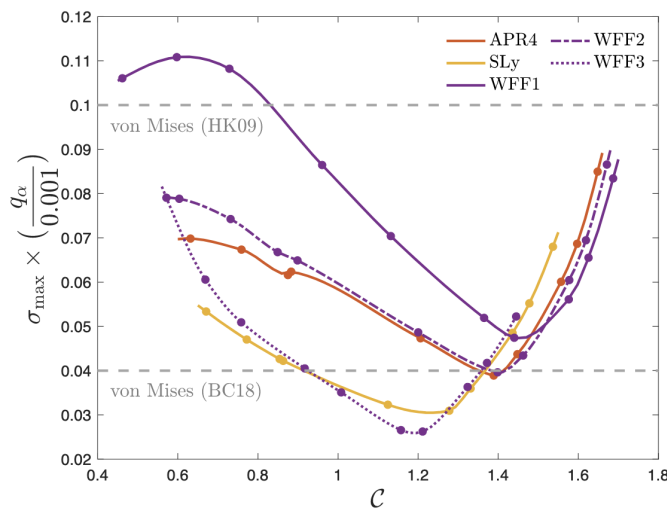
There are open issues in the modelling of *i*-modes, however, such as those that relate to consistent GR treatments, the choice of shear modulus profile, and the possibility of anisotropic nuclear clusters and pasta. Accurately incorporating these elements is a difficult task owing to both conceptual and numerical issues, and it is unclear how much anticipated constraints on parameter spaces may vary.

6.4.2. g-Modes
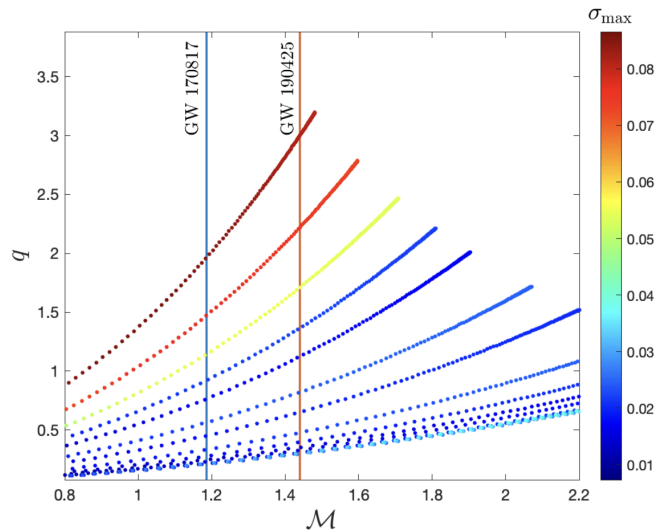
As described throughout, these modes are due to buoyancy resulting from thermal or composition gradients (including discontinuities; [405–407]) sourced intrinsically or through the accretion of matter from a companion, crustal movements, or magnetic interactions (e.g., [408]). For cold stars in a late-stage binary, the frequencies of (normal fluid) *g*-modes can range from tens to hundreds of Hz, indicating resonances occur 1–10 s prior to merger when spin is insignificant (see Section 4.3). Interestingly, maximum amplitudes and frequency tend to increase with stellar mass for the g_1-modes, while the amplitudes tend to *decrease* for g_2-modes; see Table 1 in [34]. On the other hand, *g*-modes in less compact stars have longer growth times, compensating for their weaker coupling to the tidal field to some extent. As such, the maximally induced *stress* exhibits a parabola-like shape, at least

when the stratification is held fixed as seen in Figure 18. The local minima of these curves have been referred to as "tidal neutrality" as described in Appendix A of [49].

In addition to the intrinsic mode properties, the binary mass ratio also influences the resonance timescale through the tidal potential (13), and hence the maximal stress also. Figure 19 demonstrates that a larger strain is generally manifest when the companion is heavier (i.e., the g_1-mode issues a greater σ) for a given chirp mass $\mathcal{M} = M_A q^{3/5} / (1+q)^{1/5}$ of the binary, which can be precisely estimated with GW analysis (e.g., [251]). This occurs because when $\mathcal{M}$ is fixed, a larger q implies a lower mass and pushes the system into the left half of the compactness range considered in Figure 18, noting the use of WFF1 (Section 2.1.1). For other EOSs, the trend may reverse.
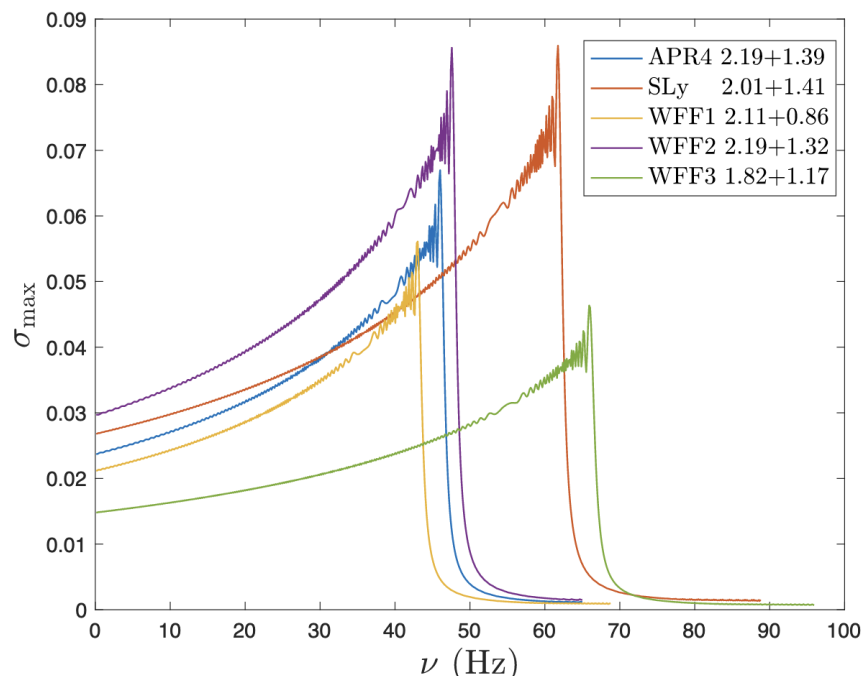
Figure 18. Dependence of the maximally induced stress (Equation 6) due to g_1- modes for various EOSs (same for both stars with $q = 1$) as functions of the stellar compactness $\mathcal{C} = M_{1.4}/R_{10\mathrm{km}}$. The grey dashed lines represent the von Mises criterion identified by [170] (lower) and [162] (upper). A fixed value of $\delta = 0.005$ is used. From Kuan et al. [369].

Figure 19. Sequences of maximal strain (redder shades indicating a greater value for σ) driven by g_1-mode resonances for the WFF1 EOS for various chirp masses $\mathcal{M}$ and mass ratios. The blue vertical line shows the chirp mass of the progenitor of GW 170817, while the red corresponds to GW 190425. From Kuan et al. [369].

As discussed in Section 4.3, spin reduces the frequency of retrograde modes. When the stellar angular momentum is in the opposite direction to that of the orbit, the oscillation

rate of tidally susceptible modes (whose phase pattern velocity matches the orbit) is slowed, pushing the resonance time earlier. Although perhaps counter-intuitive, [285] showed that the scaling of the saturation amplitude after resonance is $\propto \omega_\alpha^{-5/6}$ under the stationary phase approximation (i.e., when the orbital decay rate is much slower than the mode frequency): an earlier resonance thus generally renders a higher amplitude, leading to a general increase, with maximal strain as a function of spin as presented in Figure 20 for fixed overlap. In principle, this increase reaches a peak at the spin such that the mode will be likely smeared out by chemical reaction, leading to an abrupt zeroing of the strain. Note, however, that such a smearing was not modelled by [369]: the reason for the drop in σ in this case is because the mode frequency drops enough such that the resonance window falls outside of the computational domain at some minimum $\Omega_{\mathrm{Orb}}(t=0)$.

Figure 20. Similar to Figure 18 but as functions of the stellar spin for fixed compactness. Plot legends for the systems define the mutually abiding EOSs together with individual masses in units of $M_\odot$. Sharp drops after a certain spin for different modes result because the mode frequency drops lower than the initial tidal pushing frequency used in the numerical computation, and may be analogous to the spectral "washing out" described in Section 3.3 once the mode frequencies drop too low. From Kuan et al. [369].

Although g-modes reside mostly in the core, they are capable of exerting strain at the bottom of the crust for two reasons. (i) They penetrate into the crust when δ is sufficiently large; in fact, Refs. [225,296] demonstrated that the g_1-mode eigenfunction can resemble that of the i-mode though the frequencies differ (cf. [409]). (ii) Their tangential motion is not necessarily small, even when buoyancy is somewhat quenched by the shear modulus. Should some crustal activities be triggered by g-modes and lead to observables, information about the internal stratification, thermal properties, cooling, phase transitions (including gravitational ones; [410]), and heat transport in neutron stars could all be gleaned.

There are open problems in this direction related to the handling of the microphysics that more sophisticated models hope to treat in future. Even with respect to the models described above that do include crustal elasticity explicitly, compositional stratifications at the base of the crust may be driven by neutron drip from nuclear clusters, which is likely to occur at timescales *faster* than those of g-mode oscillations, thereby modifying the mode eigenfunctions there relative to models, where perturbed adiabatic indices were put in by hand. Other models described throughout that do use tabulated EOS data for

describing the crust and boundary layer composition (see Figure 5) but which do not include crustal elasticity may similarly overestimate the crustal strain. Efforts to include all such components for *g*-modes are in progress.

6.4.3. Ocean Modes

Ocean modes refer rather literally to waves (as for surface waves on Earth's oceans) that occur in the thin, penultimate layer of the star (before the atmosphere), which is typically a few meters to tens of meters thick [411,412]. Given the low density of the region, these modes are especially affected by the magnetic field, temperature gradients, gravitational forces, and, most importantly, composition. Ocean modes are important in the context of X-ray bursts, as the thermonuclear reactions that heat up the ocean layer can also instigate drifts that modulate the X-ray emission (see Table 4 and references in [340]); such drifting can be used to study ocean and atmosphere structures [413–415].

Ocean modes tend to have frequencies of $\sim$ tens of Hz at most, and thus could be excited at early times in a merger. Similar to the *g*-mode case, there is a competition between the excitation window (which is long for low frequencies) and overlap (which tends to be small at low frequencies). This was investigated by [416], who found largest overlaps for carbon atmospheres with frequencies ~ 16 Hz. These authors also found that energy deposits could reach $\lesssim 10^{47}$ erg over the inspiral duration, decreasing by a few orders of magnitude if elasticity or a crust with heavier nuclei (e.g., oxygen or iron) is considered. Atmospheres composed of lighter elements may be expected in a system with a history of accretion; "rapid" rotation may thus coincide with larger ocean impact (Section 2.2). Again like the *g*-mode case, there should also be a contest between mode frequencies and the local reaction rate, though the reaction rate in the ocean can be quite different from that in the crust or core. For heavier atmospheres with sub-Hz mode frequencies, space-based GW interferometers may be especially useful since such resonances could occur long before the LVK window and possibly coincide with multimessenger activity [416]. Whether such modes could ever instigate crustal failure is unclear, though emissions may still result from particular accelerations via tidal-wave motions [289].

Aside from the crust–core interface, there is also a crust–ocean interface that can be considered (the i_1 mode). These can potentially grow to large amplitudes; as noted by [289], while crustal failure may be difficult to achieve through an initial resonance as i_1 overlaps are not so large (see Figure 9 in [225]), crustal inhomogeneities may arise from such local failures (see also [156]). This may prime the crust for failures down the line, through either repeated resonances of the same mode, in an eccentric or dynamically evolving system, or higher-frequency (e.g., *g*-) modes.

6.4.4. f-Modes

The *f*-undamental fluid oscillation mode is a member of the acoustic (*p*-) family, in which the main restoring force is the hydrostatic pressure. This mode has no nodes, and thus couples very strongly to the tidal field which also has no nodes as noted by [417] and others. The linear eigenfrequencies of these modes typically range from 1 kHz to several kHz, depending on the mass, radius, and internal structure of the star. However, several studies have noted an insensitivity to the EOS [275,418], allowing for universal relations to be written down. Such aspects are powerful in the sense that measuring an *f*-mode frequency would give valuable insight onto the compactness of the system in an EOS-independent way. For a complete list of such relations, including the effects of rotation, we refer the reader to [316,419].

Although these modes are likely dominant in the tidal dephasing problem (see Section 4.1.3), they are probably not especially relevant for precursors (the topic of this section). This is because their high frequency means that resonances, and hence crustal failure, are unlikely to occur except in cases with rapid rotation [310], high eccentricity [343], or if the stellar compactness is particularly low (e.g., for EOS predicting large radii; see Figure 2). Still, if resonant, failure is practically guaranteed, as the overlap is of order
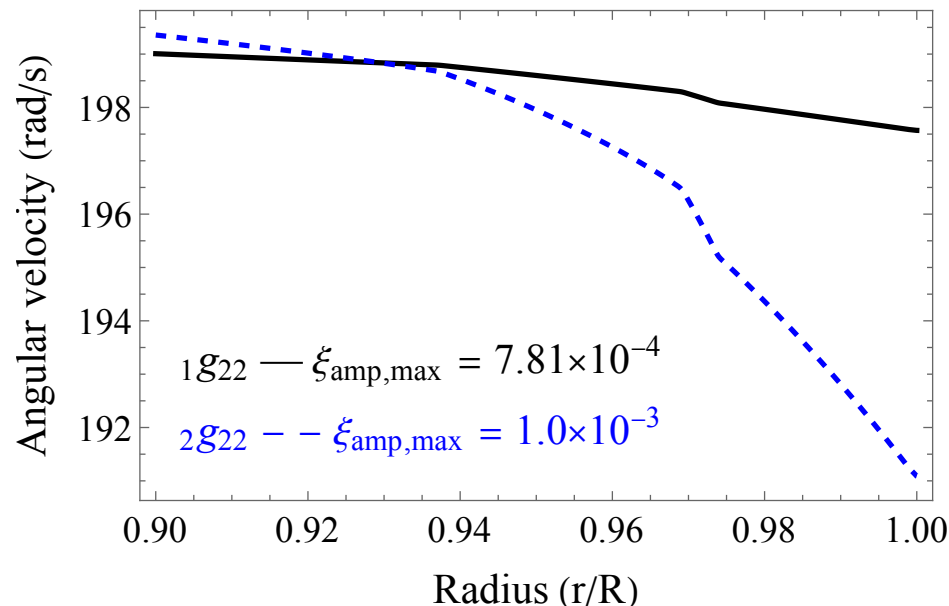
unity, and thus this mode could explain short-waiting-time events (like in GRBs 150922A, 100223110, ...).

6.4.5. r-Modes

Inertial (i.e., *r*-) modes are quasi-axial modes, degenerating in the static limit, with relatively weak coupling to the tidal field. However, in systems that are rotating very rapidly ($\nu \gg 100$ Hz), the hybrid character allows the modes to exert non-negligible strain on the crust [218,310], though it is expected that such systems are rare (cf. Section 2.2; [88]). They are generically unstable to rotational instabilities [318,420–422] because their co-rotating frame frequencies are less than $2\Omega_s$ [see Equation (24)], and in this way, they may be important in limiting the maximum rotation of neutron stars through radiation reaction [423]. They can be potentially excited in neutron star glitches [424], the predicted amplitudes of which may be detectable with LVK given $\gtrsim$ months of folding for galactic sources (e.g., PSR J0537-691; [425]). Mathematical considerations related to tidal and magnetic corrections to the inertial spectrum were considered in [310], and are similarly not expected to be important unless magnetars are present in the merger (cf. Sections 2.3 and 4.2). In principle, *r*-modes could also incite dynamo activity prior to merger if a large enough amplitude is reached ([426]; see also Section 6.5).

6.5. Late-Stage Dynamos?

Tidal resonances, aside from draining energy from the orbit, also add angular momentum to the stellar interior (Section Tidal Spinup). The resulting velocity pattern is tied to the mode eigenfunction and generally implies differentially rotating cavities, $\Omega = \Omega(t, \boldsymbol{x})$. One such example, computed self-consistently by [34], is shown in Figure 21 for two different *g*-mode resonances. The snapshots are taken at the moment of peak positive amplitude in the crust. Generally speaking, low-overtone *g*-modes have a monotonic radial profile in the crust, leading to either $\partial_r \Omega < 0$ or $\partial_r \Omega > 0$ everywhere there, depending on the mode phase.
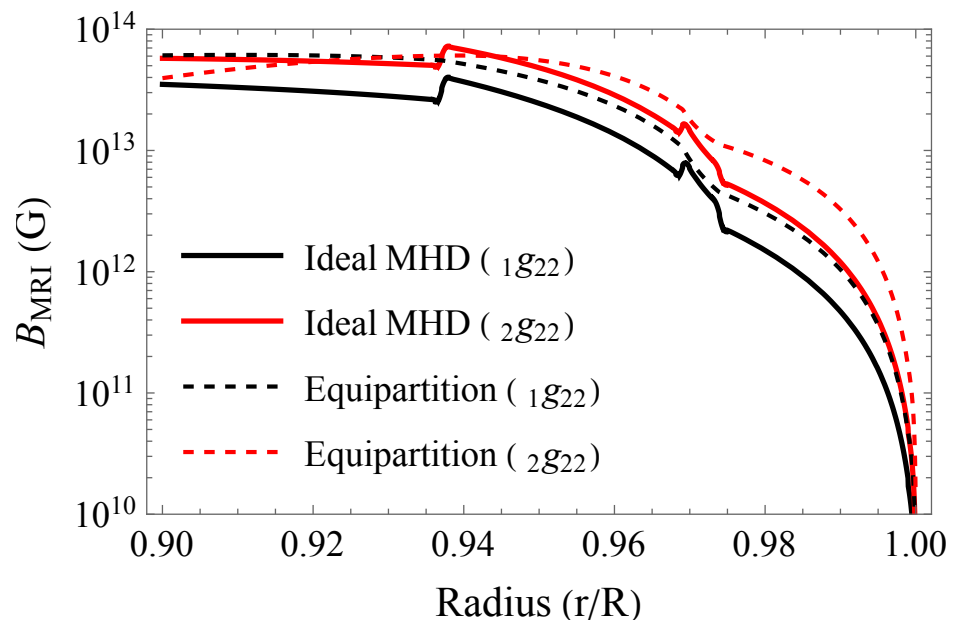
Figure 21. Crustal angular velocities at fixed spherical angles, $\Omega(r)$, for g_1 (black, solid) and g_2 (blue, dashed) modes, at a time slice corresponding to the maximum resonant amplitude. The star has an initial angular velocity of $\Omega_s = 200$ rad/s with $M = 1.6 M_\odot$, and $R = 11.26$ km with a hybrid APR4 + [62] (for the crust) EOS. From Suvorov et al. [34].

Differential rotation is typically a necessary (but not sufficient) condition for a dynamo, most notably, the magnetorotational instability (MRI): [427] and others since have shown

that if the radial angular velocity gradient is sufficiently negative in a cavity, $\partial_r \Omega \ll 0$, the magnetic tension can rocket to a large value in an effort to stabilise the system. The exact criterion depends on the microphysics of the cavity itself, such as the chemical diffusivity, stratification gradient, and electric resistivity. As explored by [34], the magnetic field could be amplified on ∼ms timescales in the final ∼s of inspiral via the MRI in a mature, recycled star. They found that saturation fields in the crust of a merger participant could exceed ∼ 10^{13} G for certain modes and EOS if the star is spinning sufficiently fast ($\nu \gtrsim 30$ Hz). The reason that some pre-existing rotation is necessary is because it influences the growth time of the unstable magnetic (Alfvén) modes, in general like $t_{MRI} \propto \Omega_s^{-1}$ [427,428]. This is important because the mode oscillation will flip the sign of $\Omega(x)$ every half-period, and thus if the mode growth is too slow (i.e., if Ω_s is too low), then less (or no) amplification is anticipated. The extent can be computed with a dephasing integral.

Fields of strength depicted in Figure 22 would allow for the magnetic energy budget to match the observed luminosities of precursors, possibly resolving the mystery of why precursors are rare: fast stars are needed. Suvorov et al. [34] estimated that the conditions necessary for the MRI are satisfied in ∼ 5% of merger events (see Appendix A therein). It may therefore be that magnetar-level fields do not persist into merger, but rather the field is generated. While appealing, some issues remain with this interpretation, the main one being that it is difficult to imagine a coherent field being produced; rather, one may expect a turbulent, highly tangled structure to emerge, as is more typical from MRI simulations (e.g., [381]). The process of extracting magnetoelastic energy is thus more complicated, and further work is needed to address the topological development of the field. A second issue is that estimates thus far have been carried out in (GR)MHD, but really elastic terms are necessary to adequately describe the crustal system. Whether it is possible for the MRI to activate in an *elastic cavity*, rather than fluid interior, is not obvious. Efforts in this direction are underway. Other dynamos would be worth investigating, like those with a chiral flavour [429] triggered by tide-related processes that force the system out of thermodynamic equilibrium prior to merger [186].


Figure 22. Dynamo amplifications from either a local MHD analysis (solid curves) or setting equipartition between magnetic and shear energies (dashed curves; upper limits) as triggered by either g_1- or g_2-modes in a star with $\Omega_{s,0} = 200$ rad/s. The same macro- and microparameters used in Figure 21 are used. From Suvorov et al. [34].

6.6. Post-Merger Models

If the main GRB episode is produced by (the standard mechanism involving) synchrotron radiation in an internal shock or magnetic dissipation zone, a (thermal) precursor may be expected either as the shock breaks out from the surrounding ejecta or as some (neutrino–anti-neutrino) fireball reaches the photosphere [16,32,430]. Alternatively, it may be that an incipient jet fails to break out (or "chokes"), which can produce some GRB-like emission prior to the main event, where a renewed jet successfully escapes. In the latter case, a range of spectra are plausible depending on the jet nature. A newborn magnetar may also launch a powerful wind independently from the jet, which may interact with the surroundings and produce X- and gamma-ray activity (e.g., [113]). Overall, this review is concerned with premerger phenomena, and thus we do not discuss these possibilities further. The interested reader is directed to [18,19,23] and the references therein.

7. Multimessenger Outlook

The previous three sections were devoted to understanding gravitational and gamma-ray emissions in premerger systems. These can be studied through tidal and magnetic interaction theory, with a careful of the stellar micro- and macrophysics. Here, by contrast, we turn briefly to other multimessenger elements, expected in the radio and X-ray bands, together with neutrino counterparts. We intentionally keep this section rather short: such elements have been described elsewhere (see, for instance [431]), and our main focus is on the gamma and GW aspects.

What can one learn, broadly speaking, from premerger multimessengers? A rough summary is provided below.

1. Love numbers. The effective parameter κ^T, the quadrupolar member of which is defined by (39), is directly visible in the gravitational waveform at a leading PN order (see Table 2). Since this quantity depends on the stellar masses and integrals taken over by the internal density, it is clear that EOS information can be gleaned. This is effectively illustrated in Figure 2, showing mass–radius contours from GW170817.
2. Asteroseismology. Dynamical tides also imprint themselves on the waveform. However, since these emerge at finite, non-zero frequencies, while the former appear already "at infinity", they are generally subleading. It has been estimated that only in $\sim 1\%$ of neutron-star mergers will one be able to cleanly isolate the impact of dynamical tides with current detectors [292]. However, owing to the discussion provided in Section 4.1.3, there are open questions in this direction which are worth revisiting. For example, the g-modes may be comparable contributors to the dephasing if the f-mode frequency is very high (cf. Figure 9). Strong magnetic fields may also be important, either through modulating the mode frequencies directly or instigating an electromotive spin-up (Section 4.4), which continuously shifts the spectra. Out-of-equilibrium effects could also distort the spectrum in a complicated, time-dependent way [186].
3. Gamma-ray precursors. Depending on the ignition mechanism, different kinds of information may be discernible. For premerger precursors, we argue the resonant failure picture can adequately explain all the observational characteristics (Section 6.3), though admittedly this is due to the huge range of QNM properties that neutron stars can exhibit. As resonances are obviously tied to the mode spectra, everything above applies here too but in the gamma-ray band. Similarly, since the activity of these modes *in the crust* is the relevant aspect here, microphysical inputs become critical. With the above three (Love number, dynamical tides, and precursors), one may thus learn about both macro- and microphysical elements of the stars taking part in a merger. This can be combined self-consistently with the properties of the post-merger remnant to deduce generative elements of GRBs (e.g., heavier stars will more likely promptly collapse, leading to faster jet break-out; see [377] and Table 4).
4. Radio flares. Radio activity can be incited premerger from a few different channels. For instance, there may be shock-powered radio emissions through interactions taking place in the accelerating, binary wind left in the wake of the inspiral [336,432]. These

are likely to be in the form of FRBs or "giant pulse" like phenomena in the $\sim$ GHz band. Another possibility discussed by [28] is that acceleration zones may form in regions of interwoven magnetic fields, which could produce coherent, millisecond bursts in radio frequencies that are theoretically observable out to $\sim$ Gpc distances. Such observations could reveal information about the magnetospheric plasma and radio activation mechanisms, which can be used to deduce information about the general pulsar engine and all that can be conveyed about the stellar structure (see [433]). There is also the possibility of post-merger radio activity associated with a neutron star collapse as described in Section 6.1. The Square Kilometer Array (SKA) will go a long way towards detection prospects.

5. X-ray flares. We have earlier described how the emission mechanism for GRB precursors resembles that of giant flares from magnetars in terms of energy extraction and propagation. Given that X-ray activity from magnetars is commonplace (and arguably a defining feature), the same applies for premerger stars with strong fields. X-ray emission mechanisms in a premerger system are described by [434], the key ingredient being the non-linear development of magnetospheric Alfvén waves (see also [401]). Such observations may reveal crucial information about the local magnetic field strength and radiation transport physics, from which information about neutron-star evolutionary pathways can be deduced. X-ray activity may also be related to magnetic instabilities arising by late-stage dynamo activity or magnetic reconfiguration, more generally (see Section 6.5 and also [158,435] for instance). The planned ECLAIRs telescope will help enable searches for X-rays out to cosmological distances.

6. Neutrinos. Neutrinos could be emitted from a premerger system through at least two distinct means. One involves tidal heating. As described in Section 4.5, rapid episodes of heating could lead to chemical imbalance and the production of neutrinos, which could be theoretically observed for a close merger. Such observations would provide important information on the microphysical heat capacity. The second mechanism is indirectly via the production of cosmic rays. As discussed by Coppin and van Eijndhoven [436], it is thought that GRBs could be sources of ultra-high-energy cosmic rays. In this case, the interaction of high-energy protons in relativistic wind wakes (as above) near the source could produce neutrinos carrying a non-negligible fraction of the proton energy. Ice-Cube has reported the detection of some *cosmic neutrinos* [437–439], while the sources are only identified in a few cases; next-generation neutrino observatories (like IceCube-Gen2; [440]) will synergise with other instruments to better constrain the sources (e.g., [441]). In addition, such observations could be used to place constraints on binary neutron star merger abundances and provide tests of the standard model [442]. For instance, neutrinos are thought to carry magnetic moments [443,444] through which they interact with the ambient magnetic field that depends on whether they are of a Dirac or Majorana nature [445]. Thus, the neutrino flux from a strongly magnetised environment, such as the engine of GRBs [446,447], may encode the neutrino's nature (e.g., [448]). An excellent review of future neutrino observatories, and instruments capable of follow-up, are described in Tables 1 and 2 of [449].

In addition to the above, there are the broadband kilonovae [356,357]. With the upcoming Roman Space Telescope, they may be detectable out to redshifts $z \sim 1$ [358], which is considerably further than the GWs from neutron star mergers. Even without GWs, more kilonova observations would be valuable to disentangle the types of GRBs that can be associated with mergers; see Section 5.2.

A Brief Look at Future Possibilities

One of the key ways in which multimessenger astrophysics will be propelled forward in the future comes from next-generation GW interferometers. Although there are a number of proposed technologies, some of the most notable are as follows. (i) The Einstein Telescope (ET; [450–453]). The sensitivity band of ET is similar to that of the LVK network, though notably deeply with considerable improvement in the $\lesssim 10$ Hz range. The reason is that

the gravitational gradient (i.e., "Newtonian"), seismic, and thermal noises are less of a problem for ET, as it will be built underground and include cryogenic technologies to reduce thermal vibrations [453]. This latter band is relevant to capture the onset of low-frequency oscillations and track the orbit for longer periods of time. (ii) Cosmic Explorer (CE; [454–456]). This detector is similar to ET in terms of sensitivity band, though it is planned to go even deeper. CE may detect *thousands* of neutron stars in merger [457], and thus lead to a true era where statistical methods can nail down the neutron-star EOS. (iii) The Laser Interferometer Space Antenna (LISA). LISA is a planned space-based detector that could capture the very early aspects of an inspiral while the orbit is at $\gtrsim$ mHz frequencies [458]. Wide binary elements could be useful for ocean resonances [289,416], low frequency *g*-modes (assuming these are not washed out by reaction rates; Section 3.3) and the testing of spacetime structure generally (see [459,460]).

With CE and ET, many of the high-amplitude QNMs of a merger remnant may be resolvable out to cosmological distances. Aside from providing tests of GR directly (see [290,461–463]), this could be connected with GRB observations to deduce the remnant nature and its impact on the jet structure; see [464], who reported the discovery of $\sim$ kHz modulations in the short GRBs 910711 and 931101B. Identifying oscillation frequencies in both the remnant and the premerger stars (via dynamical tides) would prove a powerful probe of fundamental physics. In a similar vein, GWs from a resonant failure itself may be detectable with a sufficiently sensitive telescope for a Galactic binary merger [465]. This would allow for the precursor-merger waiting time to be cleanly isolated, removing uncertainties relating to jet break-out (see Section 6.1).

Innovations on the electromagnetic side are no less promising. For instance, with the development of the SKA and next-generation X-ray observatories, the types of premerger precursors could increase significantly. Although we have limited our use of the word *precursor* to specifically mean the gamma-ray flashes occurring before the main event (see Table 3), it is hoped that such terminology will prove ambiguous in the future. Tables 1 and 2 of [449] provide a summary of next-generation telescopes that could coincidentally detect signals associated with neutrino bursts originating from a binary merger. One intriguing possibility comes from the planned POLAR-2 detector, which should be able to measure polarisation and similar effects related to the propagation of gamma rays (a survey of other next-generation gamma-ray facilities are described in Section 2 of [400]). This could be used to probe the local magnetic field strength in the region where the rays were produced. This would allow one to test, for instance, the extent to which non-thermality is tied to magnetars in mergers (see also Section 4.4).

8. Conclusions

This review is dedicated to the study of premerger phenomena in compact binaries involving at least one neutron star. Although there are a number of reviews of binary mergers on the market, we feel that none have attempted to put the theory of dynamical tides on a consistent footing together with the relevant GW and electromagnetic elements. Figure 1 provides an overall picture of that which we consider.

In compact binaries without pure black holes, tidal forces become large in the late stages of the inspiral. These strong tides distort the stars geometrically through the equilibrium tide and subsequently initiate large-amplitude fluid motions through dynamical tides (see Figure 6). Resonant pulsations can drain significant amounts of energy from the orbit, thereby allowing for avenues to test the highly coveted core EOS of neutron stars by examining *dephasing* predictions relative to cases where tides are "switched off" (see Figure 7). A review of tidal theory, with a particular emphasis on GW phenomena, is given in Section 4, building on the earlier two sections which introduced neutron-star macro- and microphysical elements. Although views on the detectability of dynamical tides in binaries vary in the literature, it is hoped that our review gives call for optimism, noting that there are open problems on both the theoretical side (e.g., modelling out-of-equilibrium elements related to tidal heating) and modelling side (e.g., accounting for time-dependent spins from tidal or electromotive torques), which, when resolved, may improve the outlook.

High-energy phenomena in late-stage inspirals are not limited to the GW sector, as the observation of early *precursors* establishes (see Section 5). Observational characteristics of these first-round gamma-ray flashes are highly varied in terms of their spectra, energetics, and waiting times (see Table 3). It is likely, therefore, that a single, theoretical model cannot account for all of them. The two more popular models considered thus far involve either electrodynamic interactions (Section 6.2) or, as above, resonant tides (Section 6.3). Even within these two classes, there are varied predictions. For example, which mode may be responsible for initiating crustal failure that leads to precursor emission? Several families have been proposed in the literature, as covered in Section 6.4. Aside from the gamma-ray flashes, a number of other multimessenger elements have been predicted, ranging from radio-band pulsations to neutrino floods. These are described in Section 7.

What type of constraints may the multimessenger channels described herein place on neutron-star magnetic fields, for instance? In no particular order, we have the following:

★ Magnetospheric interactions will accelerate the inspiral and lead to electromotive spin-up (quantified in Section 4.4), both of which may be visible in GWs either directly (dephasing) or indirectly (shifting mode frequencies as a function of time). Flares, radio pulsations, and/or FRBs may also be triggered by reconnection; such observations can place constraints on the large-scale, far-field dipole moments of old stars.

★ Strong internal fields ($B \gtrsim 10^{15}$ G) could, in principle, reveal themselves by shifting the stellar QNM frequencies or tidal Love numbers (Section Internal Fields). This could also be used to statistically constrain the presence or absence of superconducting states, as the superconductor tension force may also shift these properties even if B itself is partially expelled.

★ Near-surface fields could be constrained by bright, non-thermal precursors if the magnetic field dominates the energy transport process (e.g., the maximum luminosity is set by the near-surface field; see Section 6.3.1).

★ Remnant properties may be tied to the strength of the fields of the inspiralling constituents. Although very recent, high-resolution simulations suggest the magnetisation of the remnant may be set independently by dynamo activity [381], and disk material may still be highly magnetised [373], which could prolong subsequent GRB activity by setting up magnetic barriers that sporadically halt accretion. This channel could constrain internal fields and disc dynamics more generally.

★ Field longevity is a critical question in the precursor scenario. How is it possible that magnetars take place in mergers when the anticipated decay timescales are orders of magnitude lower than a typical inspiral time? If the answer is that it is impossible, we appear to be left with only two options, being either that (i) bright, non-thermal precursors must be *post-merger* phenomena (Section 6.6), or (ii) the field is generated by dynamo activity in the seconds leading up to coalescence (Section 6.5). Either of these would lead to constraints on jet formation and propagation together with the microphysics of the crust where the dynamo would operate. If such fields can persist into late times, this may call into question assumptions about field evolution generally (e.g., whether one can ignore meridional circulation when evolving the induction equation [333]).

We hope to leave the reader with the impression that premerger phenomena have the capacity to educate us on fundamental physics related to the low-temperature, high-baryon-density sector of quantum chromodynamics, GR, quantum electrodynamics, and more to a level that rivals that of post-merger phenomena.

Data Availability Statement: Compiled data presented in this review are freely available in the cited references. Additional data needed for reproducing figures can be made available on reasonable request to the corresponding author.

Conflicts of Interest: The authors declare no conflicts of interest. The funders had no role in the design of the study; in the collection, analyses, or interpretation of data; in the writing of the manuscript; or in the decision to publish the results.

Notes

1. For an up-to-date catalogue of neutron-star mass measurements, at least where there are no substantial systematics due to mass transfer or mass loss, see https://www3.mpifr-bonn.mpg.de/staff/pfreire/NS_masses.html, accessed on 27 November 2024. There are supposedly heavier "spiders", though these are highly dynamical and also rotating rapidly.
2. These and many other EOS can be obtained in a tabulated form at [46]: https://compose.obspm.fr/home/, accessed on 27 November 2024.
3. The BSk EOS table can be generated by the resources provided in https://www.ioffe.ru/astro/NSG/BSk/, accessed on 27 November 2024 or the CompOSE catalogue.
4. Subtle issues arise in GR, making this non-trivial. For example, even the notion of eccentricity is ambiguous [216]. An all-encompassing notion of "tide" is also hard to define via the Weyl tensor or other means; see Section I.C in [217].
5. This is no longer strictly true in GR (or when including complicated microphysics capable of independent, secular responses) as the metric variables, even in the Regge-Wheeler gauge for example, cannot be uniquely expressed in terms of this displacement (cf. w-modes, which exist even in the no-fluid limit where $\xi \to 0$). We remark also that the inclusion of an elastic region does not complicate the formal analysis here [225].
6. Two ways of generalising overlaps to GR have been proposed in [224] and [228]. The orthogonality between modes and the sum rule for tidal overlaps [229] are equally respected by both definitions, while only the former predicts a vanishing g-mode overlap in the zero stratification limit (at least for a simple, constant δ law; see Section 3.3). This issue is related to overlap "leakage" discussed in Section 6.4.1. Throughout, we adopt the definition of [224].
7. This raises a subtle issue: it could be that the GRB is missed (e.g., beamed away) but a precursor is launched in the direction of Earth. The precursor may therefore be mistaken for the actual GRB since such events can be spectrally similar in some instances (see also Section 5.4).
8. In GR, modes are not strictly orthogonal but the inner product between them is much smaller than the extent of this leakage; see also Note 6.

References

1. Lattimer, J.M. Neutron Stars and the Nuclear Matter Equation of State. *Annu. Rev. Nucl. Part. Sci.* **2021**, *71*, 433. [CrossRef]
2. Oertel, M.; Hempel, M.; Klähn, T.; Typel, S. Equations of state for supernovae and compact stars. *Rev. Mod. Phys.* **2017**, *89*, 015007. [CrossRef]
3. Özel, F.; Freire, P. Masses, Radii, and the Equation of State of Neutron Stars. *Annu. Rev. Astron. Astrophys.* **2016**, *54*, 401–440. [CrossRef]
4. Shibata, M.; Taniguchi, K.; Uryū, K. Merger of binary neutron stars of unequal mass in full general relativity. *Phys. Rev. D* **2003**, *68*, 084020. [CrossRef]
5. Shibata, M.; Uryū, K.ō. Simulation of merging binary neutron stars in full general relativity: Γ = 2 case. *Phys. Rev. D* **2000**, *61*, 064001. [CrossRef]
6. Falcke, H.; Rezzolla, L. Fast radio bursts: the last sign of supramassive neutron stars. *Astron. Astrophys.* **2014**, *562*, A137. [CrossRef]
7. Kaplan, J.D.; Ott, C.D.; O'Connor, E.P.; Kiuchi, K.; Roberts, L.; Duez, M. The Influence of Thermal Pressure on Equilibrium Models of Hypermassive Neutron Star Merger Remnants. The *Astrophys. J.* **2014**, *790*, 19. [CrossRef]
8. Suvorov, A.G.; Glampedakis, K. Magnetically supramassive neutron stars. *Phys. Rev. D* **2022**, *105*, L061302. [CrossRef]
9. Levan, A.J.; Gompertz, B.P.; Salafia, O.S.; Bulla, M.; Burns, E.; Hotokezaka, K.; Izzo, L.; Lamb, G.P.; Malesani, D.B.; Oates, S.R.; et al. Heavy-element production in a compact object merger observed by JWST. *Nature* **2024**, *626*, 737. [CrossRef]

10. Troja, E.; Fryer, C.L.; O'Connor, B.; Ryan, G.; Dichiara, S.; Kumar, A.; Ito, N.; Gupta, R.; Wollaeger, R.T.; Norris, J.P.; et al. A nearby long gamma-ray burst from a merger of compact objects. *Nature* **2022**, *612*, 228–231. [CrossRef] [PubMed]
11. Abbott, B.P. et al. [LIGO Scientific and Virgo Collaborations] GW170817: Observation of gravitational waves from a binary neutron star inspiral. *Phys. Rev. Lett.* **2017**, *119*, 161101. [PubMed]
12. Goldstein, A.; Veres, P.; Burns, E.; Briggs, M.S.; Hamburg, R.; Kocevski, D.; Wilson-Hodge, C.A.; Preece, R.D.; Poolakkil, S.; Roberts, O.J.; et al. An ordinary short gamma-ray burst with extraordinary implications: Fermi-GBM detection of GRB 170817A. *Astrophys. J. Lett.* **2017**, *848*, L14. [CrossRef]
13. Abbott, B.P. et al. [LIGO Scientific and Virgo Collaborations] Tests of general relativity with the binary black hole signals from the LIGO-Virgo catalog GWTC-1. *Phys. Rev. D* **2019**, *100*, 104036. [CrossRef]
14. Chatziioannou, K. Neutron-star tidal deformability and equation-of-state constraints. *Gen. Relativ. Gravit.* **2000**, *52*, 109. [CrossRef]
15. Dietrich, T.; Hinderer, T.; Samajdar, A. Interpreting binary neutron star mergers: Describing the binary neutron star dynamics, modelling gravitational waveforms, and analyzing detections. *Gen. Relativ. Gravit.* **2021**, *53*, 27. [CrossRef]
16. Wang, J.; Liu, L. Electromagnetic Precursors of Short Gamma-Ray Bursts as Counterparts of Gravitational Waves. *Galaxies* **2021**, *9*, 104. [CrossRef]
17. Baiotti, L.; Rezzolla, L. Binary neutron star mergers: A review of Einstein's richest laboratory. *Rep. Prog. Phys.* **2017**, *80*, 096901. [CrossRef]
18. Burns, E. Neutron star mergers and how to study them. *Living Rev. Relativ.* **2020**, *23*, 4.
19. Ciolfi, R. Short gamma-ray burst central engines. *Int. J. Mod. Phys. D* **2018**, *27*, 1842004. [CrossRef]
20. Faber, J.A.; Rasio, F.A. Binary neutron star mergers. *Living Rev. Relativ.* **2012**, *15*, 8. [CrossRef]
21. Kiuchi, K. General relativistic magnetohydodynamics simulations for binary neutron star mergers. *arXiv* **2024**, arXiv:2405.10081.
22. Radice, D.; Perego, A.; Hotokezaka, K.; Fromm, S.A.; Bernuzzi, S.; Roberts, L.F. Binary neutron star mergers: Mass ejection, electromagnetic counterparts, and nucleosynthesis. *Astrophys. J.* **2018**, *869*, 130. [CrossRef]
23. Sarin, N.; Lasky, P.D. The evolution of binary neutron star post-merger remnants: A review. *Gen. Relativ. Gravit.* **2021**, *53*, 59. [CrossRef]
24. Shibata, M.; Hotokezaka, K. Merger and mass ejection of neutron star binaries. *Annu. Rev. Nucl. Part. Sci.* **2019**, *69*, 41–64. [CrossRef]
25. Coppin, P.; de Vries, K.D.; van Eijndhoven, N. Identification of gamma-ray burst precursors in Fermi-GBM bursts. *Phys. Rev. D* **2020**, *102*, 103014. [CrossRef]
26. Deng, H.-Y.; Peng, Z.-Y.; Chen, J.-M.; Yin, Y.; Li, T. A Study of the Spectral properties of Gamma-Ray Bursts with the Precursors and Main bursts. *Astrophys. J.* **2024**, *970*, 67. [CrossRef]
27. Wang, J.-S.; Peng, Z.-K.; Zou, J.-H.; Zhang, B.-B.; Zhang, B. Stringent search for precursor emission in short grbs from fermi/gbm data and physical implications. *Astrophys. J. Lett.* **2020**, *902*, L42. [CrossRef]
28. Cooper, A.J.; Gupta, O.; Wadiasingh, Z.; Wijers, R.A.M.J.; Boersma, O.M.; Andreoni, I.; Rowlinson, A.; Gourdji, K. Pulsar revival in neutron star mergers: Multimessenger prospects for the discovery of pre-merger coherent radio emission. *Mon. Not. R. Astron. Soc.* **2023**, *519*, 3923–3946. [CrossRef]
29. Hansen, B.M.S.; Lyutikov, M. Radio and X-ray signatures of merging neutron stars. *Mon. Not. R. Astron. Soc.* **2001**, *322*, 695–701. [CrossRef]
30. Palenzuela, C.; Lehner, L.; Ponce, M.; Liebling, S.L.; Anderson, M.; Neilsen, D.; Motl, P. Electromagnetic and gravitational outputs from binary-neutron-star coalescence. *Phys. Rev. Lett.* **2013**, *111*, 061105. [CrossRef]
31. Wada, T.; Shibata, M.; Ioka, K. Analytic properties of the electromagnetic field of binary compact stars and electromagnetic precursors to gravitational waves. *Prog. Theor. Exp. Phys.* **2020**, *2020*, 103E01. [CrossRef]
32. Wang, J.-S.; Peng, F.-K.; Wu, K.; Dai, Z.-G.Pre-merger electromagnetic counterparts of binary compact stars. *Astrophys. J.* **2018**, *868*, 19. [CrossRef]
33. Dichiara, S.; Tsang, D.; Troja, E.; Neill, D.; Norris, J.P.; Yang, Y.H. A luminous precursor in the extremely bright GRB 230307A. *Astrophys. J. Lett.* **2023**, *954*, L29. [CrossRef]
34. Suvorov, A.G.; Kuan, H.-J.; Reboul-Salze, A.; Kokkotas, K.D. Magnetic amplification in premerger neutron stars through resonance-induced magnetorotational instabilities. *Phys. Rev. D* **2024**, *109*, 103023. [CrossRef]
35. Xiao, S.; Zhang, Y.Q.; Zhu, Z.P.; Xiong, S.L.; Gao, H.; Xu, D.; Zhang, S.N.; Peng, W.X.; Li, X.B.; Zhang, P.; et al. The peculiar precursor of a gamma-ray burst from a binary merger involving a magnetar. *Astrophys. J.* **2024**, *970*, 6. [CrossRef]
36. Thompson, C.; Duncan, R.C. Neutron star dynamos and the origins of pulsar magnetism. *Astrophys. J.* **1993**, *408*, 194–217. [CrossRef]
37. Thompson, C.; Duncan, R.C.The soft gamma repeaters as very strongly magnetized neutron stars-I. Radiative mechanism for outbursts. *Mon. Not. R. Astron. Soc.* **1995**, *275*, 255–300. [CrossRef]
38. Enoto, T.; Kisaka, S.; Shibata, S. Observational diversity of magnetized neutron stars. *Rep. Prog. Phys.* **2019**, *82*, 106901. [CrossRef]
39. Olausen, S.A.; Kaspi, V.M. The McGill magnetar catalog. *Astrophys. J. Suppl. Ser.* **2014**, *212*, 6. [CrossRef]
40. Hoyos, J.; Reisenegger, A.; Valdivia, J.A. Magnetic field evolution in neutron stars: One-dimensional multi-fluid model. *Astron. Astrophys.* **2008**, *487*, 789–803. [CrossRef]
41. Alford, M.G.; Harris, S.P. β equilibrium in neutron-star mergers. *Phys. Rev. C* **2018**, *98*, 065806. [CrossRef]

42. O'Boyle, M.F.; Markakis, C.; Stergioulas, N.; Read, J.S. Parametrized equation of state for neutron star matter with continuous sound speed. *Phys. Rev. D* **2020**, *102*, 083027. [CrossRef]
43. Alford, M.; Braby, M.; Paris, M.; Reddy, S. Hybrid stars that masquerade as neutron stars. *Astrophys. J.* **2005**, *629*, 969. [CrossRef]
44. Doroshenko, V.; Suleimanov, V.; Pühlhofer, G.; Santangelo, A. A strangely light neutron star within a supernova remnant. *Nat. Astron.* **2022**, *6*, 1444–1451. [CrossRef]
45. Ofengeim, D.D.; Shternin, P.S.; Piran, T. A three-parameter characterization of neutron stars' mass-radius relation and equation of state. *arXiv* **2024**, arXiv:2404.17647. [CrossRef]
46. Typel, S.; Oertel, M.; Klähn, T. CompOSE CompStar online supernova equations of state harmonising the concert of nuclear physics and astrophysics compose.obspm.fr. *Phys. Part. Nucl.* **2015**, *46*, 633–664. [CrossRef]
47. Krüger, C.J.; Ho, W.C.G.; Andersson, N. Seismology of adolescent neutron stars: Accounting for thermal effects and crust elasticity. *Phys. Rev. D* **2015**, *92*, 063009. [CrossRef]
48. Kuan, H.-J.; Suvorov, A.G.; Kokkotas, K.D. Measuring spin in coalescing binaries of neutron stars that show double precursors. *Astron. Astrophys.* **2023**, *676*, A59. [CrossRef]
49. Kuan, H.-J.; Krüger, C.J.; Suvorov, A.G.; Kokkotas, K.D. Constraining equation-of-state groups from g-mode asteroseismology. *Mon. Not. R. Astron. Soc.* **2022**, *513*, 4045–4056. [CrossRef]
50. Lattimer, J.M.; Prakash, M. Neutron star structure and the equation of state. *Astrophys. J.* **2001**, *550*, 426. [CrossRef]
51. Raithel, C.A.; Most, E.R. Characterizing the Breakdown of Quasi-universality in Postmerger Gravitational Waves from Binary Neutron Star Mergers. *Astrophys. J. Lett.* **2022**, *933*, L39. [CrossRef]
52. Sedrakian, A.; Li, J.J.; Weber, F. Heavy baryons in compact stars. *Prog. Part. Nucl. Phys.* **2023**, *131*, 104041. [CrossRef]
53. Greif, S.K.; Hebeler, K.; Lattimer, J.M.; Pethick, C.J.; Schwenk, A. Equation of state constraints from nuclear physics, neutron star masses, and future moment of inertia measurements. *Astrophys. J.* **2020**, *901*, 155. [CrossRef]
54. Wiringa, R.B.; Fiks, V.; Fabrocini, A. Equation of state for dense nucleon matter. *Phys. Rev. C* **1988**, *38*, 1010. [CrossRef] [PubMed]
55. Wiringa, R.B.; Stoks, V.G.J.; Schiavilla, R. Accurate nucleon-nucleon potential with charge-independence breaking. *Phys. Rev. C* **1995**, *51*, 38. [CrossRef]
56. Akmal, A.; Pandharipande, V.R.; Ravenhall, D.G. Equation of state of nucleon matter and neutron star structure. *Phys. Rev. C* **1998**, *58*, 1804. [CrossRef]
57. Anzuini, F.; Melatos, A.; Dehman, C.; Viganò, D.; Pons, J.A. Fast cooling and internal heating in hyperon stars. *Mon. Not. R. Astron. Soc.* **2022**, *509*, 2609–2623.
58. Schneider, A.S.; Constantinou, C.; Muccioli, B.; Prakash, M. Akmal-Pandharipande-Ravenhall equation of state for simulations of supernovae, neutron stars, and binary mergers. *Phys. Rev. C* **2019**, *100*, 025803. [CrossRef]
59. Burgio, G.F.; Schulze, H.J.; Vidaña, I.; Wei, J.B. Neutron stars and the nuclear equation of state. *Prog. Part. Nucl. Phys.* **2021**, *120*, 103879. [CrossRef]
60. Chabanat, E.; Bonche, P.; Haensel, P.; Meyer, J.; Schaeffer, R. A Skyrme parametrization from subnuclear to neutron star densities. *Nucl. Phys. A* **1997**, *627*, 710–746. [CrossRef]
61. Chabanat, E.; Bonche, P.; Haensel, P.; Meyer, J.; Schaeffer, R. A Skyrme parametrization from subnuclear to neutron star densities Part II. Nuclei far from stabilities. *Nucl. Phys. A* **1998**, *635*, 231–256. [CrossRef]
62. Douchin, F.; Haensel, P. A unified equation of state of dense matter and neutron star structure. *Astron. Astrophys.* **2001**, *380*, 151–167. [CrossRef]
63. Gulminelli, F.; Raduta, A.R. Unified treatment of subsaturation stellar matter at zero and finite temperature. *Phys. Rev. C* **2015**, *92*, 055803. [CrossRef]
64. Raduta, A.R.; Gulminelli, F. Nuclear statistical equilibrium equation of state for core collapse. *Nucl. Phys. A* **2019**, *983*, 252–275. [CrossRef]
65. Schneider, A.S.; Roberts, L.F.; Ott, C.D. A New Open-Source Nuclear Equation of State Framework based on the Liquid-Drop Model with Skyrme Interaction. *Phys. Rev. C* **2017**, *96*, 065802. [CrossRef]
66. Marino A.; Dehman C.; Kovlakas K.; Rea N.; Pons J.A.; Viganò, D. Constraints on the dense matter equation of state from young and cold isolated neutron stars. *Nat. Astron.* **2024**, *8*, 1020–1030. [CrossRef]
67. Goriely, S.; Chamel, N.; Pearson, J.M. Further explorations of Skyrme-Hartree-Fock-Bogoliubov mass formulas. XIII. The 2012 atomic mass evaluation and the symmetry coefficient. *Phys. Rev. C* **2013**, *88*, 024308. [CrossRef]
68. Pearson, J.M.; Chamel, N.; Goriely, S.; Ducoin, C. Inner crust of neutron stars with mass-fitted Skyrme functionals. *Phys. Rev. C* **2012**, *85*, 065803. [CrossRef]
69. Pearson, J.M.; Chamel, N.; Potekhin, A.Y.; Fantina, A.F.; Ducoin, C.; Dutta, A.K.; Goriely, S. Unified equations of state for cold non-accreting neutron stars with Brussels–Montreal functionals–I. Role of symmetry energy. *Mon. Not. R. Astron. Soc.* **2018**, *481*, 2994–3026. [CrossRef]
70. Pearson, J.M.; Goriely, S.; Chamel, N. Properties of the outer crust of neutron stars from Hartree-Fock-Bogoliubov mass models. *Phys. Rev. C* **2011**, *83*, 065810. [CrossRef]
71. Potekhin, A.Y.; Fantina, A.F.; Chamel, N.; Pearson, J.M.; Goriely, S. Analytical representations of unified equations of state for neutron-star matter. *Astron. Astrophys.* **2013**, *560*, A48. [CrossRef]
72. Dobaczewski, J.; Stoitsov, M.V.; Nazarewicz, W. Skyrme-HFB deformed nuclear mass table. *AIP Conf. Proc.* **2004**, *726*, 51–56. [CrossRef]

73. Fantina, A.F.; Zdunik, J.L.; Chamel, N.; Pearson, J.M.; Suleiman, L.; Goriely, S. Accreting neutron stars from the nuclear energy-density functional theory. II. Equation of state and global properties. *Astron. Astrophys.* **2022**, *665*, A74. [CrossRef]

74. Stockinger, G.; Janka, H.T.; Kresse, D.; Melson, T.; Ertl, T.; Gabler, M.; Gessner, A.; Wongwathanarat, A.; Tolstov, A.; Leung, S.C.; et al. Three-dimensional models of core-collapse supernovae from low-mass progenitors with implications for Crab. *Mon. Not. R. Astron. Soc.* **2020**, *496*, 2039–2084. [CrossRef]

75. Fields, C.E. The Three-dimensional Collapse of a Rapidly Rotating 16 $M_\odot$ Star. *Astrophys. J. Lett.* **2022**, *924*, L15. [CrossRef]

76. Varma, V.; Müller, B. 3D simulations of magnetoconvection in a rapidly rotating supernova progenitor. *Mon. Not. R. Astron. Soc.* **2023**, *526*, 5249–5262. [CrossRef]

77. Varma, V.; Müller, B.; Schneider, F.R.N. 3D simulations of strongly magnetized non-rotating supernovae: Explosion dynamics and remnant properties. *Mon. Not. R. Astron. Soc.* **2023**, *518*, 3622–3636. [CrossRef]

78. Patruno, A.; Haskell, B.; D'Angelo, C. Gravitational waves and the maximum spin frequency of neutron stars. *Astrophys. J.* **2012**, *746*, 9. [CrossRef]

79. Tauris, T.M.; Kramer, M.; Freire, P.C.C.; Wex, N.; Janka, H.T.; Langer, N.; Podsiadlowski, P.; Bozzo, E.; Chaty, S.; Kruckow, M.U.; et al. Formation of double neutron star systems. *Astrophys. J.* **2017**, *846*, 170. [CrossRef]

80. Andrews, J.J.; Mandel, I. Double neutron star populations and formation channels. *Astrophys. J. Lett.* **2019**, *880*, L8. [CrossRef]

81. van den Heuvel, E.P.J. *High-Mass X-Ray Binaries: Illuminating the Passage from Massive Binaries to Merging Compact Objects*; Oskinova, L.M., Bozzo, E., Bulik, T., Gies, D.R., Eds.; Cambridge University Press: Cambridge, UK, 2019; Volume 346, pp. 1–13.

82. Fonseca, E.; Stairs, I.H.; Thorsett, S.E. A comprehensive study of relativistic gravity using PSR B1534+ 12. *Astrophys. J.* **2014**, *787*, 82. [CrossRef]

83. Glampedakis, K.; Suvorov, A.G. Modelling spin-up episodes in accreting millisecond X-ray pulsars. *Mon. Not. R. Astron. Soc.* **2021**, *508*, 2399–2411. [CrossRef]

84. Melatos, A.; Payne, D.J.B. Gravitational radiation from an accreting millisecond pulsar with a magnetically confined mountain. *Astrophys. J.* **2005**, *623*, 1044. [CrossRef]

85. Suvorov, A.G.; Melatos, A.Testing modified gravity and no-hair relations for the Kerr-Newman metric through quasiperiodic oscillations of galactic microquasars. *Phys. Rev. D* **2016**, *93*, 024004. [CrossRef]

86. Suvorov, A.G.; Melatos, A. Relaxation by thermal conduction of a magnetically confined mountain on an accreting neutron star. *Mon. Not. R. Astron. Soc.* **2019**, *484*, 1079–1099. [CrossRef]

87. Vigelius, M.; Melatos, A. Resistive relaxation of a magnetically confined mountain on an accreting neutron star. *Mon. Not. R. Astron. Soc.* **2009**, *395*, 1985–1998. [CrossRef]

88. Zhu, X.; Thrane, E.; Osłowski, S.; Levin, Y.; Lasky, P.D. Inferring the population properties of binary neutron stars with gravitational-wave measurements of spin. *Phys. Rev. D* **2018**, *98*, 043002.

89. Dexheimer, V.; Franzon, B.; Gomes, R.O.; Farias, R.L.S.; Avancini, S.S.; Schramm, S. What is the magnetic field distribution for the equation of state of magnetized neutron stars? *Phys. Lett. B* **2017**, *773*, 487–491. [CrossRef]

90. Bilous, A.V.; Ransom, S.M.; Demorest, P. Unusually bright single pulses from the binary pulsar B1744–24A: A case of strong lensing? *Astrophys. J.* **2019**, *877*, 125. [CrossRef]

91. Riley, T.E. et al. [NICER Collaboration] A NICER view of the massive pulsar PSR J0740+ 6620 informed by radio timing and XMM-Newton spectroscopy. *Astrophys. J. Lett.* **2021**, *918*, L27. [CrossRef]

92. Kalapotharakos, C.; Wadiasingh, Z.; Harding, A.K.; Kazanas, D. The multipolar magnetic field of the millisecond pulsar PSR J0030+ 0451. *Astrophys. J.* **2021**, *907*, 63. [CrossRef]

93. Suvorov, A.G.; Melatos, A. Recycled pulsars with multipolar magnetospheres from accretion-induced magnetic burial. *Mon. Not. R. Astron. Soc.* **2020**, *499*, 3243–3254. [CrossRef]

94. Chen, K.; Ruderman, M. Pulsar death lines and death valley. *Astrophys. J.* **1993**, *402*, 264–270. [CrossRef]

95. Hibschman, J.A.; Arons, J. Pair multiplicities and pulsar death. *Astrophys. J.* **2001**, *554*, 624. [CrossRef]

96. Barnard, J.J.; Arons, J. Pair production and pulsar cutoff in magnetized neutron stars with nondipolar magnetic geometry. *Astrophys. J.* **1982**, *254*, 713–734. [CrossRef]

97. Beloborodov, A.M.; Thompson, C. Corona of magnetars. *Astrophys. J.* **2007**, *657*, 967. [CrossRef]

98. Zhang, B.; Gil, J.; Dyks, J. On the origins of part-time radio pulsars. *Mon. Not. R. Astron. Soc.* **2007**, *374*, 1103–1107. [CrossRef]

99. Suvorov, A.G.; Mastrano, A.; Geppert, U. Gravitational radiation from neutron stars deformed by crustal Hall drift. *Mon. Not. R. Astron. Soc.* **2016**, *459*, 3407–3418. [CrossRef]

100. Gourgouliatos, K.N.; De Grandis, D.; Igoshev, A. Magnetic field evolution in neutron star crusts: Beyond the hall effect. *Symmetry* **2022**, *14*, 130. [CrossRef]

101. Gusakov, M.E.; Kantor, E.M.; Ofengeim, D.D. Evolution of the magnetic field in neutron stars. *Phys. Rev. D* **2017**, *96*, 103012. [CrossRef]

102. Dehman, C.; Brandenburg, A. Reality of Inverse Cascading in Neutron Star Crusts. *arXiv* **2024**, arXiv:2408.08819. [CrossRef]

103. Barsukov, D.P.; Tsygan, A.I. The influence of nondipolar magnetic field and neutron star precession on braking indices of radiopulsars. *Mon. Not. R. Astron. Soc.* **2010**, *409*, 1077–1087. [CrossRef]

104. Melatos, A. Bumpy spin-down of anomalous x-ray pulsars: The link with magnetars. *Astrophys. J.* **1999**, *519*, L77. [CrossRef]

105. Johnston, S.; Galloway, D. Pulsar braking indices revisited. *Mon. Not. R. Astron. Soc.* **1999**, *306*, L50–L54. [CrossRef]

106. Bransgrove, A.; Levin, Y.; Beloborodov, A.M. Giant Hall Waves Launched by Superconducting Phase Transition in Pulsars. *arXiv* **2024**, arXiv:2408.10888.
107. Johnston, S.; Karastergiou, A. Pulsar braking and the *P–Ṗ* diagram. *Mon. Not. R. Astron. Soc.* **2017**, *467*, 3493–3499. [CrossRef]
108. Melatos, A.; Priymak, M. Gravitational radiation from magnetically funneled supernova fallback onto a magnetar. *Astrophys. J.* **2014**, *794*, 170. [CrossRef]
109. Bhattacharya, D.; van den Heuvel, E.P.J. Formation and evolution of binary and millisecond radio pulsars. *Phys. Rep.* **1991**, *203*, 1–124. [CrossRef]
110. Staubert, R.; Trümper, J.; Kendziorra, E.; Klochkov, D.; Postnov, K.; Kretschmar, P.; Pottschmidt, K.; Haberl, F.; Rothschild, R.E.; Santangelo, A.; et al. Cyclotron lines in highly magnetized neutron stars. *Astron. Astrophys.* **2019**, *622*, A61. [CrossRef]
111. Beloborodov, A.M. Untwisting magnetospheres of neutron stars. *Astrophys. J.* **2009**, *703*, 1044. [CrossRef]
112. Baym, G.; Pines, D. Neutron starquakes and pulsar speedup. *Ann. Phys.* **1971**, *66*, 816–835. [CrossRef]
113. Dall'Osso, S.; Stella, L. Millisecond Magnetars. In *Millisecond Pulsars*; Astrophysics and Space Science Library; Bhattacharyya, S., Papitto, A., Bhattacharya, D., Eds.; Springer: Cham, Switzerland, 2022; Volume 465, pp. 245–280.
114. Suvorov, A.G.; Kokkotas, K.D. Young magnetars with fracturing crusts as fast radio burst repeaters. *Mon. Not. R. Astron. Soc.* **2019**, *488*, 5887–5897. [CrossRef]
115. Makishima, K.; Enoto, T.; Hiraga, J.S.; Nakano, T.; Nakazawa, K.; Sakurai, S.; Sasano, M.; Murakami, H.Possible evidence for free precession of a strongly magnetized neutron star in the magnetar 4U 0142+ 61. *Phys. Rev. Lett.* **2014**, *112*, 171102. [CrossRef] [PubMed]
116. Makishima, K.; Tamba, T.; Aizawa, Y.; Odaka, H.; Yoneda, H.; Enoto, T.; Suzuki, H. Discovery of 40.5 ks hard X-ray pulse-phase modulations from SGR 1900+ 14. *Astrophys. J.* **2021**, *923*, 63. [CrossRef]
117. Mastrano, A.; Suvorov, A.G.; Melatos, A. Neutron star deformation due to poloidal–toroidal magnetic fields of arbitrary multipole order: A new analytic approach. *Mon. Not. R. Astron. Soc.* **2015**, *447*, 3475–3485. [CrossRef]
118. Suvorov, A.G.; Kokkotas, K.D. Evidence for magnetar precession in X-ray afterglows of gamma-ray bursts. *Astrophys. J. Lett.* **2020**, *892*, L34. [CrossRef]
119. Akgün, T.; Reisenegger, A.; Mastrano, A.; Marchant, P. Stability of magnetic fields in non-barotropic stars: An analytic treatment. *Mon. Not. R. Astron. Soc.* **2013**, *433*, 2445–2466. [CrossRef]
120. Herbrik, M.; Kokkotas, K.D. Stability analysis of magnetized neutron stars—A semi-analytic approach. *Mon. Not. R. Astron. Soc.* **2017**, *466*, 1330–1347. [CrossRef]
121. Tayler, R.J. The Adiabatic Stability of Stars Containing Magnetic Fields–I: T OROIDAL F IELDS. *Mon. Not. R. Astron. Soc.* **1973**, *161*, 365–380. [CrossRef]
122. Melatos, A. Fast fossil rotation of neutron star cores. *Astrophys. J.* **2012**, *761*, 32. [CrossRef]
123. Dehman, C.; Viganò, D.; Pons, J.A.; Rea, N. 3D code for MAgneto-Thermal evolution in Isolated Neutron Stars, MATINS: The magnetic field formalism. *Mon. Not. R. Astron. Soc.* **2023**, *518*, 1222–1242. [CrossRef]
124. Pons, J.A.; Perna, R. Magnetars versus high magnetic field pulsars: A theoretical interpretation of the apparent dichotomy. *Astrophys. J.* **2011**, *741*, 123. [CrossRef]
125. Suvorov, A.G. Wave-optical effects in the microlensing of continuous gravitational waves by star clusters. *Astrophys. J.* **2022**, *930*, 13. [CrossRef]
126. Braithwaite, J.; Nordlund, Å. Stable magnetic fields in stellar interiors. *Astron. Astrophys.* **2006**, *450*, 1077–1095. [CrossRef]
127. Lorimer, D.R.; Kramer, M. *Handbook of Pulsar Astronomy*; Cambridge University Press: Cambridge, UK, 2004; Volume 4.
128. Goldreich, P.; Reisenegger, A. Magnetic field decay in isolated neutron stars. *Astrophys. J.* **1992**, *395*, 250–258. [CrossRef]
129. Gourgouliatos, K.N.; Lander, S.K. Axisymmetric magneto-plastic evolution of neutron-star crusts. *Mon. Not. R. Astron. Soc.* **2021**, *506*, 3578–3587. [CrossRef]
130. Suvorov, A.G.; Melatos, A. Evolutionary implications of a magnetar interpretation for GLEAM-X J162759. 5–523504.3. *Mon. Not. R. Astron. Soc.* **2023**, *520*, 1590–1600. [CrossRef]
131. Aguilera, D.N.; Pons, J.A.; Miralles, J.A. The impact of magnetic field on the thermal evolution of neutron stars. *Astrophys. J.* **2008**, *673*, L167. [CrossRef]
132. Gourgouliatos, K.N.; Cumming, A. Hall attractor in axially symmetric magnetic fields in neutron star crusts. *Phys. Rev. Lett.* **2014**, *112*, 171101. [CrossRef]
133. Igoshev, A.P.; Popov, S.B. How to make a mature accreting magnetar. *Mon. Not. R. Astron. Soc.* **2018**, *473*, 3204–3210. [CrossRef]
134. Ho, W.C.G.; Andersson, N.; Graber, V. Dynamical onset of superconductivity and retention of magnetic fields in cooling neutron stars. *Phys. Rev. C* **2017**, *96*, 065801. [CrossRef]
135. Suvorov, A.G.; Glampedakis, K. Does the Gamma-Ray Binary LS I+ 61° 303 Harbor a Magnetar? *Astrophys. J.* **2022**, *940*, 128. [CrossRef]
136. Eichler, D.; Livio, M.; Piran, T.; Schramm, D.N. Nucleosynthesis, neutrino bursts and γ-rays from coalescing neutron stars. *Nature* **1989**, *340*, 126–128. [CrossRef]
137. Rosswog, S.; Liebendörfer, M. High-resolution calculations of merging neutron stars—II. Neutrino emission. *Mon. Not. R. Astron. Soc.* **2003**, *342*, 673–689. [CrossRef]
138. Sekiguchi, Y.; Kiuchi, K.; Kyutoku, K.; Shibata, M. Gravitational waves and neutrino emission from the merger of binary neutron stars. *Phys. Rev. Lett.* **2011**, *107*, 051102. [CrossRef] [PubMed]

139. Chamel, N.; Haensel, P. Physics of neutron star crusts. *Living Rev. Relativ.* **2008**, *11*, 10. [CrossRef]

140. Farouki, R.T.; Hamaguchi, S. Thermal energy of the crystalline one-component plasma from dynamical simulations. *Phys. Rev. E* **1993**, *47*, 4330 [CrossRef]

141. Gittins, F.; Celora, T.; Beri, A.; Andersson, N. Modelling Neutron-Star Ocean Dynamics. *Universe* **2023**, *9*, 226. [CrossRef]

142. Gudmundsson, E.H.; Pethick, C.J.; Epstein, R.I. Structure of neutron star envelopes. *Astrophys. J.* **1983**, *272*, 286–300. [CrossRef]

143. Lorenz, C.P.; Ravenhall, D.G.; Pethick, C.J. Neutron star crusts. *Phys. Rev. Lett.* **1993**, *70*, 379. [CrossRef]

144. Negele, J.W.; Vautherin, D. Neutron star matter at sub-nuclear densities. *Nucl. Phys. A* **1973**, *207*, 298–320. [CrossRef]

145. Harutyunyan, A.; Sedrakian, A. Electrical conductivity of a warm neutron star crust in magnetic fields. *Phys. Rev. C* **2016**, *94*, 025805. [CrossRef]

146. Truesdell, C.; Noll, W.; *The Non-Linear Field Theories of Mechanics [Electronic Resource]*; Springer: Berlin, Heidelberg, Germany, 2004.

147. Andersson, N.; Comer, G.L. Relativistic fluid dynamics: Physics for many different scales. *Living Rev. Relativ.* **2021**, *24*, 3. [CrossRef]

148. Sotani, H.; Suvorov, A.G.; Kokkotas, K.D. Couplings of torsional and shear oscillations in a neutron star crust. *Phys. Rev. D* **2024**, *110*, 023035. [CrossRef]

149. Pethick, C.J.; Potekhin, A.Y. Liquid crystals in the mantles of neutron stars. *Phys. Lett. B* **1998**, *427*, 7–12. [CrossRef]

150. Strohmayer, T.; Ogata, S.; Iyetomi, H.; Ichimaru, S.; van Horn, H.M. The shear modulus of the neutron star crust and nonradial oscillations of neutron stars. *Astrophys. J.* **1991**, *375*, 679–686. [CrossRef]

151. Horowitz, C.J.; Hughto, J. Molecular dynamics simulation of shear moduli for Coulomb crystals. *arXiv* **2008**, arXiv:0812.2650.

152. Baiko, D.A. Shear modulus of neutron star crust. *Mon. Not. R. Astron. Soc.* **2011**, *416*, 22–31. [CrossRef]

153. Beloborodov, A.M.; Levin, Y. Thermoplastic waves in magnetars. *Astrophys. J. Lett.* **2014**, *794*, L24. [CrossRef]

154. Carter, B.; Quintana, H. Foundations of general relativistic high-pressure elasticity theory. *Proc. R. Soc. Lond. Ser. A* **1972**, *331*, 57–83.

155. Kojima, Y. Correct criterion of crustal failure driven by intense magnetic stress in neutron stars. *arXiv* **2024**, arXiv:2408.14100. [CrossRef]

156. Kerin, A.D.; Melatos, A. Mountain formation by repeated, inhomogeneous crustal failure in a neutron star. *Mon. Not. R. Astron. Soc.* **2022**, *514*, 1628–1644. [CrossRef]

157. Ruderman, M. Crust-breaking by neutron superfluids and the VELA pulsar glitches. *Astrophys. J.* **1976**, *203*, 213–222. [CrossRef]

158. Suvorov, A.G. The radio shut-off, glitch, and X-ray burst in 1E 1547.0-5408 interpreted through magnetic reconfiguration. *Mon. Not. R. Astron. Soc.* **2023**, *523*, 4089–4096. [CrossRef]

159. Lander, S.K.; Andersson, N.; Antonopoulou, D.; Watts, A.L. Magnetically driven crustquakes in neutron stars. *Mon. Not. R. Astron. Soc.* **2015**, *449*, 2047–2058. [CrossRef]

160. Jones, P.B. Nature of fault planes in solid neutron star matter. *Astrophys. J.* **2003**, *595*, 342. [CrossRef]

161. Li, X.; Levin, Y.; Beloborodov, A.M. Magnetar outbursts from avalanches of Hall waves and crustal failures. *Astrophys. J.* **2016**, *833*, 189. [CrossRef]

162. Horowitz, C.J.; Kadau, K. Breaking strain of neutron star crust and gravitational waves. *Phys. Rev. Lett.* **2009**, *102*, 191102. [CrossRef] [PubMed]

163. Kozhberov, A.A.; Yakovlev, D.G. Deformed crystals and torsional oscillations of neutron star crust. *Mon. Not. R. Astron. Soc.* **2020**, *498*, 5149–5158. [CrossRef]

164. Smoluchowski, R. Frequency of pulsar starquakes. *Phys. Rev. Lett.* **1970**, *24*, 923. [CrossRef]

165. Kittel, C. *Introduction to Solid State Physics*; Wiley, New York, 1976.

166. Ruderman, R. Neutron star crustal plate tectonics. II-Evolution of radio pulsar magnetic fields. III-Cracking, glitches, and gamma-ray bursts. *Astrophys. J.* **1991**, *382*, 576–593. [CrossRef]

167. Chugunov, A.I.; Horowitz, C.J. Breaking stress of neutron star crust. *Mon. Not. R. Astron. Soc.* **2010**, *407*, L54–L58. [CrossRef]

168. Hoffman, K.; Heyl, J. Mechanical properties of non-accreting neutron star crusts. *Mon. Not. R. Astron. Soc.* **2012**, *426*, 2404–2412. [CrossRef]

169. Fattoyev, F.J.; Horowitz, C.J.; Lu, H. Crust breaking and the limiting rotational frequency of neutron stars. *arXiv* **2018**, arXiv:1804.04952.

170. Baiko, D.A.; Chugunov, A.I. Breaking properties of neutron star crust. *Mon. Not. R. Astron. Soc.* **2018**, *480*, 5511–5516. [CrossRef]

171. Caplan, M.E.; Schneider, A.S.; Horowitz, C.J. Elasticity of nuclear pasta. *Phys. Rev. Lett.* **2018**, *121*, 132701. [CrossRef] [PubMed]

172. Kozhberov, A.A. Breaking properties of multicomponent neutron star crust. *Mon. Not. R. Astron. Soc.* **2023**, *523*, 4855–4858. [CrossRef]

173. Baiko, D.A. Liquid-phase epitaxy of neutron star crusts and white dwarf cores. *Mon. Not. R. Astron. Soc.* **2024**, *528*, 408–417. [CrossRef]

174. Aerts, C.; Christensen-Dalsgaard, J.; Kurtz, D.W. *Asteroseismology*; Springer: Dordrecht, The Netherlands, 2010.

175. Unno, W.; Osaki, Y.; Ando, H.; Shibahashi, H. *Nonradial Oscillations of Stars*; University of Tokyo Press: Tokyo, Japan, 1979.

176. Andersson, N.; Pnigouras, P. Exploring the effective tidal deformability of neutron stars. *Phys. Rev. D* **2020**, *101*, 083001 [CrossRef]

177. Ho, W.C.G.; Andersson, N. New dynamical tide constraints from current and future gravitational wave detections of inspiralling neutron stars. *Phys. Rev. D* **2023**, *108*, 043003. [CrossRef]

178. Xu, W.; Lai, D. Resonant tidal excitation of oscillation modes in merging binary neutron stars: Inertial-gravity modes. *Phys. Rev. D* **2017**, *96*, 083005. [CrossRef]
179. Haensel, P.; Potekhin, A.Y. Analytical representations of unified equations of state of neutron-star matter. *Astron. Astrophys.* **2004**, *428*, 191–197. [CrossRef]
180. Hiscock, W.A.; Lindblom, L. Stability and causality in dissipative relativistic fluids. *Ann. Phys.* **1983**, *151*, 466–496. [CrossRef]
181. Israel, W. Nonstationary irreversible thermodynamics: A causal relativistic theory. *Ann. Phys.* **1976**, *100*, 310–331. [CrossRef]
182. Israel, W.; Stewart, J.M. Transient relativistic thermodynamics and kinetic theory. *Ann. Phys.* **1979**, *118*, 341–372. [CrossRef]
183. Stewart, J.M. On transient relativistic thermodynamics and kinetic theory. *Proc. R. Soc. Lond. Ser. A* **1977**, *357*, 59–75.
184. Andersson, N.; Pnigouras, P. The g-mode spectrum of reactive neutron star cores. *Mon. Not. R. Astron. Soc.* **2019**, *489*, 4043–4048. [CrossRef]
185. Counsell, A.R.; Gittins, F.; Andersson, N. The impact of nuclear reactions on the neutron-star g-mode spectrum. *Mon. Not. R. Astron. Soc.* **2024**, *531*, 1721–1729. [CrossRef]
186. Hammond, P.; Hawke, I.; Andersson, N. Thermal aspects of neutron star mergers. *Phys. Rev. D* **2021**, *104*, 103006. [CrossRef]
187. Ripley, J.L.; K, R.A.H.; Yunes, N. Probing internal dissipative processes of neutron stars with gravitational waves during the inspiral of neutron star binaries. *Phys. Rev. D* **2023**, *108*, 103037. [CrossRef]
188. Saketh, M.V.S.; Zhou, Z.; Ghosh, S.; Steinhoff, J.; Chatterjee, D. Investigating tidal heating in neutron stars via gravitational Raman scattering. *arXiv* **2024**, arXiv:2407.08327. [CrossRef]
189. Ripley, J.L.; Hegade KR, A.; Chandramouli, R.S.; Yunes, N. A constraint on the dissipative tidal deformability of neutron stars. *Nat. Astron.* **2024**, *8*, 1277–1283. [CrossRef]
190. Shapiro, S.L.; Teukolsky, S.A. *Black Holes, White Dwarfs and Neutron Stars: The Physics of Compact Objects*; Wiley: New York, NY, USA, 1983.
191. Haskell, B.; Sedrakian, A. Superfluidity and Superconductivity in Neutron Stars. In *The Physics and Astrophysics of Neutron Stars*; Astrophysics and Space Science Library; Rezzolla, L., Pizzochero, P., Jones, D.I., Rea, N., Vidaña, I., Eds.; Springer: Cham, Switzerland, 2018; Volume 457, p. 401.
192. Migdal, A.B. Superfluidity and the moments of inertia of nuclei. *Nucl. Phys.* **1959**, *13*, 655–674. [CrossRef]
193. Ginzburg, V.L.; Kirzhniz, D.A. On the superfluidity of neutron stars. *Zh. Eksperim Teor. Fiz.* **1964**, *47*, 2006.
194. Drissi, M.; Rios, A. Many-body approximations to the superfluid gap and critical temperature in pure neutron matter. *Eur. Phys. J. A* **2022**, *58*, 90. [CrossRef]
195. Gandolfi, S.; Palkanoglou, G.; Carlson, J.; Gezerlis, A.; Schmidt, K.E. The $^1S_0$ pairing gap in neutron matter. *Condens. Matter* **2022**, *7*, 19. [CrossRef]
196. Krotscheck, E.; Papakonstantinou, P.; Wang, J. Triplet pairing in neutron matter. *Astrophys. J.* **2023**, *955*, 76. [CrossRef]
197. Andersson, N. A superfluid perspective on neutron star dynamics. *Universe* **2021**, *7*, 17. [CrossRef]
198. Ye, C.S.; Fong, W.-F.; Kremer, K.; Rodriguez, C.L.; Chatterjee, S.; Fragione, G.; Rasio, F.A. On the rate of neutron star binary mergers from globular clusters. *Astrophys. J.* **2020**, *888*, L10. [CrossRef]
199. Wolf, R.A. Some effects of the strong interactions on the properties of neutron-star matter. *Astrophys. J.* **1966**, *145*, 834. [CrossRef]
200. Passamonti, A.; Andersson, N.; Ho, W.C.G. Buoyancy and g-modes in young superfluid neutron stars. *Mon. Not. R. Astron. Soc.* **2016**, *455*, 1489–1511. [CrossRef]
201. Kantor, E.M.; Gusakov, M.E. Composition temperature-dependent g modes in superfluid neutron stars. *Mon. Not. R. Astron. Soc.* **2014**, *442*, L90–L94. [CrossRef]
202. Yu, H.; Weinberg, N.N. Resonant tidal excitation of superfluid neutron stars in coalescing binaries. *Mon. Not. R. Astron. Soc.* **2017**, *464*, 2622–2637. [CrossRef]
203. Rau, P.B.; Wasserman, I. Compressional modes in two-superfluid neutron stars with leptonic buoyancy. *Mon. Not. R. Astron. Soc.* **2018**, *481*, 4427–4444. [CrossRef]
204. Yu, H.; Weinberg, N.N.; Arras, P.; Kwon, J.; Venumadhav, T. Beyond the linear tide: Impact of the non-linear tidal response of neutron stars on gravitational waveforms from binary inspirals. *Mon. Not. R. Astron. Soc.* **2023**, *519*, 4325–4343. [CrossRef]
205. Yu, H.; Arras, P.; Weinberg, N.N. Dynamical tides during the inspiral of rapidly spinning neutron stars: Solutions beyond mode resonance. *Phys. Rev. D* **2024**, *110*, 024039. [CrossRef]
206. Lander, S.K. Magnetic fields in superconducting neutron stars. *Phys. Rev. Lett.* **2013**, *110*, 071101. [CrossRef]
207. Suvorov, A.G. Ultra-compact X-ray binaries as dual-line gravitational-wave sources. *Mon. Not. R. Astron. Soc.* **2021**, *503*, 5495–5503. [CrossRef]
208. Glampedakis, K.; Andersson, N.; Samuelsson, L. Magnetohydrodynamics of superfluid and superconducting neutron star cores. *Mon. Not. R. Astron. Soc.* **2011**, *410*, 805–829. [CrossRef]
209. Taam, R.E.; Sandquist, E.L. Common envelope evolution of massive binary stars. *Annu. Rev. Astron. Astrophys.* **2000**, *38*, 113–141. [CrossRef]
210. Peters, P.C. Gravitational radiation and the motion of two point masses. *Phys. Rev.* **1964**, *136*, 1224. [CrossRef]
211. Peters, P.C.; Mathews, J. Gravitational radiation from point masses in a Keplerian orbit. *Phys. Rev.* **1963**, *131*, 435. [CrossRef]
212. Lai, D.; Rasio, F.A.; Shapiro, S.L. Equilibrium, stability and orbital evolution of close binary systems. *Astrophys. J.* **1994**, *423*, 344. [CrossRef]

213. Lai, D.; Rasio, F.A.; Shapiro, S.L. Hydrodynamic instability and coalescence of binary neutron stars. *Astrophys. J.* **1994**, *420*, 811. [CrossRef]

214. Kochanek, C.S. Coalescing binary neutron stars. *Astrophys. J.* **1992**, *398*, 234–247. [CrossRef]

215. Pnigouras, P.; Gittins, F.; Nanda, A.; Andersson, N.; Jones, D.I. The dynamical tides of spinning Newtonian stars. *Mon. Not. R. Astron. Soc.* **2024**, *527*, 8409–8428. [CrossRef]

216. Knee, A.M.; Romero-Shaw, I.M.; Lasky, P.D.; McIver, J.; Thrane, E. A Rosetta Stone for eccentric gravitational waveform models. *Astrophys. J.* **2022**, *936*, 172. [CrossRef]

217. Pitre, T.; Poisson, E. General relativistic dynamical tides in binary inspirals without modes. *Phys. Rev. D* **2024**, *109*, 064004. [CrossRef]

218. Lai, D.; Wu, Y. Resonant tidal excitations of inertial modes in coalescing neutron star binaries. *Phys. Rev. D* **2006**, *74*, 024007. [CrossRef]

219. Press, W.H.; Teukolsky, S.A. On formation of close binaries by two-body tidal capture. *Astrophys. J.* **1977**, *213*, 183–192. [CrossRef]

220. Reisenegger, A.; Goldreich, P. Excitation of neutron star normal modes during binary inspiral. *Astrophys. J.* **1994**, *426*, 688–691. [CrossRef]

221. Zahn, J.P. Les marées dans une étoile double serrée. *Ann. d'Astrophys.* **1966**, *29*, 313

222. Zahn, J.P. Tidal friction in close binary stars. *Astron. Astrophys.* **1977**, *57*, 383–394.

223. Ho, W.C.G.; Lai, D. Resonant tidal excitations of rotating neutron stars in coalescing binaries. *Mon. Not. R. Astron. Soc.* **1999**, *308*, 153–166.

224. Kuan, H.-J.; Suvorov, A.G.; Kokkotas, K.D. General-relativistic treatment of tidal g-mode resonances in coalescing binaries of neutron stars–I. Theoretical framework and crust breaking. *Mon. Not. R. Astron. Soc.* **2021**, *506*, 2985–2998. [CrossRef]

225. Passamonti, A.; Andersson, N.; Pnigouras, P. Dynamical tides in neutron stars: the impact of the crust. *Mon. Not. R. Astron. Soc.* **2021**, *504*, 1273–1293. [CrossRef]

226. Strohmayer, T.E. Oscillations of rotating neutron stars. *Astrophys. J.* **1991**, *372*, 573–591. [CrossRef]

227. Denis, J. Tidal Perturbation of the Non-Radial Oscillations of a Star. *Astron. Astrophys.* **1972**, *20*, 151.

228. Miao, Z.; Zhou, E.; Li, A. Resolving phase transition properties of dense matter through tidal-excited g-mode from inspiralling neutron stars. *Astrophys. J.* **2024**, *964*, 31. [CrossRef]

229. Reisenegger, A. Multipole moments of stellar oscillation modes. *Astrophys. J.* **1994**, *432*, 296. [CrossRef]

230. Alexander, M.E. Tidal resonances in binary star systems. *Mon. Not. R. Astron. Soc.* **1987**, *227*, 843–861. [CrossRef]

231. Alexander, M.E. Tidal resonances in binary star systems: Pt. 2. Slowly rotating stars. *Mon. Not. R. Astron. Soc.* **1988**, *235*, 1367. [CrossRef]

232. Schäfer, G.; Jaranowski, P. Hamiltonian formulation of general relativity and post-Newtonian dynamics of compact binaries. *Living Rev. Relativ.* **2024**, *27*, 2. [CrossRef]

233. Kokkotas, K.D.; Schafer, G. Tidal and tidal-resonant effects in coalescing binaries. *Mon. Not. R. Astron. Soc.* **1995**, *275*, 301–308. [CrossRef]

234. Schäfer, G. The gravitational quadrupole radiation-reaction force and the canonical formalism of ADM. *Ann. Phys.* **1985**, *161*, 81–100. [CrossRef]

235. Yagi, K.; Stein, L.C.; Yunes, N. Challenging the presence of scalar charge and dipolar radiation in binary pulsars. *Phys. Rev. D* **2016**, *93*, 024010. [CrossRef]

236. Thorne, K.S. Multipole expansions of gravitational radiation. *Rev. Mod. Phys.* **1980**, *52*, 299. [CrossRef]

237. Yunes, N.; Yagi, K.; Pretorius, F. Theoretical physics implications of the binary black-hole mergers GW150914 and GW151226. *Phys. Rev. D* **2016**, *94*, 084002. [CrossRef]

238. Andersson, N.; Gittins, F.; Yin, S.; Panosso Macedo, R. Building post-Newtonian neutron stars. *Class. Quantum Gravity* **2023**, *40*, 025016. [CrossRef]

239. Wagoner, R.V.; Malone, R.C. Post-Newtonian neutron stars. *Astrophys. J.* **1974**, *189*, L75. [CrossRef]

240. Minaev, S.; Will, C.M. Compact binary systems in scalar-tensor gravity:<? format?> Equations of motion to 2.5 post-Newtonian order. *Phys. Rev. D* **2013**, *87*, 084070.

241. Blanchet, L.; Damour, T.; Iyer, B.R.; Will, C.M.; Wiseman, A.G. Gravitational-radiation damping of compact binary systems to second post-Newtonian order. *Phys. Rev. Lett.* **1995**, *74*, 3515. [CrossRef]

242. Ioka, K.; Taniguchi, K. Gravitational waves from inspiraling compact binaries with magnetic dipole moments. *Astrophys. J.* **2000**, *537*, 327. [CrossRef]

243. Poisson, E. Gravitational waves from inspiraling compact binaries: The quadrupole-moment term. *Phys. Rev. D* **1998**, *57*, 5287. [CrossRef]

244. Blanchet, L. Gravitational-wave tails of tails. *Class. Quantum Gravity* **1998**, *15*, 113. [CrossRef]

245. Damour, T.; Nagar, A.; Villain, L.Measurability of the tidal polarizability of neutron stars in late-inspiral gravitational-wave signals. *Phys. Rev. D* **2012**, *85*, 123007. [CrossRef]

246. Yagi, K. Multipole love relations. *Phys. Rev. D* **2014**, *89*, 043011. [CrossRef]

247. Abdelsalhin, T.; Gualtieri, L.; Pani, P. Post-Newtonian spin-tidal couplings for compact binaries. *Phys. Rev. D* **2018**, *98*, 104046. [CrossRef]

248. Henry, Q.; Faye, G.; Blanchet, L. Tidal effects in the gravitational-wave phase evolution of compact binary systems to next-to-next-to-leading post-Newtonian order. *Phys. Rev. D* **2020**, *102*, 044033. [CrossRef]
249. Castro, G.; Gualtieri, L.; Maselli, A.; Pani, P. Impact and detectability of spin-tidal couplings in neutron star inspirals. *Phys. Rev. D* **2022**, *106*, 024011. [CrossRef]
250. Suvorov, A.G. Monopolar and quadrupolar gravitational radiation from magnetically deformed neutron stars in modified gravity. *Phys. Rev. D* **2018**, *98*, 084026. [CrossRef]
251. Cutler, C.; Flanagan, E.E. Gravitational waves from merging compact binaries: How accurately can one extract the binary's parameters from the inspiral waveform? *Phys. Rev. D* **1994**, *49*, 2658. [CrossRef]
252. Finn, L.S.; Chernoff, D.F. Observing binary inspiral in gravitational radiation: One interferometer. *Phys. Rev. D* **1993**, *47*, 2198. [CrossRef]
253. Damour, T. *Gravitational Radiation*; Deruelle, N., Piran, T., Eds.; North-Holland: Amsterdam, The Netherlands, 1983; p. 58.
254. Binnington, T.; Poisson, E. Relativistic theory of tidal Love numbers. *Phys. Rev. D* **2009**, *80*, 084018. [CrossRef]
255. Damour, T.; Nagar, A.Relativistic tidal properties of neutron stars. *Phys. Rev. D* **2009**, *80*, 084035. [CrossRef]
256. Pani, P.; Gualtieri, L.; Abdelsalhin, T.; Jiménez-Forteza, X. Magnetic tidal Love numbers clarified. *Phys. Rev. D* **2018**, *98*, 124023. [CrossRef]
257. Pani, P.; Gualtieri, L.; Ferrari, V. Tidal Love numbers of a slowly spinning neutron star. *Phys. Rev. D* **2015**, *92*, 124003. [CrossRef]
258. Hansen, R.O. Multipole moments of stationary space-times. *J. Math. Phys.* **1974**, *15*, 46–52. [CrossRef]
259. Gürsel, Y. Multipole moments for stationary systems: The equivalence of the Geroch-Hansen formulation and the Thorne formulation. *Gen. Relativ. Gravit.* **1983**, *15*, 737–754. [CrossRef]
260. Damour, T.; Soffel, M.; Xu, C. General-relativistic celestial mechanics. I. Method and definition of reference systems. *Phys. Rev. D* **1991**, *43*, 3273 [CrossRef]
261. Pappas, G.; Sotiriou, T.P. Multipole moments in scalar-tensor theory of gravity. *Phys. Rev. D* **2015**, *91*, 044011. [CrossRef]
262. Bernuzzi, S.; Nagar, A.; Dietrich, T.; Damour, T. Modeling the dynamics of tidally interacting binary neutron stars up to the merger. *Phys. Rev. Lett.* **2015**, *114*, 161103. [CrossRef]
263. Bini, D.; Damour, T.; Faye, G. Effective action approach to higher-order relativistic tidal interactions<? format?> in binary systems and their effective one body description. *Phys. Rev. D* **2012**, *85*, 124034.
264. Hinderer, T.; Taracchini, A.; Foucart, F.; Buonanno, A.; Steinhoff, J.; Duez, M.; Kidder, L.E.; Pfeiffer, H.P.; Scheel, M.A.; Szilagyi, B.; et al. Effects of neutron-star dynamic tides on gravitational waveforms within the effective-one-body approach. *Phys. Rev. Lett.* **2016**, *116*, 181101. [CrossRef]
265. Baiotti, L.; Damour, T.; Giacomazzo, B.; Nagar, A.; Rezzolla, L. Analytic modeling of tidal effects in the relativistic inspiral of binary neutron stars. *Phys. Rev. Lett.* **2010**, *105*, 261101. [CrossRef]
266. Bernuzzi, S.; Thierfelder, M.; Brügmann, B. Accuracy of numerical relativity waveforms from binary neutron star mergers<? format?> and their comparison with post-Newtonian waveforms. *Phys. Rev. D* **2012**, *85*, 104030.
267. Damour, T.; Nagar, A. Effective one body description of tidal effects in inspiralling compact binaries. *Phys. Rev. D* **2010**, *81*, 084016. [CrossRef]
268. Flanagan, É.É.; Hinderer, T. Constraining neutron-star tidal Love numbers with gravitational-wave detectors. *Phys. Rev. D* **2008**, *77*, 021502. [CrossRef]
269. Hinderer, T. Tidal Love numbers of neutron stars. *Astrophys. J.* **2008**, *677*, 1216. [CrossRef]
270. Hinderer, T.; Lackey, B.D.; Lang, R.N.; Read, J.S. Tidal deformability of neutron stars with realistic equations of state<? format?> and their gravitational wave signatures in binary inspiral. *Phys. Rev. D* **2010**, *81*, 123016.
271. Buonanno, A.; Damour, T. Effective one-body approach to general relativistic two-body dynamics. *Phys. Rev. D* **1999**, *59*, 084006. [CrossRef]
272. Buonanno, A.; Damour, T. Transition from inspiral to plunge in binary black hole coalescences. *Phys. Rev. D* **2000**, *62*, 064015. [CrossRef]
273. Bini, D.; Damour, T. Gravitational self-force corrections to two-body tidal interactions and the effective one-body formalism. *Phys. Rev. D* **2014**, *90*, 124037. [CrossRef]
274. Andersson, N. A gravitational-wave perspective on neutron-star seismology. *Universe* **2021**, *7*, 97. [CrossRef]
275. Andersson, N.; Kokkotas, K.D. Towards gravitational wave asteroseismology. *Mon. Not. R. Astron. Soc.* **1998**, *299*, 1059–1068. [CrossRef]
276. Kokkotas, K.D.; Apostolatos, T.A.; Andersson, N. The inverse problem for pulsating neutron stars: A 'fingerprint analysis' for the supranuclear equation of state. *Mon. Not. R. Astron. Soc.* **2001**, *320*, 307–315. [CrossRef]
277. Pratten, G.; Schmidt, P.; Hinderer, T. Gravitational-wave asteroseismology with fundamental modes from compact binary inspirals. *Nat. Commun.* **2020**, *11*, 2553. [CrossRef]
278. Colaiuda, A.; Kokkotas, K.D. Magnetar oscillations in the presence of a crust. *Mon. Not. R. Astron. Soc.* **2011**, *414*, 3014–3022. [CrossRef]
279. Gabler, M.; Cerdá-Durán, P.; Stergioulas, N.; Font, J.A.; Müller, E. Magnetoelastic oscillations of neutron stars with dipolar magnetic fields. *Mon. Not. R. Astron. Soc.* **2012**, *421*, 2054–2078. [CrossRef]
280. Gabler, M.; Cerdá-Durán, P.; Stergioulas, N.; Font, J.A.; Müller, E. Coherent magneto-elastic oscillations in superfluid magnetars. *Mon. Not. R. Astron. Soc.* **2016**, *460*, 4242–4257. [CrossRef]

281. Lockitch, K.H.; Friedman, J.L. Where are the r-modes of isentropic stars? *Astrophys. J.* **1999**, *521*, 764. [CrossRef]
282. Papaloizou, J.; Pringle, J.E. On the rotational modes of fully convective stars with application to close binary systems. *Mon. Not. R. Astron. Soc.* **1981**, *195*, 743–753. [CrossRef]
283. Kuan, H.-J.; Kokkotas, K.D. f-mode imprints on gravitational waves from coalescing binaries involving aligned spinning neutron stars. *Phys. Rev. D* **2022**, *106*, 064052. [CrossRef]
284. Kuan, H.-J.; Kokkotas, K.D. Last three seconds: Packed message delivered by tides in binary neutron star mergers. *Phys. Rev. D* **2023**, *108*, 063026. [CrossRef]
285. Lai, D. Resonant oscillations and tidal heating in coalescing binary neutron stars. *Mon. Not. R. Astron. Soc.* **1994**, *270*, 611–629. [CrossRef]
286. Pratten, G.; Schmidt, P.; Williams, N. Impact of dynamical tides on the reconstruction of the neutron star equation of state. *Phys. Rev. Lett.* **2022**, *129*, 081102. [CrossRef]
287. Williams, N.; Pratten, G.; Schmidt, P. Prospects for distinguishing dynamical tides in inspiralling binary neutron stars with third generation gravitational-wave detectors. *Phys. Rev. D* **2022**, *105*, 123032. [CrossRef]
288. Tsang, D.; Read, J.S.; Hinderer, T.; Piro, A.L.; Bondarescu, R. Resonant shattering of neutron star crusts. *Phys. Rev. Lett.* **2012**, *108*, 011102. [CrossRef]
289. Sullivan, A.G.; Alves, L.M.B.; Márka, Z.; Bartos, I.; Márka, S. Gamma-ray burst precursors from tidally resonant neutron star oceans: Potential implications for GRB 211211A. *Mon. Not. R. Astron. Soc.* **2024**, *527*, 7722–7730. [CrossRef]
290. Kokkotas, K.D.; Schmidt, B.G. Quasi-normal modes of stars and black holes. *Living Rev. Relativ.* **1999**, *2*, 2. [CrossRef]
291. Andersson, N.; Pnigouras, P. The phenomenology of dynamical neutron star tides. *Mon. Not. R. Astron. Soc.* **2021**, *503*, 533–539. [CrossRef]
292. Gamba, R.; Bernuzzi, S. Resonant tides in binary neutron star mergers: Analytical-numerical relativity study. *Phys. Rev. D* **2023**, *107*, 044014. [CrossRef]
293. Ma, S.; Yu, H.; Chen, Y. Excitation of f-modes during mergers of spinning binary neutron star. *Phys. Rev. D* **2020**, *101*, 123020. [CrossRef]
294. Steinhoff, J.; Hinderer, T.; Buonanno, A.; Taracchini, A. Dynamical tides in general relativity: Effective action and effective-one-body Hamiltonian. *Phys. Rev. D* **2016**, *94*, 104028. [CrossRef]
295. Steinhoff, J.; Hinderer, T.; Dietrich, T.; Foucart, F. Spin effects on neutron star fundamental-mode dynamical tides: Phenomenology and comparison to numerical simulations. *Phys. Rev. Res.* **2021**, *3*, 033129. [CrossRef]
296. Gittins, F.; Andersson, N. Neutron-star seismology with realistic, finite-temperature nuclear matter. *arXiv* **2024**, arXiv:2406.05177.
297. Cowling, T.G.; Newing, R.A. The Oscillations of a Rotating Star. *Astrophys. J.* **1949**, *109*, 149. [CrossRef]
298. Gaertig, E.; Kokkotas, K.D. Oscillations of rapidly rotating relativistic stars. *Phys. Rev. D* **2008**, *78*, 064063. [CrossRef]
299. Ledoux, P. The Nonradial Oscillations of Gaseous Stars and the Problem of Beta Canis Majoris. *Astrophys. J.* **1951**, *114*, 373. [CrossRef]
300. Yoshida, S.; Rezzolla, L.; Karino, S.; Eriguchi, Y. Frequencies of f-modes in differentially rotating relativistic stars and secular stability limits. *Astrophys. J.* **2002**, *568*, L41. [CrossRef]
301. Dudi, R.; Dietrich, T.; Rashti, A.; Brügmann, B.; Steinhoff, J.; Tichy, W. High-accuracy simulations of highly spinning binary neutron star systems. *Phys. Rev. D* **2022**, *105*, 064050. [CrossRef]
302. Read, J.S.; Lackey, B.D.; Owen, B.J.; Friedman, J.L. Constraints on a phenomenologically parametrized neutron-star equation of state. *Phys. Rev. D* **2009**, *79*, 124032. [CrossRef]
303. Akcay, S.; Bernuzzi, S.; Messina, F.; Nagar, A.; Ortiz, N.; Rettegno, P. Effective-one-body multipolar waveform for tidally interacting binary neutron stars up to merger. *Phys. Rev. D* **2019**, *99*, 044051. [CrossRef]
304. Nagar, A.; Bernuzzi, S.; Del Pozzo, W.; Riemenschneider, G.; Akcay, S.; Carullo, G.; Fleig, P.; Babak, S.; Tsang, K.W.; Colleoni, M.; et al. Time-domain effective-one-body gravitational waveforms for coalescing compact binaries with nonprecessing spins, tides, and self-spin effects. *Phys. Rev. D* **2018**, *98*, 104052. [CrossRef]
305. Abac, A.; Dietrich, T.; Buonanno, A.; Steinhoff, J.; Ujevic, M. New and robust gravitational-waveform model for high-mass-ratio binary neutron star systems with dynamical tidal effects. *Phys. Rev. D* **2024**, *109*, 024062. [CrossRef]
306. Dietrich, T.; Bernuzzi, S.; Tichy, W. Closed-form tidal approximants for binary neutron star gravitational waveforms constructed from high-resolution numerical relativity simulations. *Phys. Rev. D* **2017**, *96*, 121501. [CrossRef]
307. Dietrich, T.; Samajdar, A.; Khan, S.; Johnson-McDaniel, N.K.; Dudi, R.; Tichy, W. Improving the NRTidal model for binary neutron star systems. *Phys. Rev. D* **2019**, *100*, 044003. [CrossRef]
308. Dietrich, T.; Khan, S.; Dudi, R.; Kapadia, S.J.; Kumar, P.; Nagar, A.; Ohme, F.; Pannarale, F.; Samajdar, A.; Bernuzzi, S.; et al. Matter imprints in waveform models for neutron star binaries: Tidal and self-spin effects. *Phys. Rev. D* **2019**, *99*, 024029. [CrossRef]
309. Williams, N.; Schmidt, P.; Pratten, G. Phenomenological model of gravitational self-force enhanced tides in inspiralling binary neutron stars. *arXiv* **2024**, arXiv:2407.08538.
310. Suvorov, A.G.; Kokkotas, K.D. Precursor flares of short gamma-ray bursts from crust yielding due to tidal resonances in coalescing binaries of rotating, magnetized neutron stars. *Phys. Rev. D* **2020**, *101*, 083002. [CrossRef]
311. Blanchet, L. Post-Newtonian theory for gravitational waves. *Living Rev. Relativ.* **2024**, *27*, 4. [CrossRef]
312. Detweiler, S. Consequence of the gravitational self-force for circular orbits of the Schwarzschild geometry. *Phys. Rev. D* **2008**, *77*, 124026. [CrossRef]

313. Chandrasekhar, S. Solutions of two problems in the theory of gravitational radiation. *Phys. Rev. Lett.* **1970**, *24*, 611. [CrossRef]

314. Friedman, J.L.; Schutz, B.F. Langrangian perturbation theory of nonrelativistic fluids. *Astrophys. J.* **1978**, *221*, 937–957. [CrossRef]

315. Friedman, J.L.; Schutz, B.F. Secular instability of rotating Newtonian stars. *Astrophys. J.* **1978**, *222*, 281–296. [CrossRef]

316. Krüger, C.J.; Kokkotas, K.D.; Manoharan, P.; Völkel, S.H. Fast rotating neutron stars: Oscillations and instabilities. *Front. Astron. Space Sci.* **2021**, *8*, 736918. [CrossRef]

317. Doneva, D.D.; Gaertig, E.; Kokkotas, K.D.; Krüger, C. Gravitational wave asteroseismology of fast rotating neutron stars with realistic equations of state. *Phys. Rev. D* **2013**, *88*, 044052. [CrossRef]

318. Andersson, N.; Kokkotas, K.D. The r-mode instability in rotating neutron stars. *Int. J. Mod. Phys. D* **2001**, *10*, 381–441. [CrossRef]

319. Cutler, C.; Apostolatos, T.A.; Bildsten, L.; Finn, L.S.; Flanagan, E.E.; Kennefick, D.; Markovic, D.M.; Ori, A.; Poisson, E.; Sussman, G.J.; et al. The last three minutes: Issues in gravitational-wave measurements of coalescing compact binaries. *Phys. Rev. Lett.* **1993**, *70*, 2984. [CrossRef] [PubMed]

320. Kidder, L.E. Coalescing binary systems of compact objects to (post) 5/2-Newtonian order. V. Spin effects. *Phys. Rev. D* **1995**, *52*, 821. [CrossRef]

321. Kidder, L.E.; Will, C.M.; Wiseman, A.G. Spin effects in the inspiral of coalescing compact binaries. *Phys. Rev. D* **1993**, *47*, R4183 [CrossRef] [PubMed]

322. Passamonti, A.; Haskell, B.; Andersson, N.; Jones, D.I.; Hawke, I. Oscillations of rapidly rotating stratified neutron stars. *Mon. Not. R. Astron. Soc.* **2009**, *394*, 730–741. [CrossRef]

323. Bernuzzi, S.; Dietrich, T.; Tichy, W.; Brügmann, B. Mergers of binary neutron stars with realistic spin. *Phys. Rev. D* **2014**, *89*, 104021. [CrossRef]

324. Lai, D. Dynamical tides in rotating binary stars. *Astrophys. J.* **1997**, *490*, 847. [CrossRef]

325. Fuller, J.; Lai, D. Tidal excitations of oscillation modes in compact white dwarf binaries–I. Linear theory. *Mon. Not. R. Astron. Soc.* **2011**, *412*, 1331–1340. [CrossRef]

326. Racine, É.; Phinney, E.S.; Arras, P. Non-dissipative tidal synchronization in accreting binary white dwarf systems. *Mon. Not. R. Astron. Soc.* **2007**, *380*, 381–398. [CrossRef]

327. Lai, D. DC circuit powered by orbital motion: Magnetic interactions in compact object binaries and exoplanetary systems. *Astrophys. J.* **2012**, *757*, L3. [CrossRef]

328. Goldreich, P.; Lynden-Bell, D. Io, a Jovian unipolar inductor. *Astrophys. J.* **1969**, *156*, 59–78. [CrossRef]

329. Piro, A.L. Magnetic interactions in coalescing neutron star binaries. *Astrophys. J.* **2012**, *755*, 80. [CrossRef]

330. Crinquand, B.; Cerutti, B.; Dubus, G. Kinetic modeling of the electromagnetic precursor from an axisymmetric binary pulsar coalescence. *Astron. Astrophys.* **2019**, *622*, A161. [CrossRef]

331. Giacomazzo, B.; Rezzolla, L.; Baiotti, L. Can magnetic fields be detected during the inspiral of binary neutron stars? *Mon. Not. R. Astron. Soc.* **2009**, *399*, L164–L168. [CrossRef]

332. Zhu, Z.; Li, A.; Rezzolla, L. Tidal deformability and gravitational-wave phase evolution of magnetized compact-star binaries. *Phys. Rev. D* **2020**, *102*, 084058. [CrossRef]

333. Suvorov, A.G.; Glampedakis, K. Magnetic equilibria of relativistic axisymmetric stars: The impact of flow constants. *Phys. Rev. D* **2023**, *108*, 084006. [CrossRef]

334. Arras, P.; Weinberg, N.N. Urca reactions during neutron star inspiral. *Mon. Not. R. Astron. Soc.* **2019**, *486*, 1424–1436. [CrossRef]

335. Ghosh, S.; Pradhan, B.K.; Chatterjee, D. Tidal heating as a direct probe of strangeness inside neutron stars. *Phys. Rev. D* **2024**, *109*, 103036. [CrossRef]

336. Meszaros, P.; Rees, M.J. Tidal heating and mass loss in neutron star binaries-Implications for gamma-ray burst models. *Astrophys. J.* **1992**, *397*, 570–575. [CrossRef]

337. Kanakis-Pegios, A.; Koliogiannis, P.S.; Moustakidis, C.C. Thermal effects on tidal deformability in the last orbits of an inspiraling binary neutron star system. *Phys. Lett. B* **2022**, *832*, 137267. [CrossRef]

338. Alford, M.; Harutyunyan, A.; Sedrakian, A. Bulk viscous damping of density oscillations in neutron star mergers. *Particles* **2000**, *3*, 34. [CrossRef]

339. Pan, Z.; Lyu, Z.; Bonga, B.; Ortiz, N.; Yang, H. Probing crust meltdown in inspiraling binary neutron stars. *Phys. Rev. Lett.* **2020**, *125*, 201102. [CrossRef]

340. Watts, A. L. Thermonuclear burst oscillations. *Annu. Rev. Astron. Astrophys.* **2012**, *50*, 609–640. [CrossRef]

341. Lindblom, L.; Owen, B.J.; Ushomirsky, G. Effect of a neutron-star crust on the r-mode instability. *Phys. Rev. D* **2000**, *62*, 084030. [CrossRef]

342. Mardling, R.A. The Role of Chaos in the Circularization of Tidal Capture Binaries. I. The Chaos Boundary. *Astrophys. J.* **1995**, *450*, 722. [CrossRef]

343. Vick, M.; Lai, D. Dynamical tides in highly eccentric binaries: Chaos, dissipation, and quasi-steady state. *Mon. Not. R. Astron. Soc.* **2018**, *476*, 482–495. [CrossRef]

344. Chirenti, C.; Gold, R.; Miller, M.C. Gravitational waves from f-modes excited by the inspiral of highly eccentric neutron star binaries. *Astrophys. J.* **2017**, *837*, 67. [CrossRef]

345. Wang, J.-S.; Lai, D. Evolution of inspiralling neutron star binaries: Effects of tidal interactions and orbital eccentricities. *Phys. Rev. D* **2020**, *102*, 083005. [CrossRef]

346. Yang, H. Inspiralling eccentric binary neutron stars: Orbital motion and tidal resonance. *Phys. Rev. D* **2019**, *100*, 064023. [CrossRef]

347. Vick, M.; Lai, D. Tidal effects in eccentric coalescing neutron star binaries. *Phys. Rev. D* **2019**, *100*, 063001. [CrossRef]
348. Takátsy, J.; Kocsis, B.; Kovács, P. Observability of dynamical tides in merging eccentric neutron star binaries. *arXiv* **2024**, arXiv:2407.17560. [CrossRef]
349. Shibata, M. Effects of tidal resonances in coalescing compact binary systems. *Prog. Theor. Phys.* **1994**, *91*, 871–883. [CrossRef]
350. Gabler, M.; Sperhake, U.; Andersson, N. Nonlinear radial oscillations of neutron stars. *Phys. Rev. D* **2009**, *80*, 064012. [CrossRef]
351. Koshut, T.M.; Kouveliotou, C.; Paciesas, W.S.; van Paradijs, J.; Pendleton, G.N.; Briggs, M.S.; Fishman, G.J.; Meegan, C.A. Gamma-ray burst precursor activity as observed with BATSE. *Astrophys. J.* **1995**, *452*, 145. [CrossRef]
352. Troja, E.; Rosswog, S.; Gehrels, N. Precursors of short gamma-ray bursts. *Astrophys. J.* **2010**, *723*, 1711. [CrossRef]
353. Zhong, S.-Q.; Dai, Z.-G.; Cheng, J.-G.; Lan, L.; Zhang, H.-M. Precursors in short gamma-ray bursts as a possible probe of progenitors. *Astrophys. J.* **2019**, *884*, 25. [CrossRef]
354. Abbott, B.P. et al. [LIGO Scientific and Virgo Collaborations] Search for gravitational waves associated with gamma-ray bursts detected by Fermi and Swift during the LIGO–Virgo run O3b. *Astrophys. J.* **2022**, *928*, 186. [CrossRef]
355. Thöne, C.C. De Ugarte Postigo, A. Fryer, C.L. Page, K.L. Gorosabel, J. Aloy, M.A. Perley, D.A. Kouveliotou, C. Janka, H.T. Mimica, P. Racusin, J.L. Krimm, H. Cummings, J. Oates, S.R. Holland, S.T. Siegel, M.H. et al. The unusual γ-ray burst GRB 101225A from a helium star/neutron star merger at redshift 0.33. *Nature* **2011**, *480*, 72–74. [CrossRef] [PubMed]
356. Li, L.-X.; Paczyński, B. Transient events from neutron star mergers. *Astrophys. J.* **1998**, *507*, L59. [CrossRef]
357. Valenti, S.; Sand, D.J.; Yang, S.; Cappellaro, E.; Tartaglia, L.; Corsi, A.; Jha, S.W.; Reichart, D.E.; Haislip, J.; Kouprianov, V. The discovery of the electromagnetic counterpart of GW170817: Kilonova AT 2017gfo/DLT17ck. *Astrophys. J.* **2017**, *848*, L24. [CrossRef]
358. Chase, E.A.; O'Connor, B.; Fryer, C.L.; Troja, E.; Korobkin, O.;Wollaeger, R.T.; Ristic, M.; Fontes, C.J.; Hungerford, A.L.; Herring, A.M. Kilonova detectability with wide-field instruments. *Astrophys. J.* **2022**, *927*, 163. [CrossRef]
359. Yang, B.; Jin, Z.-P.; Li, X.; Covino, S.; Zheng, X.-Z.; Hotokezaka, K.; Fan, Y.-Z.; Piran, T.; Wei, D.-M. A possible macronova in the late afterglow of the long–short burst grb 060614. *Nat. Commun.* **2015**, *6*, 7323. [CrossRef]
360. Deng, Q.; Zhang, Z.B.; Li, X.J.; Chang, H.Y.; Zhang, X.L.; Zhen, H.Y.; Sun, H.; Pan, Q.; Dong, X.F. Reclassifying Swift Gamma-Ray Bursts with Diverse Duration Distributions. *Astrophys. J.* **2022**, *940*, 5. [CrossRef]
361. Rowlinson, A.; O'Brien, P.T.; Metzger, B.D.; Tanvir, N.R.; Levan, A.J. Signatures of magnetar central engines in short GRB light curves. *Mon. Not. R. Astron. Soc.* **2013**, *430*, 1061–1087. [CrossRef]
362. Suvorov, A.G.; Kokkotas, K.D. Precessing magnetars as central engines in short gamma-ray bursts. *Mon. Not. R. Astron. Soc.* **2021**, *502*, 2482–2494. [CrossRef]
363. Minaev, P.Y.; Pozanenko, A.S. Precursors of short gamma-ray bursts in the SPI-ACS/INTEGRAL experiment. *Astron. Lett.* **2017**, *43*, 1. [CrossRef]
364. Qin, S.-M.; Jiang, L.-Y.; Wang, X.-G. GRB 130310A: Very high peak energy and thermal emission. *Res. Astron. Astrophys.* **2021**, *21*, 072. [CrossRef]
365. Virgili, F.J.; Zhang, B.; O'Brien, P.; Troja, E. Are all short–hard gamma-ray bursts produced from mergers of compact stellar objects? *Astrophys. J.* **2011**, *727*, 109. [CrossRef]
366. Pavan, A.; Ciolfi, R.; Kalinani, J.V.; Mignone, A. Short gamma-ray burst jet propagation in binary neutron star merger environments. *Mon. Not. R. Astron. Soc.* **2021**, *506*, 3483–3498. [CrossRef]
367. Tsang, D. Shattering flares during close encounters of neutron stars. *Astrophys. J.* **2013**, *777*, 103. [CrossRef]
368. Meredith, T.R.L.; Wynn, G.A.; Evans, P.A. An analysis of the effect of data processing methods on magnetic propeller models in short GRBs. *Mon. Not. R. Astron. Soc.* **2023**, *519*, 418–431. [CrossRef]
369. Kuan, H.-J.; Suvorov, A.G.; Kokkotas, K.D. General-relativistic treatment of tidal g-mode resonances in coalescing binaries of neutron stars–II. As triggers for precursor flares of short gamma-ray bursts. *Mon. Not. R. Astron. Soc.* **2021**, *508*, 1732–1744. [CrossRef]
370. Gehrels, N. Confidence limits for small numbers of events in astrophysical data. *Astrophys. J.* **1986**, *303*, 336–346. [CrossRef]
371. Rastinejad, J.C.; Gompertz, B.P.; Levan, A.J.; Fong,W.; Nicholl, M.; Lamb, G.P.; Malesani, D.B.; Nugent, A.E.; Oates, S.R.; Tanvir, N.R.; et al. A kilonova following a long-duration gamma-ray burst at 350 Mpc. *Nature* **2022**, *612*, 223–227. [CrossRef]
372. Suvorov, A.G.; Kuan, H.J.; Kokkotas, K.D. Quasi-periodic oscillations in precursor flares via seismic aftershocks from resonant shattering. *Astron. Astrophys.* **2022**, *664*, A177. [CrossRef]
373. Kiuchi, K.; Kyutoku, K.; Sekiguchi, Y.; Shibata, M.; Wada, T. High resolution numerical relativity simulations for the merger of binary magnetized neutron stars. *Phys. Rev. D* **2014**, *90*, 041502. [CrossRef]
374. Chirenti, C.; Dichiara, S.; Lien, A.; Miller, M.C. Evidence of a Strong 19.5 Hz Flux Oscillation in Swift BAT and Fermi GBM Gamma-Ray Data from GRB 211211A. *Astrophys. J.* **2024**, *967*, 26. [CrossRef]
375. Duncan, R.C. Global seismic oscillations in soft gamma repeaters. *Astrophys. J. Lett.* **1998**, *498*, L45. [CrossRef]
376. Fernández, R.; Metzger, B.D. Electromagnetic signatures of neutron star mergers in the advanced LIGO era. *Annu. Rev. Nucl. Part. Sci.* **2016**, *66*, 23–45. [CrossRef]
377. Zhang, B. The delay time of gravitational wave—gamma-ray burst associations. *Front. Phys.* **2019**, *14*, 64402. [CrossRef]
378. Ravi, V.; Lasky, P.D. The birth of black holes: Neutron star collapse times, gamma-ray bursts and fast radio bursts. *Mon. Not. R. Astron. Soc.* **2014**, *441*, 2433–2439. [CrossRef]

379. Ciolfi, R.; Kastaun, W.; Kalinani, J.V.; Giacomazzo, B. First 100 ms of a long-lived magnetized neutron star formed in a binary neutron star merger. *Phys. Rev. D* **2019**, *100*, 023005. [CrossRef]
380. Ciolfi, R. Collimated outflows from long-lived binary neutron star merger remnants. *Mon. Not. R. Astron. Soc.* **2020**, *495*, L66–L70. [CrossRef]
381. Kiuchi, K.; Reboul-Salze, A.; Shibata, M.; Sekiguchi, Y. A large-scale magnetic field produced by a solar-like dynamo in binary neutron star mergers. *Nat. Astron.* **2024**, *8*, 298–307. [CrossRef]
382. Paschalidis, V.; Etienne, Z.B.; Shapiro, S.L. Importance of cooling in triggering the collapse of hypermassive neutron stars. *Phys. Rev. D* **2012**, *86*, 064032. [CrossRef]
383. Mösta, P.; Radice, D.; Haas, R.; Schnetter, E.; Bernuzzi, S. A magnetar engine for short GRBs and kilonovae. *Astrophys. J.* **2020**, *901*, L37. [CrossRef]
384. Ruiz, M.; Shapiro, S.L.; Tsokaros, A. Jet launching from binary black hole-neutron star mergers: Dependence on black hole spin, binary mass ratio, and magnetic field orientation. *Phys. Rev. D* **2018**, *98*, 123017. [CrossRef]
385. Shibata, M.; Taniguchi, K. Merger of black hole and neutron star in general relativity: Tidal disruption, torus mass, and gravitational waves. *Phys. Rev. D* **2008**, *77*, 084015. [CrossRef]
386. Nampalliwar, S.; Suvorov, A.G.; Kokkotas, K.D. Testing horizon topology with electromagnetic observations. *Phys. Rev. D* **2020**, *102*, 104035. [CrossRef]
387. Spivey, R.J. Quasars: A supermassive rotating toroidal black hole interpretation. *Mon. Not. R. Astron. Soc.* **2000**, *316*, 856–874. [CrossRef]
388. Lu, M.-X.; Li, L.; Wang, X.-G.; Deng, C.-M.; Liang, Y.-F.; Lin, D.-B.; Liang, E.-W. Searching for Associations between Short Gamma-Ray Bursts and Fast Radio Bursts. *Astrophys. J.* **2024**, *961*, 45. [CrossRef]
389. Moroianu, A.; Wen, L.; James, C.W.; Ai, S.; Kovalam, M.; Panther, F.H.; Zhang, B. An assessment of the association between a fast radio burst and binary neutron star merger. *Nat. Astron.* **2023**, *7*, 579–589. [CrossRef]
390. McWilliams, S.T.; Levin, J. Electromagnetic extraction of energy from black-hole–neutron-star binaries. *Astrophys. J.* **2011**, *742*, 90. [CrossRef]
391. Most, E.R.; Philippov, A.A. Electromagnetic precursors to gravitational-wave events: Numerical simulations of flaring in pre-merger binary neutron star magnetospheres. *Astrophys. J.* **2020**, *893*, L6. [CrossRef]
392. Carrasco, F.; Shibata, M.; Reula, O. Magnetospheres of black hole-neutron star binaries. *Phys. Rev. D* **2021**, *104*, 063004. [CrossRef]
393. Most, E.R.; Philippov, A.A. Electromagnetic precursors to black hole–neutron star gravitational wave events: Flares and reconnection-powered fast radio transients from the late inspiral. *Astrophys. J.* **2023**, *956*, L33. [CrossRef]
394. Metzger, B.D.; Zivancev, C. Pair fireball precursors of neutron star mergers. *Mon. Not. R. Astron. Soc.* **2016**, *461*, 4435–4440. [CrossRef]
395. Daugherty, J.K.; Harding, A.K. Electromagnetic cascades in pulsars. *Astrophys. J.* **1982**, *252*, 337–347. [CrossRef]
396. Medin, Z.; Lai, D. Pair cascades in the magnetospheres of strongly magnetized neutron stars. *Mon. Not. R. Astron. Soc.* **2010**, *406*, 1379–1404. [CrossRef]
397. Mignani, R.P.; Testa, V.; Caniulef, D.G.; Taverna, R.; Turolla, R.; Zane, S.; Wu, K. Evidence for vacuum birefringence from the first optical polarimetry measurement of the isolated neutron star RX J1856. 5-3754. *Mon. Not. R. Astron. Soc.* **2017**, *465*, 492–500. [CrossRef]
398. Taverna, Roberto and Turolla, Roberto and Muleri, Fabio and Heyl, Jeremy and Zane, Silvia and Baldini, Luca and González-Caniulef, Denis and Bachetti, Matteo and Rankin, John and Caiazzo, Ilaria; et al. Polarized x-rays from a magnetar. *Science* **2022**, *378*, 646–650. [CrossRef]
399. Popov, S.B.; Taverna, R.; Turolla, R. Probing the surface magnetic field structure in RX J1856. 5-3754. *Mon. Not. R. Astron. Soc.* **2017**, *464*, 4390–4398. [CrossRef]
400. Hulsman, J. POLAR-2: A large scale gamma-ray polarimeter for GRBs. In *Space Telescopes and Instrumentation 2020: Ultraviolet to Gamma Ray, Society of Photo-Optical Instrumentation Engineers (SPIE) Conference Series*; den Herder, J.-W.A., Nikzad, S., Nakazawa, K., Eds.; SPIE Optical Engineering Press: Bellingham, WA, USA, 2020; Volume 11444, p. 114442V.
401. Most, E.R.; Kim, Y.; Chatziioannou, K.; Legred, I. Nonlinear Alfvén-wave Dynamics and Premerger Emission from Crustal Oscillations in Neutron Star Mergers. *arXiv* **2024**, arXiv:2407.17026. [CrossRef]
402. Neill, D.; Tsang, D.; van Eerten, H.; Ryan, G.; Newton, W.G. Resonant shattering flares in black hole-neutron star and binary neutron star mergers. *Mon. Not. R. Astron. Soc.* **2022**, *514*, 5385–5402. [CrossRef]
403. Neill, D.; Preston, R.; Newton, W.G.; Tsang, D. Constraining the Nuclear Symmetry Energy with Multimessenger Resonant Shattering Flares. *Phys. Rev. Lett.* **2023**, *130*, 112701. [CrossRef] [PubMed]
404. Reed, B.T.; Fattoyev, F.J.; Horowitz, C.J.; Piekarewicz, J. Implications of PREX-2 on the equation of state of neutron-rich matter. *Phys. Rev. Lett.* **2021**, *126*, 172503. [CrossRef] [PubMed]
405. Finn, L.S. G-modes in zero-temperature neutron stars. *Mon. Not. R. Astron. Soc.* **1987**, *227*, 265–293. [CrossRef]
406. McDermott, P.N. Density discontinuity g-modes. *Mon. Not. R. Astron. Soc.* **1990**, *245*, 508.
407. Sotani, H.; Tominaga, K.; Maeda, K.-I. Density discontinuity of a neutron star and gravitational waves. *Phys. Rev. D* **2001**, *65*, 024010. [CrossRef]
408. Dong, W.; Melatos, A. Gravitational waves from non-radial oscillations of stochastically accreting neutron stars. *Mon. Not. R. Astron. Soc.* **2024**, *530*, 2822–2839. [CrossRef]

409. McDermott, P.N.; van Horn, H.M.; Hansen, C.J. Nonradial oscillations of neutron stars. *Astrophys. J.* **1988**, *325*, 725–748. [CrossRef]
410. Kuan, H.-J.; Suvorov, A.G.; Doneva, D.D.; Yazadjiev, S.S. Gravitational waves from accretion-induced descalarization in massive scalar-tensor theory. *Phys. Rev. Lett.* **2022**, *129*, 121104. [CrossRef]
411. McDermott, P.N.; Hansen, C.J.; van Horn, H.M.; Buland, R. The nonradial oscillation spectra of neutron stars. *Astrophys. J.* **1985**, *297*, L37–L40. [CrossRef]
412. Strohmayer, T.E. Density discontinuities and the g-mode oscillation spectra of neutron stars. *Astrophys. J.* **1993**, *417*, 273. [CrossRef]
413. Chambers, F.R.N.; Watts, A.L. Relativistic ocean r-modes during type-I X-ray bursts. *Mon. Not. R. Astron. Soc.* **2020**, *491*, 6032–6044. [CrossRef]
414. Nättilä, J.; Cho, J.Y.K.; Skinner, J.W.; Most, E.R.; Ripperda, B. Neutron Star Atmosphere–Ocean Dynamics. *Astrophys. J.* **2024**, *971*, 37. [CrossRef]
415. van Baal, B.F.A.; Chambers, F.R.N.; Watts, A.L. Waves in thin oceans on oblate neutron stars. *Mon. Not. R. Astron. Soc.* **2020**, *496*, 2098–2106. [CrossRef]
416. Sullivan, A.G.; Alves, L.M.B.; Spence, G.O.; Leite, I.P.; Veske, D.; Bartos, I.; Márka, Z.; Márka, S. Multimessenger emission from tidal waves in neutron star oceans. *Mon. Not. R. Astron. Soc.* **2023**, *520*, 6173–6189. [CrossRef]
417. Thorne, K.S. Tidal stabilization of rigidly rotating, fully relativistic neutron stars. *Phys. Rev. D* **1998**, *58*, 124031. [CrossRef]
418. Andersson, N.; Kokkotas, K.D. Gravitational waves and pulsating stars: What can we learn from future observations? *Phys. Rev. Lett.* **1996**, *77*, 4134. [CrossRef]
419. Manoharan, P.; Kokkotas, K.D. Finding universal relations using statistical data analysis. *Phys. Rev. D* **2024**, *109*, 103033. [CrossRef]
420. Andersson, N. A new class of unstable modes of rotating relativistic stars. *Astrophys. J.* **1998**, *502*, 708. [CrossRef]
421. Friedman, J.L.; Morsink, S.M. Axial instability of rotating relativistic stars. *Astrophys. J.* **1998**, *502*, 714. [CrossRef]
422. Kokkotas, K.D.; Schwenzer, K. R-mode astronomy. *Eur. Phys. J. A* **2016**, *52*, 38. [CrossRef]
423. Andersson, N.; Kokkotas, K.; Schutz, B.F. Gravitational radiation limit on the spin of young neutron stars. *Astrophys. J.* **1999**, *510*, 846. [CrossRef]
424. Antonopoulou, D.; Espinoza, C.M.; Kuiper, L.; Andersson, N. Pulsar spin-down: The glitch-dominated rotation of PSR J0537-6910. *Mon. Not. R. Astron. Soc.* **2018**, *473*, 1644–1655. [CrossRef]
425. Andersson, N.; Antonopoulou, D.; Espinoza, C.M.; Haskell, B.; Ho, W.C.G. The enigmatic spin evolution of PSR J05370-6910: r-modes, gravitational waves, and the case for continued timing. *Astrophys. J.* **2018**, *864*, 137. [CrossRef]
426. Rezzolla, L.; Lamb, F.K.; Markovi´c, D.; Shapiro, S.L. Properties of *r* modes in rotating magnetic neutron stars. II. Evolution of the *r* modes and stellar magnetic field. *Phys. Rev. D* **2001**, *64*, 104014. [CrossRef]
427. Balbus, S.A.; Hawley, J.F. A powerful local shear instability in weakly magnetized disks. I-Linear analysis. II-Nonlinear evolution. *Astrophys. J.* **1991**, *376*, 214–233. [CrossRef]
428. Duez, M.D.; Liu, Y.T.; Shapiro, S.L.; Shibata, M.; Stephens, B.C. Evolution of magnetized, differentially rotating neutron stars:<? format?> Simulations in full general relativity. *Phys. Rev. D* **2006**, *73*, 104015.
429. Dehman, C.; Pons, J.A. On the Origin of Magnetar Fields: Chiral Magnetic Instability in Neutron Star Crusts. *arXiv* **2024**, arXiv:2408.05281.
430. Mészáros, P.; Rees, M.J. Steep slopes and preferred breaks in gamma-ray burst spectra: The role of photospheres and comptonization. *Astrophys. J.* **2000**, *530*, 292. [CrossRef]
431. Lyutikov, M. Electrodynamics of binary neutron star mergers. *Mon. Not. R. Astron. Soc.* **2019**, *483*, 2766–2777. [CrossRef]
432. Sridhar, N.; Zrake, J.; Metzger, B.D.; Sironi, L.; Giannios, D. Shock-powered radio precursors of neutron star mergers from accelerating relativistic binary winds. *Mon. Not. R. Astron. Soc.* **2021**, *501*, 3184–3202. [CrossRef]
433. Beskin, V.S. Radio pulsars: Already fifty years! *Phys. Uspekhi* **2018**, *61*, 353. [CrossRef]
434. Beloborodov, A.M. Emission of magnetar bursts and precursors of neutron star mergers. *Astrophys. J.* **2021**, *921*, 92. [CrossRef]
435. Mastrano, A.; Suvorov, A.G.; Melatos, A. Interpreting the AXP 1E 2259+ 586 antiglitch as a change in internal magnetization. *Mon. Not. R. Astron. Soc.* **2015**, *453*, 522–530. [CrossRef]
436. Coppin, P.; van Eijndhoven, N. IceCube search for high-energy neutrinos produced in the precursor stages of gamma-ray bursts. In Proceedings of the 36th International Cosmic Ray Conference (ICRC2019), Madison, WI, USA, 24 July–1 August 2019; Volume 36, p. 859.
437. Aartsen, M.G. et al. [IceCube Collaboration] Evidence for high-energy extraterrestrial neutrinos at the IceCube detector. *Science* **2013**, *342*, 1242856. [PubMed]
438. Aartsen, M.G. et al. [IceCube Collaboration] A combined maximum-likelihood analysis of the high-energy astrophysical neutrino flux measured with IceCube. *Astrophys. J.* **2015**, *809*, 98. [CrossRef]
439. Abbasi, R. et al. [IceCube Collaboration] IceCube high-energy starting event sample: Description and flux characterization with 7.5 years of data. *Phys. Rev. D* **2021**, *104*, 022002. [CrossRef]
440. Aartsen, M.G. et al. [IceCube-Gen2 Collaboration] IceCube-Gen2: The window to the extreme Universe. *J. Phys. G* **2021**, *48*, 060501. [CrossRef]
441. Murase, K.; Bartos, I.High-energy multimessenger transient astrophysics. *Annu. Rev. Nucl. Part. Sci.* **2019**, *69*, 477. [CrossRef]

442. Anchordoqui, L.A.; Barger, V.; Cholis, I.; Goldberg, H.; Hooper, D.; Kusenko, A.; Learned, J.G.; Marfatia, D.; Pakvasa, S.; Paul, T.C.; et al. Cosmic Neutrino Pevatrons: A Brand New Pathway to Astronomy, Astrophysics, and Particle Physics. *J. High Energy Astrophys.* **2014**, *1*, 1. [CrossRef]

443. Fujikawa, K.; Shrock, R. Magnetic moment of a massive neutrino and neutrino-spin rotation. *Phys. Rev. Lett.* **1980**, *45*, 963. [CrossRef]

444. Shrock, R.E. Electromagnetic properties and decays of Dirac and Majorana neutrinos in a general class of gauge theories. *Nucl. Phys. B* **1982**, *206*, 359–379. [CrossRef]

445. Giunti, C.; Studenikin, A. Neutrino electromagnetic interactions: A window to new physics. *Rev. Mod. Phys.* **2015**, *87*, 531–591. [CrossRef]

446. Vietri, M. On the acceleration of ultra high energy cosmic rays in gamma ray bursts. *Astrophys. J.* **1995**, *453*, 883–889. [CrossRef]

447. Waxman, E. Cosmological gamma-ray bursts and the highest energy cosmic rays. *Phys. Rev. Lett.* **1995**, *75*, 386. [CrossRef] [PubMed]

448. Brdar, V.; Cheng, T.; Kuan, H.-J.; Li, Y.-Y. Magnetar-powered neutrinos and magnetic moment signatures at IceCube. *J. Cosmol. Astropart. Phys.* **2024**, *2024*, 026. [CrossRef]

449. Guépin, C.; Kotera, K.; Oikonomou, F. High-energy neutrino transients and the future of multi-messenger astronomy. *Nat. Rev. Phys.* **2022**, *4*, 697–712. [CrossRef]

450. Branchesi, M.; Maggiore, M.; Alonso, D.; Badger, C.; Banerjee, B.; Beirnaert, F.; Belgacem, E.; Bhagwat, S.; Boileau, G.; Borhanian, S.; et al. Science with the Einstein Telescope: A comparison of different designs. *J. Cosmol. Astropart. Phys.* **2023**, *2023*, 068. [CrossRef]

451. Hild, S.; Abernathy, M.; Acernese, F.; Amaro-Seoane, P.; Andersson, N.; Arun, K.; Barone, F.; Barr, B.; Barsuglia, M.; Beker, M.; et al. Sensitivity studies for third-generation gravitational wave observatories. *Class. Quantum Gravity* **2011**, *28*, 094013. [CrossRef]

452. Maggiore, M.; Van Den Broeck, C.; Bartolo, N.; Belgacem, E.; Bertacca, D.; Bizouard, M.A.; Branchesi, M.; Clesse, S.; Foffa, S.; García-Bellido, J.; et al. Science case for the Einstein telescope. *J. Cosmol. Astropart. Phys.* **2020**, *2020*, 050. [CrossRef]

453. Punturo, M.; Abernathy, M.; Acernese, F.; Allen, B.; Andersson, N.; Arun, K.; Barone, F.; Barr, B.; Barsuglia, M.; Beker, M.; et al. The Einstein Telescope: A third-generation gravitational wave observatory. *Class. Quantum Gravity* **2010**, *27*, 194002. [CrossRef]

454. Abbott, B.P. et al. [LIGO Scientific Collaboration] Exploring the sensitivity of next generation gravitational wave detectors. *Class. Quantum Gravity* **2017**, *34*, 044001. [CrossRef]

455. Punturo, M.; Abernathy, M.; Acernese, F.; Allen, B.; Andersson, N.; Arun, K.; Barone, F.; Barr, B.; Barsuglia, M.; Beker, M.; et al. A horizon study for cosmic explorer: Science, observatories, and community. *arXiv* **2021**, arXiv:2109.09882.

456. Reitze, D.; Adhikari, R.X.; Ballmer, S.; Barish, B.; Barsotti, L.; Billingsley, G.L.; Brown, D.A.; Chen, Y.; Coyne, D.; Eisenstein, R.; et al. Cosmic explorer: the US contribution to gravitational-wave astronomy beyond LIGO. *Bull. Am. Astron. Soc.* **2019**, *51*, 035.

457. Evans, M.; Corsi, A.; Afle, C.; Ananyeva, A.; Arun, K.G.; Ballmer, S.; Bandopadhyay, A.; Barsotti, L.; Baryakhtar, M.; Berger, E.; et al. Cosmic Explorer: A submission to the NSF MPSAC ngGW subcommittee. *arXiv* **2023**, arXiv:2306.13745.

458. Amaro-Seoane, P.; Andrews, J.; Arca Sedda, M.; Askar, A.; Baghi, Q.; Balasov, R.; Bartos, I.; Bavera, S.S.; Bellovary, J.; Berry, C.P.L.; et al. Astrophysics with the laser interferometer space antenna. *Living Rev. Relativ.* **2023**, *26*, 2.

459. Destounis, K.; Suvorov, A.G.; Kokkotas, K.D. Testing spacetime symmetry through gravitational waves from extreme-mass-ratio inspirals. *Phys. Rev. D* **2020**, *102*, 064041. [CrossRef]

460. Destounis, K.; Suvorov, A.G.; Kokkotas, K.D. Gravitational wave glitches in chaotic extreme-mass-ratio inspirals. *Phys. Rev. Lett.* **2021**, *126*, 141102. [CrossRef]

461. Berti, E.; Cardoso, V.; Starinets, A.O. Quasinormal modes of black holes and black branes. *Class. Quantum Gravity* **2009**, *26*, 163001. [CrossRef]

462. Konoplya, R.A.; Zhidenko, A. Quasinormal modes of black holes: From astrophysics to string theory. *Rev. Mod. Phys.* **2011**, *83*, 793–836. [CrossRef]

463. Suvorov, A.G.; Völkel, S.H. Exact theory for the Rezzolla-Zhidenko metric and self-consistent calculation of quasinormal modes. *Phys. Rev. D* **2021**, *103*, 044027. [CrossRef]

464. Chirenti, C.; Dichiara, S.; Lien, A.; Miller, M.C.; Preece, R. Kilohertz quasiperiodic oscillations in short gamma-ray bursts. *Nature* **2023**, *613*, 253–256. [CrossRef]

465. Zink, B.; Lasky, P.D.; Kokkotas, K.D. Are gravitational waves from giant magnetar flares observable? *Phys. Rev. D* **2012**, *85*, 024030. [CrossRef]